SCHOOL OF ENGINEERING
RESEARCH
SHOWCASE 2017

2017 Research Showcase Posters
Table of Contents

Cross-Language Microblog Retrieval using Latent Semantic Modeling
by: Archana Godavarthy and Yi Fang ... page 1

Review Summarization through Question Retrieval and Diversification
by: Alexander G. Choulos and Yi Fang ... page 2

Using Absorbing Frequency Selective Surfaces to Suppress Radiated Electromagnetic Emissions
by: Ali Khoshniat and Ramesh Abhari ... page 3

Droplet Microfluidic Platforms for the Determination of Single-Cell Lactate Release and [18F] Fluorodeoxyglucose Uptake
by: Amy Mongersun, Debanti Sengupta, Ian Smeenk, Guillem Pratx, Prashanth Asuri, and Paul Abbyad ... page 4

Non-Isothermal Precipitation Hardening of AZ91 Magnesium Alloy
by: Anneliese Bals and Panthea Sepehrband ... page 5

A 60 GHz 2x2 Planar Microstrip Patch Antenna Phased Array with SIW Modified Butler Matrix Feed
by: Benjamin Horwath and Dr. Ramesh Abhari ... page 6

Reverse engineer blue fluorescent peptide by site-directed mutagenesis of iGFP
by: Casey Kiyohara and Jonathan Zhang ... page 7

Multilingual web search interface design: a user behavior analysis
by: Chenjun Ling, Ryan Lowe, Alexander Choulos, and Ben Steichen ... page 8

Influence of Slippery Pacemaker Leads on Lead-Induced Venous Occlusion
by: S. Bhatia, D. Obenauf, O. S. Pak, W. Yang, M. Esmaily-Moghadam, and J. Feinstein ... page 9

SCHOOL OF ENGINEERING RESEARCH SHOWCASE 2017

[Evaluating the effect of nanoparticle-protein interactions on the biological responses of nanoparticles]
by: Evangelia Bouzos, Erik Berggren, Lauren Schmitt, Sarah Anderson, Prashanth Asuri, and Korin Wheeler ... page 10

[Hydrodynamic Capture of Particles by Micro-swimmers under Hele-Shaw Flows]
by: Grant Mishler, Alan Cheng Hou Tsang, and On Shun Pak ... page 11

[Deep Network Optimization for Wearable Computing]
by: Haofeng Kou, Yi Fang, and Weijia Shang ... page 12

[Electro-deformation of a Vesicle]
by: H. Nganguia, O. S. Pak, Y.-N. Young, W.-F. Hu, and M.-C. Lai ... page 13

[Knowledge Base Research at SCU]
by: Hung Nguyen and Dr. Yi Fang ... page 14

[Exposing Privacy Risks on Social Media]
by: Isabela Figueira, Archana Godavarthy, and Prof. Yi Fang ... page 15

[Fuzzy Model-Based Control of Spacecraft with Fuel Sloshing Dynamics]
by: Lilit Mazmanyan and Dr. Mohammad A. Ayoubi ... page 16

[An Approach to Image Compression using R-D Optimal OMP selection]
by: Madhusudan Kalluri, Dr. Minqiang Jiang, and Dr. Nam Ling ... page 17

[FEA Analysis of Al-Cu Intermetallic Compounds Growth Mechanism During Thermosonic Ball Bonding Process in Micro-Electronic Packaging]
by: Maryam Gholamirad and Panthea Sepehrband ... page 18

[Breakabot Precomputed Model for Anomaly Management]
by: Matthew Condino, Dr. Christopher Kitts, and Mike Rasay ... page 19

[Hybrid Force/Position Control Architecture for Mobile Robot Formations]
by: Michael Neumann and Dr. Christopher Kitts ... page 20

[Molecular dynamics study of effect of crystallographic orientation on critical distance for Jump to Contact]
by: M. Khajehvand and P. Sepehrband ... page 21

SCHOOL OF ENGINEERING RESEARCH SHOWCASE 2017

[Engineering exosomes towards therapeutics](#)
by: Natalie Duong and Dr. Biao Lu ... page 22

[Compact Microstrip Yagi-Uda Antenna Arrays for Microwave Hyperthermia at 5.8 GHz](#)
by: Nivedita Parthasarathy and Dr. Ramesh Abhari ... page 23

[Signature Based Fast Motion Estimation for HD Video](#)
by: Pavel Arnaudov and Dr. Tokunbo Ogunfunmi ... page 24

[Towards Efficient Resource Provisioning in MapReduce](#)
by: Peter P. Nghiem and Silvia M. Figureira ... page 25

[Enhanced Intra Prediction Mode Coding by using Reference Samples in Video Compression](#)
by: Promila Agarwal, Michael Schimpf, Dr. Jiang, and Dr. Ling ... page 26

[Personalized Data Visualization Aids for Improving Visualization Understanding](#)
by: Renee Prescilla and Ben Steichen ... page 27

[Aggregated Search User Interface Research](#)
by: Dr. Ben Steichen and Robert Bayer ... page 28

[Applications of Adaptive Navigation of Multirobot Clusters](#)
by: Robert McDonald and Dr. Christopher Kitts ... page 29

[A Novel Algorithm for MPM Derivation](#)
by: Shanxi Li, Nam Ling, and Minqiang Jiang ... page 30

[Molecular Dynamics Study of Self-diffusion Along Dislocations in FCC Metals](#)
by: Siavash Soltani and Panthea Sepehrband ... page 31

[Causal Modeling for Data Security and Protection of Transparency](#)
by: Dr. Suchitra Abel and Adel Abdalla ... page 32

[Variational Deep Semantic Hashing for Text Documents](#)
by: Suthee Chaidaroon and Yi Fang ... page 33

[A Quantitative Survey Of Two Eigenvalue Bounds Of Matrix Polynomials](#)
by: Tim Shur and Aaron Melman ... page 34

SCHOOL OF ENGINEERING
RESEARCH SHOWCASE 2017

Neural Semantic Personalized Ranking for Item Cold-Start Recommendation
by: Travis Ebesu and Yi Fang ... page 35

Energy-Efficient Channel Assignment and Association Management in Centralized WLANs
by: Vahid Esmaeelzadeh and Behnam Dezfouli ... page 36

Recommendation System Based on Dynamic Matrix Factorization
by: Yaojian Wang and Yuhong Liu ... page 37

Process Design for CNT Growth on Graphene
by: Zachary Baron, Richard Senegor, Changjian Zhou, and Cary Y. Yang ... page 38

Cross-Language Microblog Retrieval using Latent Semantic Modeling

Archana Godavarthy, Yi Fang
Department of Computer Engineering
Santa Clara University
ngodavarthy@scu.edu, yfang@scu.edu

Santa Clara University

Motivation

Cross-Language retrieval is useful for multilingual users. Can also be used for tasks like Online-advertising & Recommending interesting articles

Challenges

- Tweets are short text with 140 character limitation.
- Due to poor spelling and grammar with irregular and noisy tokens, **Machine Translation** is not effective.

HashTags

Parallel Text

HashTag: #Immigration
English Tweet: Our overall #immigration policy is focus enfrcmnt resources more effectively on threats to pub safety & border security
Spanish Tweet: Por que importa una reforma migratoria integral en EU: "US #immigration: Help wanted" via FT
English Translation :Why not give a comprehensive immigration reform in the US , "US #immigration: Help wanted" via FT

Key Contributions

- **Latent Semantic Approach** learnt the latent features between different languages **without** the need for **Translation**.
- **Pair-wise Relevance** if effective in the absence of negative relevance judgement.
- Using **Hashtags** for Ground Truth collection was useful to Automating the process.

Future Work

- Apply non-linear mapping with deep learning
- Experiment with more languages.
- Comprehensive testing with stronger baselines.

Problem Statement

Given a query(English tweet), retrieve relevant tweets from a different language(Spanish tweets)

Latent Semantic Modeling

$\phi_e : R^n \to R^K, \phi_s : R^p \to R^K$. We apply linear mapping for both ϕ_e and ϕ_s as

$$\phi_e = \mathbf{e}_i^T \mathbf{W} \quad (1)$$
$$\phi_s = \mathbf{s}_j^T \mathbf{Q} \quad (2)$$

where $\mathbf{W}$ and $\mathbf{Q}$ are the projection matrices for English and Spanish tweets respectively.
The relevance score $r(\mathbf{e}_i, \mathbf{s}_j)$ between the English and Spanish tweets can be measured by the inner product in the shared space:

$$r(\mathbf{e}_i, \mathbf{s}_j) = \phi_e \phi_s^T = \mathbf{e}_i^T \mathbf{W} (\mathbf{s}_j^T \mathbf{Q})^T = \mathbf{e}_i^T \mathbf{W} \mathbf{Q}^T \mathbf{s}_j \quad (3)$$

Pairwise Relevance

$$h(\mathbf{e}_i, \mathbf{s}_j^+, \mathbf{s}_m^-) = r(\mathbf{e}_i, \mathbf{s}_j^+) - r(\mathbf{e}_i, \mathbf{s}_m^-) = \mathbf{e}_i^T \mathbf{W} \mathbf{Q}^T (\mathbf{s}_j^+ - \mathbf{s}_m^-) \quad (4)$$

Total Loss

$$L = \sum_{e_i} \sum_{s_j^+, s_m^-} -\log \sigma\Big(h(\mathbf{e}_i, \mathbf{s}_j^+, \mathbf{s}_m^-)\Big) \quad (5)$$

where $h(\mathbf{e}_i, \mathbf{s}_j^+, \mathbf{s}_m^-) = r(\mathbf{e}_i, \mathbf{s}_j^+) - r(\mathbf{e}_i, \mathbf{s}_m^-) = \mathbf{e}_i^T \mathbf{W} \mathbf{Q}^T (\mathbf{s}_j^+ - \mathbf{s}_m^-)$ and $\sigma(x)$ is the sigmoid function defined as: $\sigma(x) = \frac{1}{1+\exp(-x)}$.

We use Stochastic Gradient Descent(**SGD**) to optimize the objective function.

$$\frac{\partial L}{\partial \mathbf{W}} = \frac{\partial L}{\partial h} \frac{\partial h}{\partial \mathbf{W}} = \Big(\sigma\Big(h(\mathbf{e}_i, \mathbf{s}_j^+, \mathbf{s}_m^-)\Big) - 1\Big) \mathbf{e}_i (\mathbf{s}_j^+ - \mathbf{s}_m^-)^T \mathbf{Q}$$
$$\frac{\partial L}{\partial \mathbf{Q}} = \frac{\partial L}{\partial h} \frac{\partial h}{\partial \mathbf{Q}} = \Big(\sigma\Big(h(\mathbf{e}_i, \mathbf{s}_j^+, \mathbf{s}_m^-)\Big) - 1\Big) (\mathbf{s}_j^+ - \mathbf{s}_m^-) \mathbf{e}_i^T \mathbf{W}$$

Data Set

1 million English tweets and 400,000 Spanish tweets
Preprocess by removing Retweets, URLs, usernames, punctuations, and stopwords

	#Tweets	#Unique Tokens
English	167,203	35,305
Spanish	198,690	30,531

133,762 pair-wise triples (80%)-Training.
5,880 common Hashtags

Notation

$\mathbf{e}_i \in R^n$: TF-IDF vector of English tweet: **nx1**
$\mathbf{s}_j \in R^p$: TF-IDF vector of Spanish tweet: **px1**
$\mathbf{W}$: Projection Matrix of English tweets: **nxk**
$\mathbf{Q}$: Projection Matrix of Spanish tweets: **pxk**
$\phi_e : R^n \to R^K, \phi_s : R^p \to R^K$
ϕ_e, ϕ_s: reduced dimensionality to the joint space
linear mapping: $\phi_e = \mathbf{e}_i^T \mathbf{W}$; $\phi_s = \mathbf{s}_j^T \mathbf{Q}$
Sample $\mathbf{e}_i$, $\mathbf{s}_j^+$ and $\mathbf{s}_m^-$ to form pair-wise triples $(\mathbf{e}_i, \mathbf{s}_j^+, \mathbf{s}_m^-)$

Results

Table 1: Experimental results for different baselines.

Method	P@5	P@10	AP@10	NDCG@10
Jaccard	0.060	0.110	0.157	0.074
BM25	0.080	0.100	0.170	0.075
CLM	**0.493**	**0.463**	0.536	**0.485**
Hybrid	**0.493**	0.460	**0.572**	0.479

Graphs & Examples

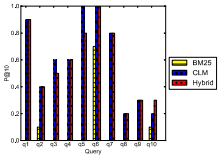

Query(q5): 2025 facebook?
CLM :(d1): snapchat redessociales (snapchat redessociales)
(d2):elimina botón redessociales feedly (delete button social networks feedly)
Query(q4): listeningto slang
CLM : tito bambino(a recording artist)

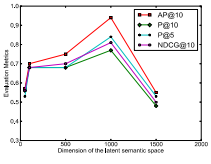

Figure 1: P@10 for 10 queries(left);Retrieval Examples(middle); Parameter Estimation (right)

Review Summarization through Question Retrieval and Diversification

Alexander G. Choulos • Yi Fang*
Department of Computer Science and Engineering
Santa Clara University
School of Engineering

Introduction

Product reviews have become an important resource for customers before they make purchase decisions. However, the abundance of reviews makes it difficult for customers to digest them. Our research aims to quickly capture the main idea of product reviews before users read the details. We have designed a two-stage approach which consists of question selection and diversification. Additionaly, we utilize a sequence-to-sequence learning model to measure the "answerability" of a review to questions. This approach has been found to be effective at finding representative questions.

- Existing Techniques for review analysis might be too general for real end-users
- Reading all reviews is time-consuming

Q: Does it have a fast autofocus?

autofocus. Its still worse than most cameras on the market, but its certainly better than the shot ruining autofocus of the first version. I like to use the DJI Ronin stabilizer and so autofocus is vital to me. I can't count how many times the a7s couldn't keep up with a subject simply walking forward. This camera does a much better job tracking subjects, although still far from perfect.

Methods

We want to maximize the relevancy, answerability, and diversification of questions. Thus, we have developed a 2-stage framework which first retrieves questions then diversifies them.

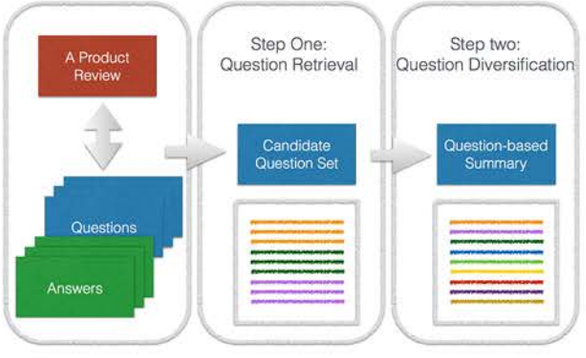

Question Retrieval

First, the query likelihood model with Jelinek-Mercer smoothing is employed. This essentially calculates the probability a question could have been generated from a review and answers.

$$\text{score}(r, q) = P(q|r)$$

Answerability

What is a review's potential for answering a question? We want to rank the question which is most answerable by the review. To do this, we utilized a sequence-to-sequence recurrent neural network.

Question Diversification

After a candidate question set is selected, next we make sure the questions have little semantic overlap. Finally, the scores for the relevancy, answerability, and diversity are combined. Optimizing for this, using a greedy algorithm, we are able to create the final question set.

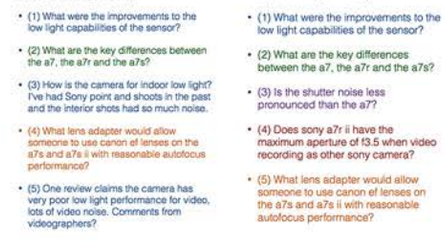

Results

Qualitative Results

Based on reivews for the Sony a7S II Camera:

Table 6: Human Annotation (Sony a7S II)

(1) How does this camera take videos in low light?
(2) Does this camera provide RAW image format?
(3) Does this camera record 4K internally?
(4) Does this camera have image stabilization?
(5) How would you describe the shutter noise?
(6) Does the EVF work well in bright conditions?
(7) Is there much of a difference in term of sensor?

Table 7: Questions Retrieved by Query Likelihood Model (Sony a7S II)

(1) What were the improvements to the low light capabilities of the sensor?
(2) What are the key differences between the a7, the a7r and the a7s?
(3) How is the camera for indoor low light? I've had Sony point and shoots in the past and the interior shots had so much noise.
(4) What lens adapter would allow someone to use canon ef lenses on the a7s and a7s ii with reasonable autofocus performance?
(5) One review claims the camera has very poor low light performance for video, lots of video noise. Comments from videographers?
(6) Do you need a special external recorder for 4k video like it is with a7s?
(7) Very curious to see how it does in low light. did sony really solve the noise problem??
(8) Where is it better? or is it?
(9) Does the a7II have a silent electronic shutter like the a7s?
(10) Is the shutter noise less pronounced than the a7?

Table 8: Questions Reranked by Submodular Function (Sony a7S II)

(1) What were the improvements to the low light capabilities of the sensor?
(2) What are the key differences between the a7, the a7r and the a7s?
(3) Is the shutter noise less pronounced than the a7?
(4) Does sony a7r ii have the maximum aperture of f3.5 when video recording as other sony camera?
(5) What lens adapter would allow someone to use canon ef lenses on the a7s and a7s ii with reasonable autofocus performance?
(6) How is the camera for indoor low light? I've had Sony point and shoots in the past and the interior shots had so much noise.
(7) Raw files, Would I see higher noise in the raw files?
(8) One review claims the camera has very poor low light performance for video, lots of video noise. Comments from videographers?
(9) Does the a7II have a silent electronic shutter like the a7s?
(10) Very curious to see how it does in low light. did sony really solve the noise problem??

Quantitative Results

Benchmarks were done using the ROGUE summary evaluation software package.

Table 9: Summarization Results (Unigram-ROUGE Scores) on TV Dataset

Length	Method	ROUGE1-R	ROUGE1-P	ROUGE1-F1
50	Q(Q)	0.248	0.177	0.192
	Q(Q, A)	0.267	0.190	0.205
	Q(Q) + answerable	0.258	0.190	0.204
	Q(Q) + MMR	0.259	0.181	0.195
	Q(Q, A) + MMR	0.263	0.189	0.204
	Q(Q) + sub	0.268	0.190	0.206
	Q(Q, A) + sub	**0.288**†	**0.209**†	**0.225**†
	Q(Q) + answerable + sub	0.263†	0.203†	0.220†
75	Q(Q)	0.324	0.137	0.199
	Q(Q, A)	0.334	0.161	0.203
	Q(Q) + answerable	0.329	0.164	0.206
	Q(Q) + MMR	0.326	0.158	0.200
	Q(Q, A) + MMR	0.336	0.163	0.205
	Q(Q) + sub	0.332	0.161	0.203
	Q(Q, A) + sub	0.353†	**0.175**†	**0.220**†
	Q(Q) + answerable + sub	**0.356**†	0.174†	0.219†
100	Q(Q)	0.372	0.137	0.190
	Q(Q, A)	0.380	0.140	0.194
	Q(Q) + answerable	0.387	0.145	0.199
	Q(Q) + MMR	0.376	0.139	0.192
	Q(Q, A) + MMR	0.386	0.142	0.196
	Q(Q) + sub	0.382	0.140	0.194
	Q(Q, A) + sub	0.401†	0.150†	0.207†
	Q(Q) + answerable + sub	**0.413**†	**0.153**†	**0.211**†

Table 11: Summarization Results (Unigram-ROUGE Scores) on Camera Dataset

Length	Method	ROUGE1-R	ROUGE1-P	ROUGE1-F1
50	Q(Q)	0.218	0.200	0.207
	Q(Q, A)	0.211	0.216	0.210
	Q(Q) + answerable	0.217	0.207	0.209
	Q(Q) + MMR	0.216	0.203	0.208
	Q(Q, A) + MMR	0.210	0.209	0.208
	Q(Q) + sub	0.213	0.231	0.216
	Q(Q, A) + sub	0.225	0.271†	0.236†
	Q(Q) + answerable + sub	**0.235**†	**0.286**†	**0.246**†
75	Q(Q)	0.306	0.221	0.245
	Q(Q, A)	0.277	0.228	0.240
	Q(Q) + answerable	0.291	0.240	0.253
	Q(Q) + MMR	0.288	0.234	0.248
	Q(Q, A) + MMR	0.277	0.229	0.241
	Q(Q) + sub	0.293	0.241	0.254
	Q(Q, A) + sub	0.297	0.242†	0.256†
	Q(Q) + answerable + sub	**0.309**†	**0.255**†	**0.268**†
100	Q(Q)	0.342	0.209	0.248
	Q(Q, A)	0.333	0.207	0.246
	Q(Q) + answerable	0.352	0.219	0.259
	Q(Q) + MMR	0.344	0.211	0.251
	Q(Q, A) + MMR	0.331	0.207	0.245
	Q(Q) + sub	0.350	0.216	0.257
	Q(Q, A) + sub	0.352	0.217†	0.258†
	Q(Q) + answerable + sub	**0.366**†	**0.229**†	**0.271**†

Future Work

Although used for the answerability characeristic, there is likely more potential for using sequence-to-sequence recurrent neural networks for review summarization. Additionally, utilizing more information from reviews, such as product specifications and question ratings. Finally, using the system on real world applications and incorpating user feedback would give us a better understanding of how good the summarization actually is.

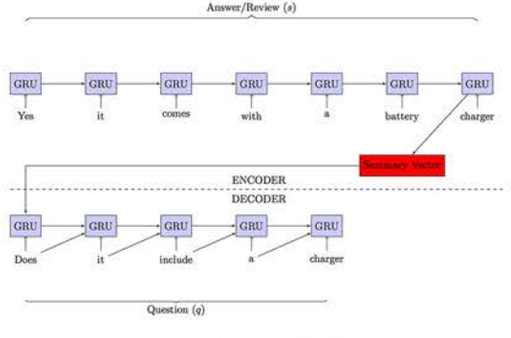

* Additional non-SCU affiliates were also collaborators on this research

Using Absorbing Frequency Selective Surfaces to Suppress Radiated Electromagnetic Emissions

Ali Khoshniat, and Ramesh Abhari
Department of Electrical Engineering, Santa Clara University
akhoshniat@scu.edu, rabhari@scu.edu

Santa Clara University
School of Engineering

Objective

- This research is intended to mitigate the radiated emission from an enclosure box at 8 GHz. The problem was observed in FCC testing of a data center's storage box containing PCIe Gen3 boards.

Introduction

- Solving electromagnetic compatibility (EMC) issues is challenging at higher frequencies.
- It is desired to reduce undesired EM emission with minimum or no change in the base system design by using gaskets and absorbers in the packaging, cover boxes and cases.
- Absorbing frequency selective surfaces (FSS) can be designed and used inside the box to suppress emission at a certain frequency.

Unit Cell Design

- The surface is seen by the incident plane wave as an equivalent series capacitor and inductor.
- The unit cell is implemented in a full-wave simulator and optimized to achieve surface impedance of Zin= 377 Ω (to match to free space intrinsic impedance) at this resonance frequency yielding w= 3.525 mm and g= 1.075 mm.
- Thin resistive film (Nickel Phosphorus alloy resistive material: 99,000 S/m) by Ohmega with thickness of 0.1 µm (sheet resistance of 100 Ω/square) is considered for implementing patches. Substrate material is Isola FR406 with thickness of d= 1.5748 mm, εr= 3.93, and tan δ= 0.0167.

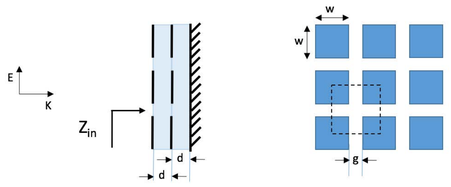

Side and top views of the two-layer FSS

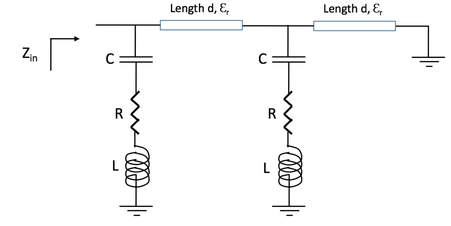

First order equivalent circuit

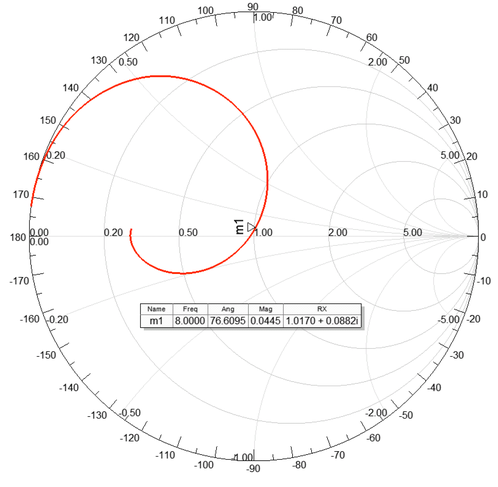

Normalized surface impedance of the unit cell

2-D Array RCS Simulation

- A uniform 2-D array of patches in RCS simulation shows FSS absorption at the frequency of interest.
- The total area is 41.1 mm by 41.4 mm. Baseline RCS simulation for same dimension conductor plane is assumed for complete reflection, i.e. 0dB. Therefore, the difference in RCS for FSS indicates absorbing characteristic of the designed array.

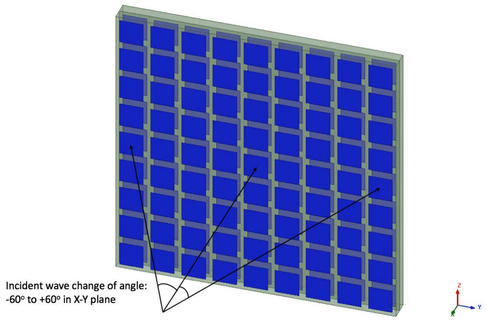

A 9x9 array of FSS for RCS simulation

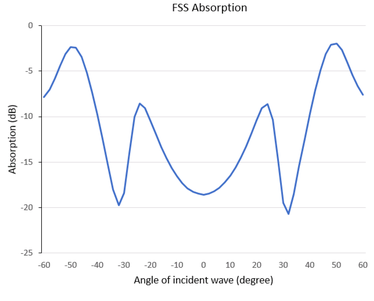

Reflection from 9x9 FSS for different incident angles

Absorbing FSS Inside a Box

- Box is excited with a printed dipole at 8 GHz to simulate EM leakage (as baseline) through openings for ventilation.
- FSS placed on top wall of the box (excited with a printed dipole at 8 GHz) shows reduction in EM emission.

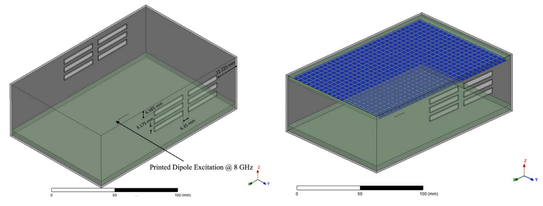

Box without and with FSS absorber excited by a small printed dipole antenna

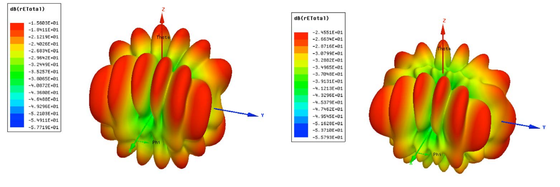

Total electric field radiated outside of the box without and with FSS absorber

Conclusions

The designed FSS shows maximum of 18 dB absorption in RCS simulation and in a practical test inside a box shows up to 9 dB reduction of EM emission leaked outside of the metal box.

Droplet Microfluidic Platforms for the Determination of Single-Cell Lactate Release and [18F] Fluorodeoxyglucose Uptake

Amy Mongersun †, Debanti Sengupta §, Ian Smeenk ‡, Guillem Pratx §, Prashanth Asuri †, Paul Abbyad ‡

†Department of Bioengineering, Santa Clara University, Santa Clara, California 95053, United States

‡Department of Chemistry and Biochemistry, Santa Clara University, Santa Clara, California 95053, United States

§Division of Radiation Physics, Department of Radiation Oncology, Stanford University School of Medicine, Stanford, California, United States

Background

Cancer cells utilize abnormal aerobic glycolysis and exhibit high levels of glucose uptake and lactate release via a phenomenon commonly referred to as the Warburg effect. Though the effects of altered metabolism in cancer have become increasingly important in cancer diagnosis and therapy, studies at the single cell level are lacking. We present here a multimodal droplet microfluidic method that allows the fast and quantitative determination of lactate release and radiolabeled glucose (FDG) uptake in many single cells. Measurements obtained from these techniques are used to assist in the identification of unusual subpopulations or rare malignant cancer cells.

Objectives

1. Develop high-throughput flow through device to measure glycolytic indexes on single cancer cells
2. Develop multimodal device to measure uptake of FDG and lactate release simultaneously
3. Determine the sources of cell-to-cell heterogeneity in cancer cell metabolism

Research Design

Single cancer cells exposed to FDG and a fluorescent probe for lactate are encapsulated in droplets formed at a flow focuser and anchored in place using passive forces. Droplets with encapsulated cells are positioned in an array above a scintillator plate. Lactate release rates and radioactive glucose uptake are observed.

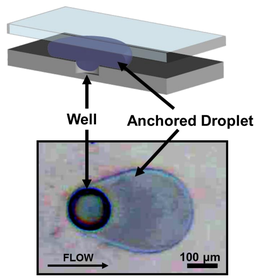

Figure 2. Rails and anchors technique. Variation in height of channel anchors droplets using a reduction in surface energy

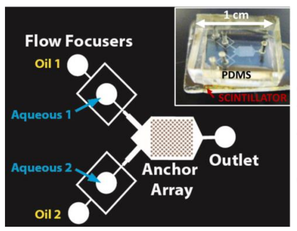

Figure 1. Microfluidic channel design with two flow focusers and an anchor array. Inset: picture of device.

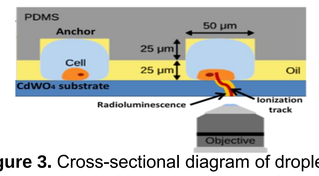

Figure 3. Cross-sectional diagram of droplet radiofluidics and β-ionization radioluminescence

Results

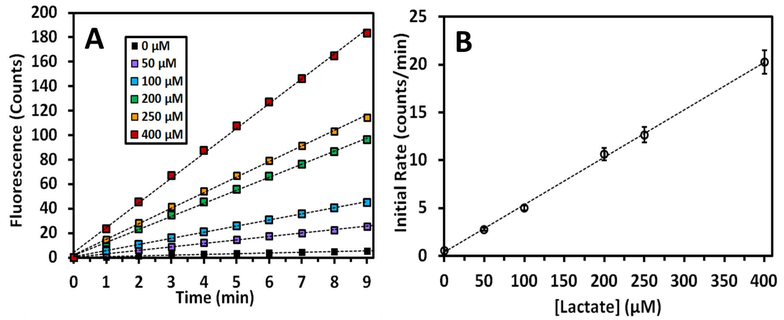

Figure 4. (A) Average fluorescence change in time for droplets of varying concentrations of lactate. (B) Lactate calibration curve demonstrating the initial rate of fluorescence increases at varying lactate concentrations. Error bars (95% confidence interval)

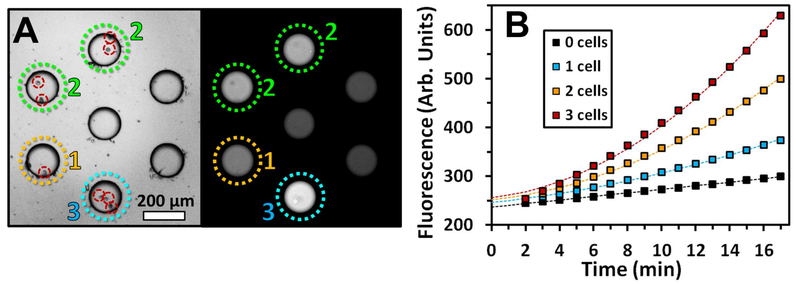

Figure 5. (A) Bright-field and fluorescent image of subsection of droplet array with individual glioblastoma cells in red. (B) Fluorescence for single droplets containing zero to three cells with dotted lines representing the fit from our mathematical lactate release model

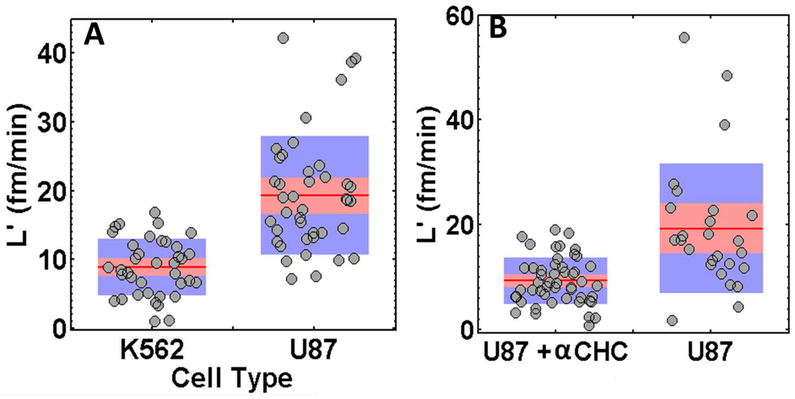

Figure 6. (A) Lactate release rates in femtomoles per minute of two different cancer cell lines. (B) Lactate release rates for single U87 cells treated with 3mM of αCHC and control cells (P > 0.001).

Results

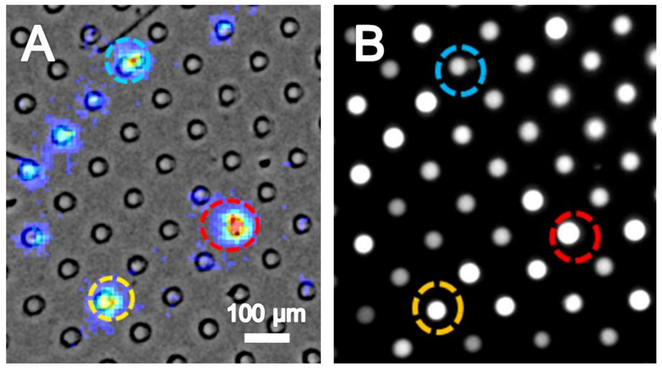

Figure 7. (A) Radioluminescence image of cells exposed to FDG. (B) Fluorescence intensity image of droplet encapsulated cells with colored circles identifying cells of interest.

Conclusions

- Quantitative measurements on single cellular lactate release rates can be obtained via fluorescent measurements
- Simultaneous measurements on lactate release and FDG concentration can be obtained on the same single cell
- There are high levels of cell-to-cell metabolic heterogeneity

Future Work

- Create flow through fluorescence device
- Develop cell sorting method utilizing dielectrophoresis
- Investigate the sources of cell-to-cell heterogeneity

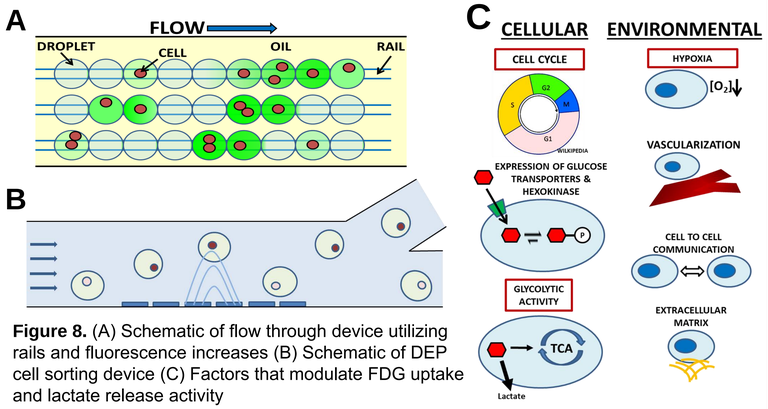

Figure 8. (A) Schematic of flow through device utilizing rails and fluorescence increases (B) Schematic of DEP cell sorting device (C) Factors that modulate FDG uptake and lactate release activity

Amy Mongersun
amongersun@scu.edu

References

1. Warburg O. On the Origin of Cancer Cells. Science. 1956;123(3191):309–314. PMID: 13298683
2. Phelps ME. PET : The Merging of Biology and Imaging into Molecular Imaging. J Nucl Med. 1999;41(4):661–681.
3. Mongersun A, Smeenk I, Pratx G, Asuri P, Abbyad P. Droplet Microfluidic Platform for the Determination of Single-Cell Lactate Release. Anal Chem. 2016;88(6):3257–3263.
4. Türkcan S, Nguyen J, Vilalta M, Shen B, Chin FT, Pratx G, Abbyad P. Single-Cell Analysis of [18F]Fluorodeoxyglucose Uptake by Droplet Radiofluidics. Anal Chem. 2015;6667–73. PMID: 26035453
5. Pratx G, Chen K, Sun C, Martin L, Carpenter CM, Olcott PD, Xing L. Radioluminescence microscopy: measuring the heterogeneous uptake of radiotracers in single living cells. PLoS One. 2012 Jan;7(10):e46285. PMID: 23056276
6. Abbyad P, Dangla R, Alexandrou A, Baroud CN. Rails and anchors: guiding and trapping droplet microreactors in two dimensions. Lab Chip. 2011;11:813–821.

Non-Isothermal Precipitation Hardening of AZ91 Magnesium Alloy

Anneliese Bals, Panthea Sepehrband
Department of Mechanical Engineering, Santa Clara University

Santa Clara University
School of Engineering

Background

The high strength-to-weight ratio of magnesium alloys make them an attractive candidate for increasing fuel efficiency.

Density of Metals

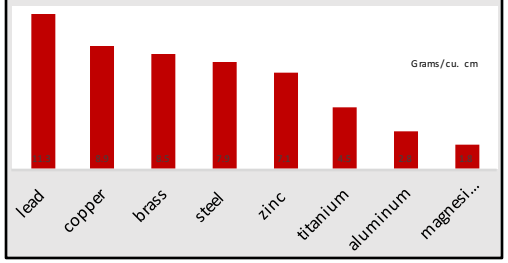

Problem Statement

Application of Magnesium for structural applications is still limited due to its relatively poor mechanical properties.

Property	Unit	AZ91	AM60	AM50	AM20	AS41	AS21	AE42
Ultimate Tensile Strength	MPa	240 (250)	225 (240)	210 (230)	190 (210)	215 (240)	175 (220)	230 (230)
Tensile Yield Strength (0.2% offset)	MPa	160 (160)	130 (130)	125 (125)	90 (90)	140 (140)	110 (120)	145 (145)
Compressive Yield Strength	MPa	160	130	125	90	140	110	145
Fracture Elongation	%	3 (7)	8 (13)	10 (15)	12 (20)	6 (15)	9 (13)	10 (11)
Elastic Modulus, tension	GPa	45	45	45	45	45	45	45
Elastic Modulus, shear	GPa	17	17	17	17	17	17	17
Brinell Hardness		70	65	60	45	60	55	60
Impact Strength Charpy un-notched test bars	J	6 (9)	17 (18)	18 (18)	18 (18)	4 (16)	5 (12)	5 (12)

Objective

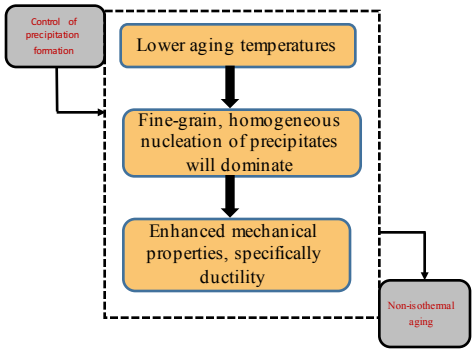

Research Design

Heat Treatment

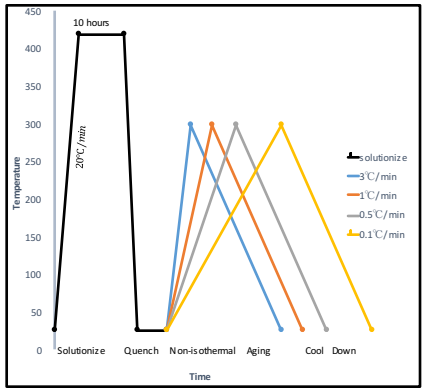

Natural Aging

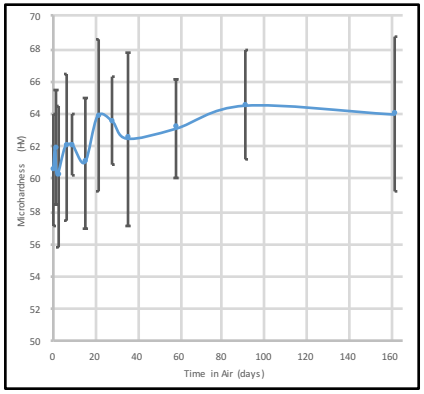

Results

Microhardness Testing

Isothermal Aging at 200°C

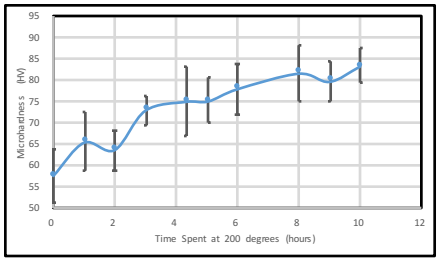

Non-Isothermal Aging

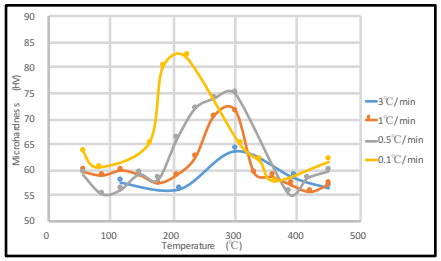

Although similar in value, it takes 33.3 hours for AZ91 to reach 221°C at 0.1°C/min, while it took AZ91 only 10 hours to reach its peak during isothermal aging at 200°C.

Kissinger Method for Activation Energy

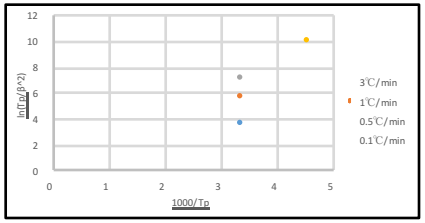

The activation energy of diffusion can be calculated using Kissinger's method which entails finding the slope of $\ln\frac{T_p}{\beta^2}$ vs. $\frac{1000}{T_p}$, where T_p is the temperature when peak hardness occurs and β is the heating rate. However, the peak hardness for each heating rate tested in this experiment was found to be at 300°C due to an insufficient number of samples taken at varying temperatures and a slope could not be found.

Future Research

Continued Isothermal Aging at 200°C

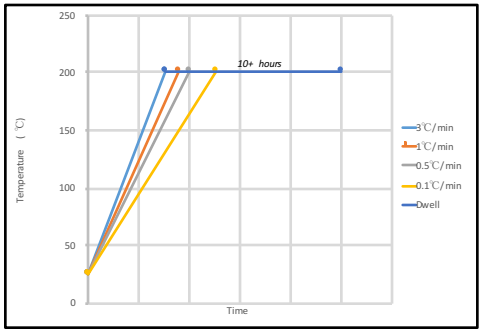

Dual Heat Treatment

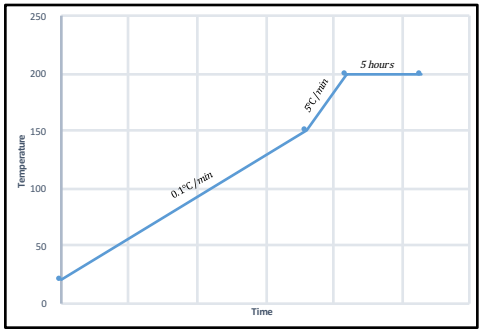

Acknowledgements

This research is funded through the 2015-2016 Kuehler Grant Undergraduate Research Support and The School of Engineering Internal Grant.

A 60 GHz 2x2 Planar Microstrip Patch Antenna Phased Array with SIW Modified Butler Matrix Feed

Benjamin Horwath, PhD Student; Dr. Ramesh Abhari, Advisor
Department of Electrical Engineering

Santa Clara University
School of Engineering

Motivation:

Interested in small footprint, low power designs for high bandwidth applications on handhelds or other low-profile, battery-operated devices

Objectives:

1. Modify the Butler Matrix to get outputs for a planar array
2. Use substrate integrated waveguide (SIW) apertures as phase shifters to shrink footprint of new Butler Matrix
3. Design, prototype, and measure the full, beam-switching antenna system

Planar Array for Beam Agility

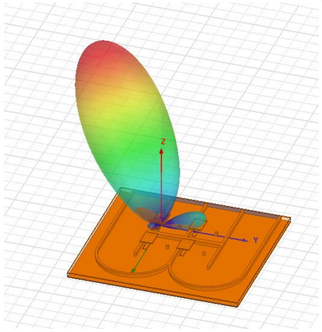

Modifying the Butler Matrix

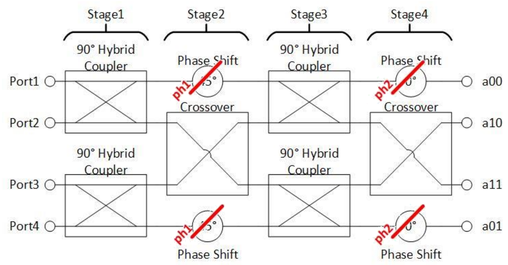

Generating Beam Patterns in θ and ϕ

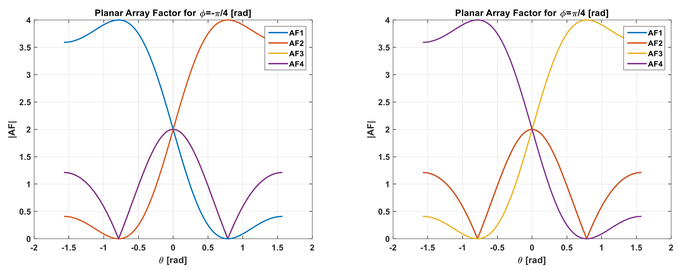

SIW Interconnect

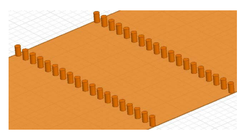

- Via diameter = 6mil
- Via pitch = 12mil
- Wall spacing = 2.5mm

Design:

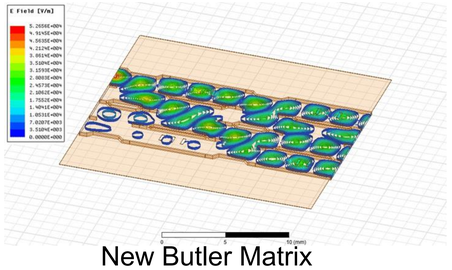

New Butler Matrix

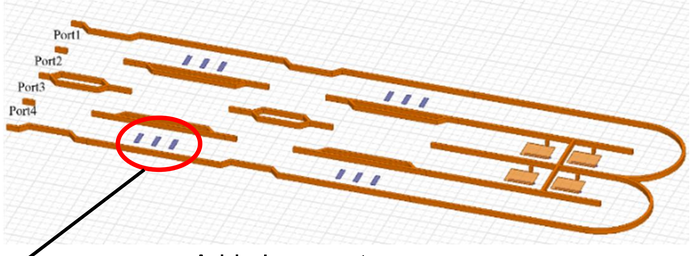

Add planar antenna array

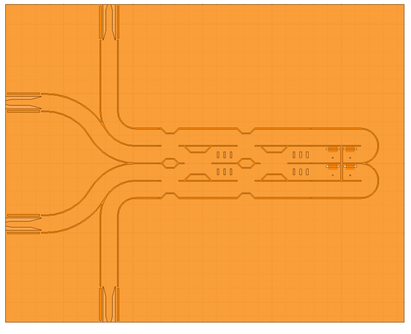

Full Prototype Layout

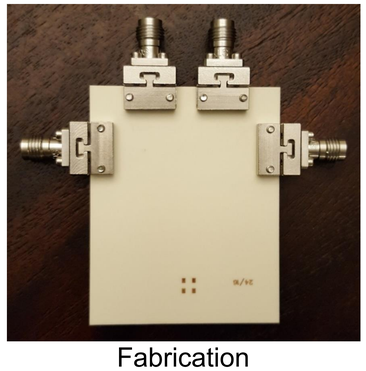

Fabrication

Breakout Design: Phase Shifters

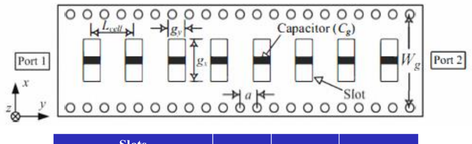

Slots [Lslot, Wslot, Space]	Δ phase	S11	S21
1 [0.26mm, 1.02mm, N/A]	-10.45°	-11.59 dB	-0.4224 dB
2 [0.23mm,0.88mm, 0.3mm]	-10.05°	-18.92 dB	-0.1221 dB
3 [0.15mm, 0.8mm, 0.3mm]	-10.13°	-38.73 dB	-0.0968 dB

Measurement Results - VNA

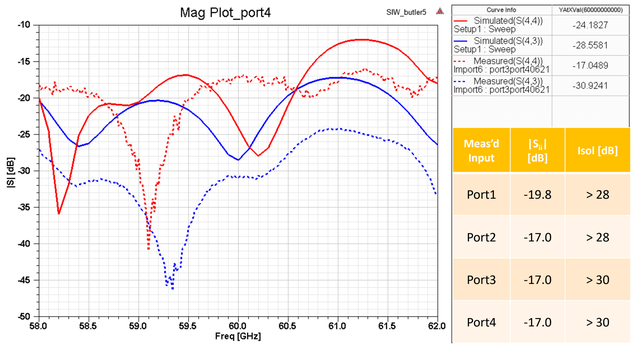

Curve Info	Y@(Val(8000000000))
Simulated(S(4,4)) Setup1 : Sweep	-24.1827
Simulated(S(4,3)) Setup1 : Sweep	-28.5581
Measured(S(4,4)) Import6 : port3port40621	-17.0489
Measured(S(4,3)) Import6 : port3port40621	-30.9241

Meas'd Input	$\|S_{ij}\|$ [dB]	Isol [dB]
Port1	-19.8	> 28
Port2	-17.0	> 28
Port3	-17.0	> 30
Port4	-17.0	> 30

Key findings of this project:

- The Butler Matrix can be readily modified for a 2x2 planar array
- Achieved significant circuit area savings over previous implementations
- Confirmed minimal crosstalk between tightly packed SIW channels in prototype designs

Next steps: 3D antenna pattern measurement

Reverse engineer blue fluorescent peptide by site-directed mutagenesis of iGFP

Casey Kiyohara, Jonathan Zhang, Ph.D.*
Department of Bioengineering

Santa Clara University
School of Engineering

INTRODUCTION

Green fluorescent protein (GFP) is a commonly used protein reporter with a wide range of applications as a fusion tag for proteins of interest.[1] However, its relatively large size (26.9 kDa) can prevent a protein of interest tagged with GFP from passing across cell membranes or interfere with the function of the protein of interest, particularly if it is similar in size to GFP.[1] A small (~10.5 kDa) green fluorescent peptide (iGFP) was developed by Dr. Jonathan Zhang from the chromophore sequence of full-length GFP. Using the GFP derivative BFP as a model, we are developing a small blue fluorescent peptide (iBFP) by site-directed mutagenesis of iGFP at a site that was rationally chosen. This peptide, produced in *E. coli*, would share iGFP's diminished effects on the protein of interest due to size while maintaining its fluorescent properties. Therefore, its potential applications are similar to those of full-length GFP and iGFP as a genetically encoded molecular probe with unique fluorescence.[1]

DESIGN

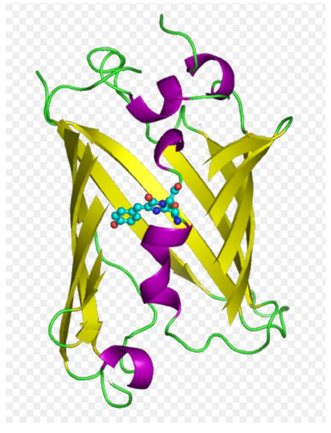

Figure 1. Structure of Green Fluorescent Protein (GFP).[4] Connected central spheres represent internal active site chromophore

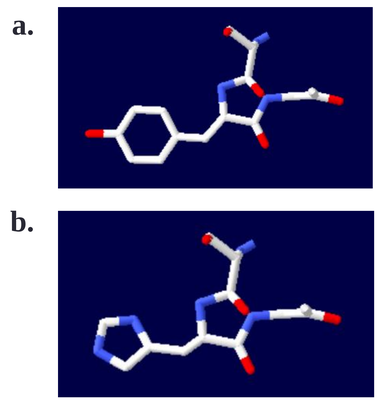

Figure 2. Key chromophore amino acid residues for GFP/iGFP (a) and BFP/iBFP (b).

- GFP and iGFP chromophores are 5-membered imidazolidinone rings formed by amino acid residues Ser65-Tyr66-Gly67 within protein's cylindrical structure[2] (Figure 1)
- Single point Y66H mutation of GFP has been shown to alter the excitation and emission behavior of this chromophore to create BFP[3] (Figure 2)
- Apply Y88H mutation to iGFP through site-directed mutagenesis to create peptide with similarly-shifted fluorescence to BFP (iBFP)

RESULTS

DNA

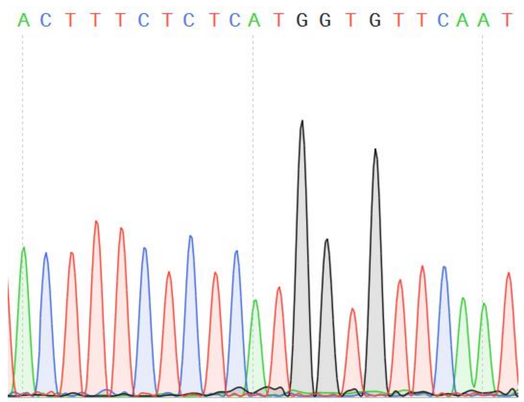

Figure 3. Chromatogram of iBFP DNA sequencing at site of Y66H mutation. Sequencing performed by Sequetech.

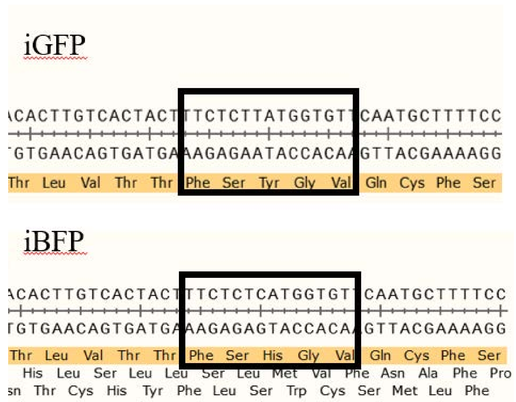

Figure 4. Comparison of iGFP sequence to iBFP sequence at site of Y66H mutation. Box surrounds key chromophore amino acid residues for iGFP and iBFP.

PROTEIN

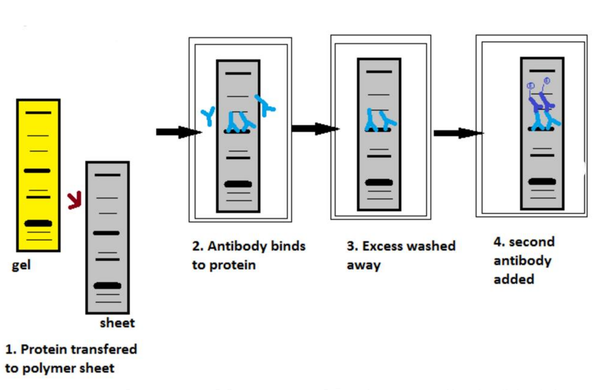

Figure 5. General Western blot protocol.[5] Primary antibody (blue) is specific to protein of interest. Second antibody (purple) is specific to primary antibody and contains substrate for subsequent visualization reaction.

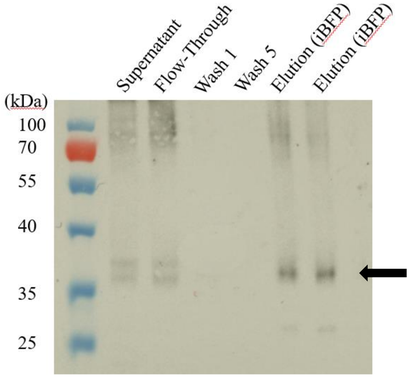

Figure 6. Western blot for iBFP purification. Each well in initial gel contained one sample from a step (as labeled) in purification of iBFP. Arrow indicates iBFP (predicted size 37-39 kDa.)

CONCLUSIONS

- DNA sequencing results suggest successful Y66H single point mutation of iGFP with no additional mutations (Figures 3, 4)
- Western blot results show protein band at predicted size of iBFP, suggesting successful expression and purification of peptide from *E. coli* (Figure 6)

Future Work:

- Perform assay to characterize fluorescent properties of iBFP
- Transfect plasmid into Hela cells to analyze properties in mammalian cell culture
- Apply methodology of reverse engineering to therapeutic proteins

REFERENCES

[1] Jensen, Ellen C. "Use of fluorescent probes: their effect on cell biology and limitations." *The Anatomical Record* 295.12 (2012): 2031-2036.
[2] Goodsell, D.S. "Green Fluorescent Protein (GFP)." *RCSB Protein Data Bank RCSB PDB* (2003): n. pag. Web.
[3] Day, Richard N., and Michael W. Davidson. "The fluorescent protein palette: tools for cellular imaging." *Chemical Society Reviews* 38.10 (2009): 2887-2921.
[4] Keller, Raymond. "GFP and Fluorophore." N.p., 28 Sept. 2008. Web.
[5] Cawang. Basic Western Blotting Steps. Digital image. N.p., 28 Oct. 2011. Web.

ACKNOWLEDGEMENTS

We would like to thank the 2016 Kuehler Undergraduate Research Program for their support of this project.

Multilingual web search interface design: a user behavior analysis

Chenjun Ling, Ryan Lowe, Alexander Choulos
Advisor: Ben Steichen
Human Centered Computing Lab, Computer Science and Engineering, Department of Computer Engineering
Santa Clara University
School of Engineering

Introduction

For multilingual search research, there has been a distinct lack of human-centered research to better understand and support multilingual user behaviors, needs, preferences and contexts. This paper proposes the first user behavior analyses of multilingual search users through detailed laboratory studies using state-of-the-art usability equipment which is eye tracking, facial expression, and wristband. Results from the studies will enable and drive the design and development of novel data-driven and personalized multilingual search systems that adapt the retrieval, composition, and presentation of multilingual information to each individual user's language abilities, preferences, and search context.

User Study Design

- **Multilingual Interfaces:** 4 types
  - **Interleaved** refers to the approach of interleaving multilingual results in a single ranked list
  - **Universal** Search refers to the approach of displaying contiguous blocks of results in different languages
  - **Tabbed** refers to interfaces that present results from each language using separate tabs
  - **Panels** refers to interfaces that present results in separate panels for each language

Interleaved

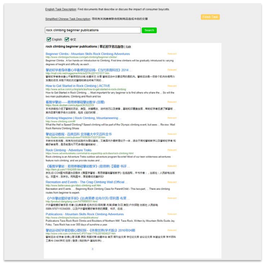

Universal

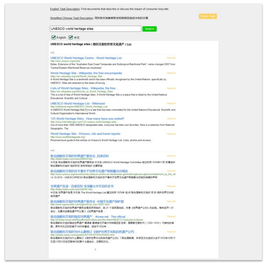

Tabbed

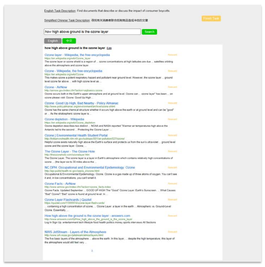

Panels

Experiment

- **Participants:** 36 (25 valid) : Num of languages, Language proficiency score (writing, reading, listening)
- **Procedure:** 3 steps; 90 minus; Control order（Interface, Task）
  - **Survey**: language proficiency
  - **Usability test**: 4 interfaces, each interface has 4 tasks (1 practice task + 3 real tasks)+ 1 Questionnaire (interface)
  - **Cognitive style test**: field dependency score

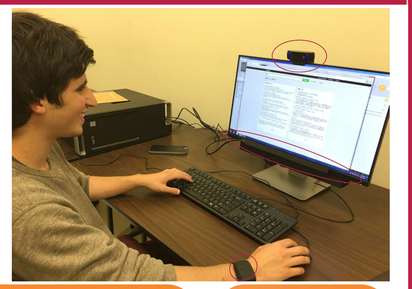

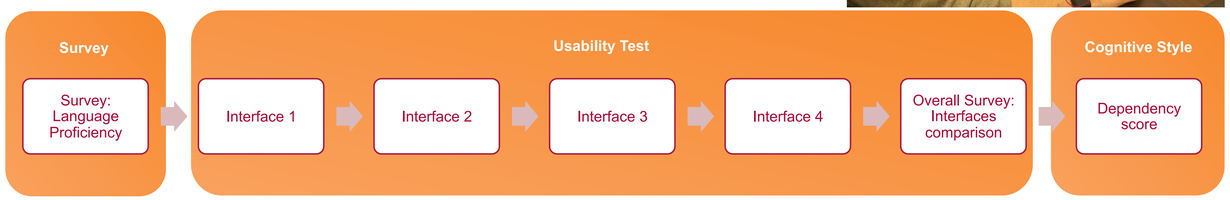

Method and Initial Analysis

- **Analysis Method**: ANOVA, T-test, and Chi-squared test.
- **Features/Measure**

Type	Features
Task	Time, Type
Queries	Number, Language
Docs	Num of viewed, Num of viewed per language, Num of relevant, Num of relevant per language
Language Proficiency	Proficiency score (Writing, Reading, Listing), High, Median, Low
Cognitive Style	Field dependency score
Interface	Preferences, Dislikes, Questionnaires
Eye Gaze	Fixations (number, rate, duration), Saccade Length
AOI	Fixations (number, rate, duration, proportion of total number, proportion of total duration, proportion of transition across AOIs), Saccade Length

- **AOI (Area of Interests): 6**

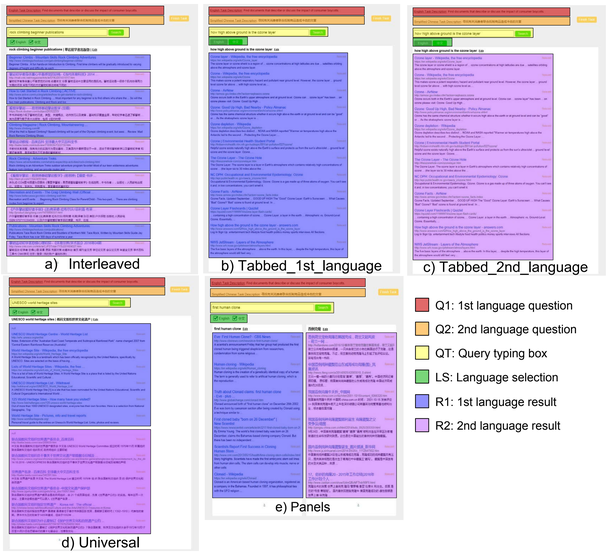

- **Initial Analysis: Eye gaze fixation heat map**

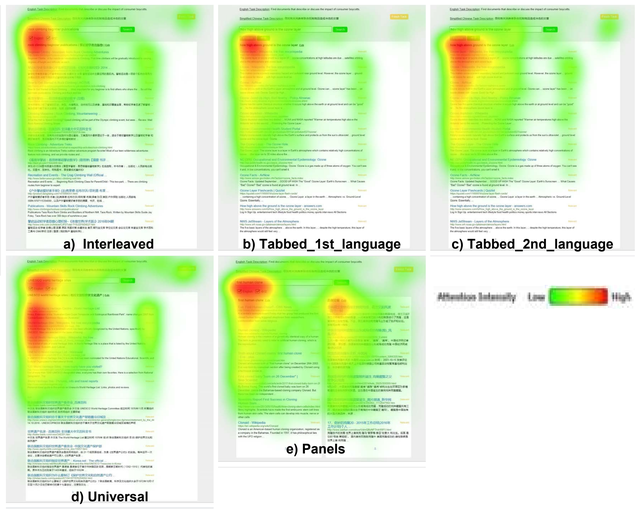

User Study Design

- **Task Questions and Types**
  - **3 types**: Doing, FactFinding, Learning
  - **13 task questions**: 1 practice task + 12 study task
- **Data Source Equipment**
  - **Traditional**: Monitor, Keyboard, Mouse
  - **Physiological** : Camera, Eye Tracker (Tobii), Wristband

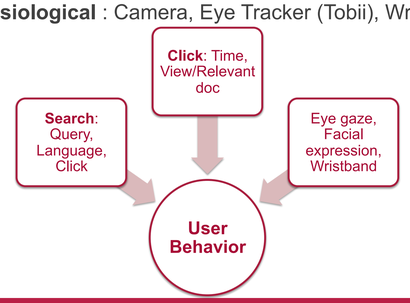

Additional Crowdsourcing Study

Task 1

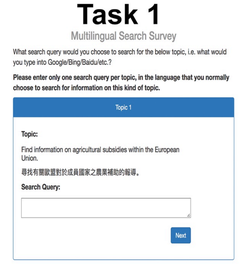

Task 2

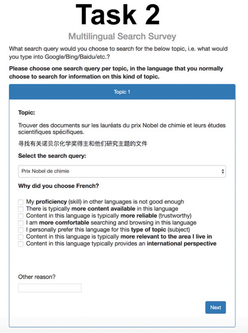

Task 3

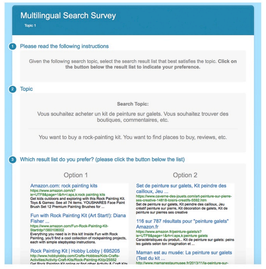

Results

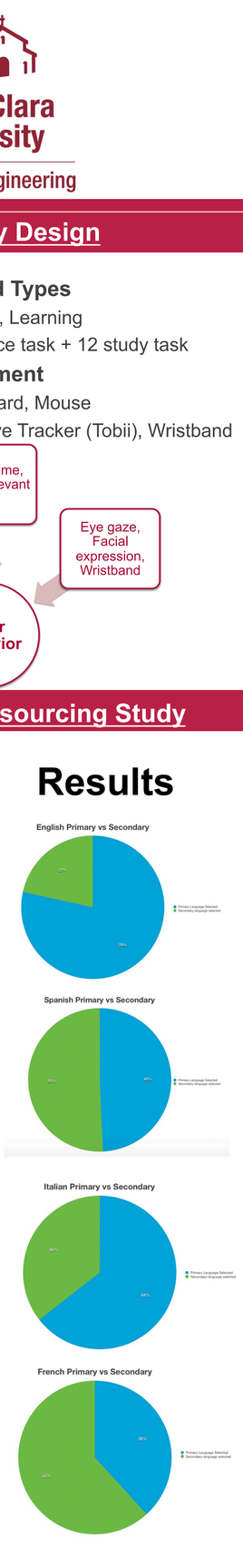

Influence of Slippery Pacemaker Leads on Lead-Induced Venous Occlusion

S. Bhatia, D. Obenauf, O. S. Pak
Department of Mechanical Engineering
Santa Clara University

W. Yang, M. Esmaily-Moghadam, J. Feinstein
Department of Pediatric Cardiology and Mechanical Engineering
Stanford University

Introduction

- Pacemakers are used to treat arrhythmias.
- Pacemaker implantation:
  between 1993-2009, 2.9 M patients in US
- Venous occlusion:
  15-30% for adults and 20% for children

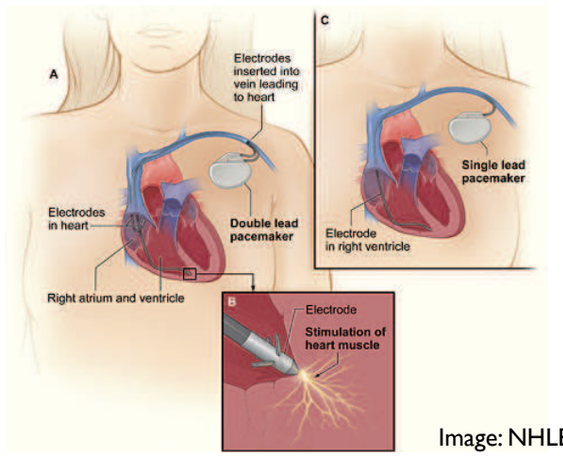

Image: NHLB, NIH

- Does lead size matter? Maybe.
- Small-diameter lead: increased rate of lead failure
- Simulations show flow stasis is concentrated around leads.
- What if slippery?
  - Pitcher plant inspired omniphobic surface coating (SLIPS)

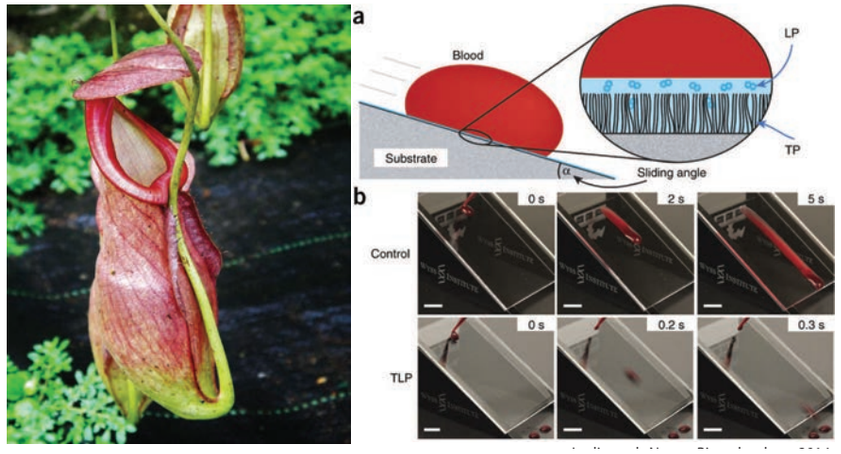

Leslie et al. (2014).Nature Biotechnol.

Computational Approach

- Navier-Stokes equations:

$$\rho\left(\frac{\partial \mathbf{u}}{\partial t}+\mathbf{u}\cdot\nabla\mathbf{u}\right)=\nabla\cdot\boldsymbol{\sigma}$$
$$\nabla\cdot\mathbf{u}=0$$

where $\sigma=-p\mathbf{I}+\mu(\nabla\mathbf{u}+\nabla(\mathbf{u})^T)$.

- Slip boundary conditions:

$$\mathbf{u}_{\parallel}=\lambda\mathbf{n}\cdot\boldsymbol{\sigma}\cdot(\mathbf{I}-\mathbf{nn})/\mu$$

- Implemented in Simvascular package
- Residence time:

$$\frac{\partial\tau}{\partial t}+\mathbf{u}\cdot\nabla\tau-\nabla\cdot\kappa\nabla\tau=H$$

Validation

- Simulation setting:
  $Q=16cc/s,\ R_o=0.55cm,\ R_i=0.117cm$

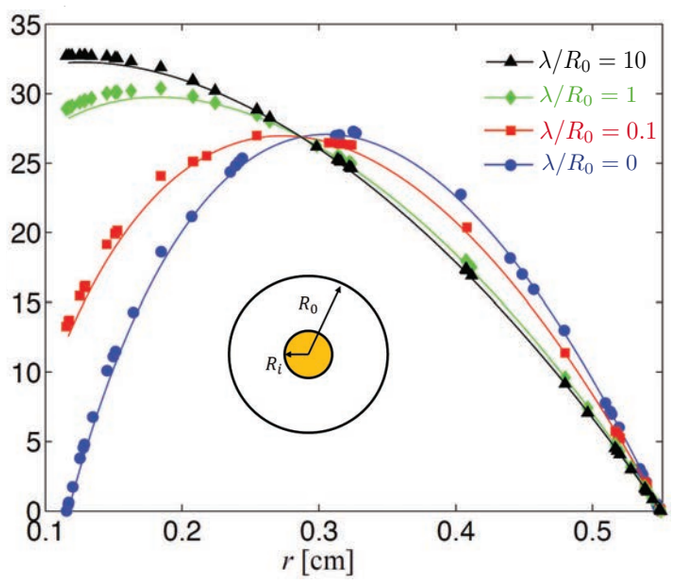

Eccentric Cylinders

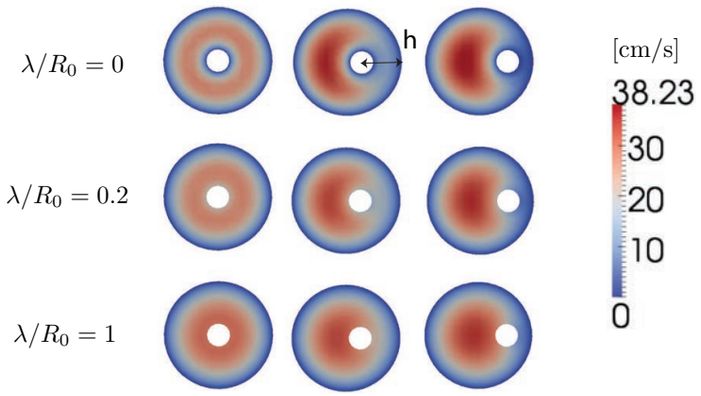

$h = 0.55, 0.41$ and 0.26 cm.

Patient-specific Simulation

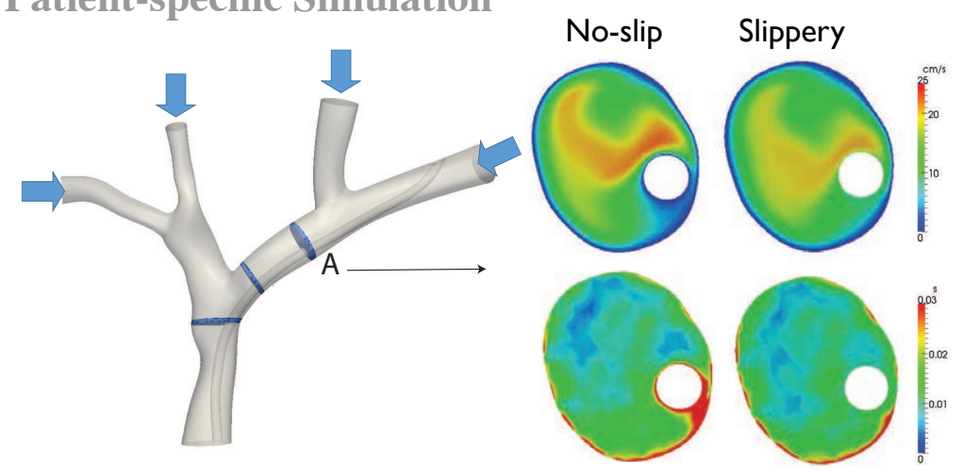

- The influence of a slippery hydrodynamic condition on pacemaker lead surface is evaluated in idealized and patient-specific scenarios.
- The slippery surface condition reduces the residence time in close proximity of the lead, suggesting its possibility of mitigating risks of lead-induced thrombosis.

References:

1. National Heart, Lung, and Blood Institute, NIH
2 Leslie et al. (2014).*Nature Biotechnol.* 32,1134-1140.

SANTA CLARA UNIVERSITY

Evaluating the effect of nanoparticle-protein interactions on the biological responses of nanoparticles

Evangelia Bouzos[1], Erik Berggren[2], Lauren Schmitt[2], Sarah Anderson[2], Prashanth Asuri[1], PhD, and Korin Wheeler[2], PhD

Departments of Bioengineering[1] and Chemistry and Biochemistry[2]

Introduction

A. Motivating Questions

- How do blood proteins influence the fate and toxicity of nanoparticles (NPs) that are commonly used for medicinal purposes?
- How does nanoparticle identity and surface coating influence the structure and function of human blood proteins?
- What role do proteins play in nanoparticle behavior, including aggregation and dissolution?
- What is the role of the engineered nanomaterial (ENM) protein corona in biological systems?

B. Defining the System

- A matrix of blood proteins and noble metal NPs were evaluated and analyzed.
- Blood proteins were selected for abundance and diversity of biophysical properties, including transferrin, fibrinogen, bovine serum albumin (BSA) and apolipoprotein A1 (**Table 1**).
- The library of 10 nm silver nanoparticles (Ag NPs) included a range of commonly employed surface coatings (**Table 2**).

Table 1. Physical properties of common human blood proteins.

Protein	Concentration in Blood	Size (kDa)	Estimated Protein Binding Sites on a 10 nm NP	
			Maximum	Minimum
Apolipoprotein A-1	1-3%	45.4	5.28	3.18
Bovine Serum Albumin	55%	66.5	32.90	2.93
Transferrin	4%	80	19.46	2.62
Fibrinogen	7%	340	29.84	1.19

Table 2. Chemical structures of common engineered surface coatings were employed on 10 nm noble metal NPs.

Surface	Structure	Zeta potential at pH 7	Description
Citrate	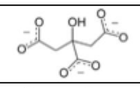	Highly negative	• Common capping agent • Easily displaceable with other molecules
Polyethyleneglycol (PEG)	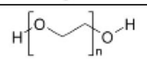	Neutral	• Commonly used for compatibility in biological systems
Branched polyethyleneimine (BPEI)	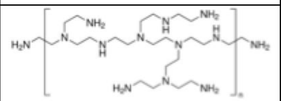	Highly positive	• Highly aminated, positively charged organic surface coating • Large number of free amines

Experiments and Results

A. Analysis of Particle Aggregation:

- DLS results estimate average particle size in water.
- Data on Silver NP-human serum albumin (HSA) interaction studies indicate that particle aggregation is primarily dependent upon protein coating.
- Ag NPs with a PEG surface tended to aggregate more dramatically, even with no protein incorporated (**Figure 1b)**.
- Zeta potential has an influence on NP's affinity to aggregate (**Table 2)**.

Figure 1a

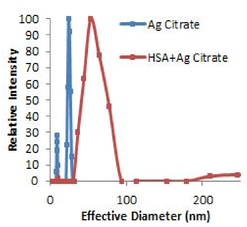

Figure 1b

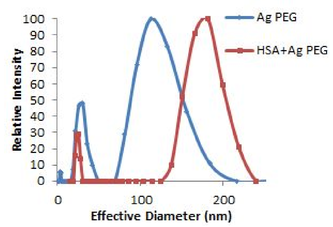

Figure 1c

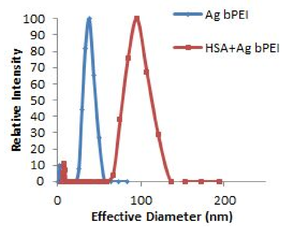

Figure 1a-1c: DLS Sizing Comparison of Ag NPs with and without HSA Protein. Figures 1a, b, and c compare the effective diameters of Ag NPs with Citrate, PEG, and bPEI surface coatings, respectively. This set of figures is designed to exhibit signs of aggregation upon the incorporation of HSA protein

B. Toxicity Testing Using a Human Hepatic Cell Line (HepG2)

HepG2 cells were plated at a concentration of 15,000 cells/well and allowed to grow for 24 hours before Ag Np's with protein coatings labeled in graph (**Figure 2**) were added to the media. WST assays were run each day for three days.

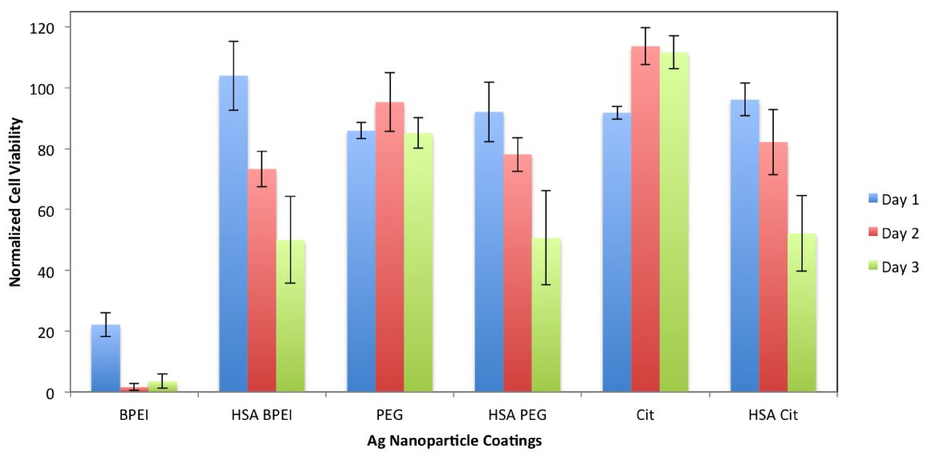

Figure 2. Trends of Ag NP Toxicity on HepG2 Cells. Raw data was normalized against no nanoparticle controls. Averages calculated based on n=4 and N=3. Statistical significance calculated using mean±SEM.

Conclusions and Future Plans

A. Particle behavior in solution

- DLS measured average hydrodynamic radius of particles upon exposure to HSA.
- Results revealed a tendency that Ag NPs will aggregate more when exposed to HSA protein.
- PEG coated Ag NPs aggregated most dramatically, which might be caused by the neutral zeta-potential of PEG.
- Degree of particle aggregation depends mostly upon the incorporation of HSA, but is also influenced by the NP engineered surface coating.

B. Role of the ENM protein corona in biological response to ENM surface coatings.

- BPEI-coated particles are toxic; but HSA protects cells from the toxicity of BPEI coatings.
- PEG and citrate coated particles are non toxic; however HSA coating on the PEG and citrate coated particles leads to toxicity.

C. Short Term Goals/Future Directions

- Begin full examination of NP-protein binding across a matrix of four blood proteins and five medically relevant NP surfaces, using data gathered by DLS, and fluorescence anisotropy.
- Protein unfolding will also be used to monitor NP effects on protein structure, e.g. circular dichroism measurements of protein structure.
- Other methods will be used to quantify proteins at the surface of NPs, including SDS PAGE quantification of the hard corona and TEM imaging of the protein coating.
- Coat NPs with transferrin, fibrinogen, and apolipoprotein A1 and evaluate the toxicity using HepG2 cells.

C. Long Term Future Directions

- Coat NPs with peptides found in fibrinogen (**Figure 3)**, and evaluate the toxicity using HepG2 cells.
- This peptide is known to suppress relapsing paralysis in multiple sclerosis (MS):

Gamma-Fibrinogen (377-395) YSMKETTMKIIPFNRLSIG

Gamma-Fibrinogen scrambled (377-395) KMMISYTFPIERTGLISNK

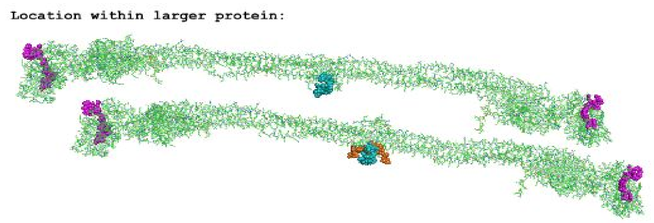

Figure 3: Diagram of Fibrinogen Protein. The Gamma-Fibrinogen (377-395) sequence is highlighted in pink.

Hydrodynamic Capture of Particles by Micro-swimmers under Hele-Shaw Flows

Grant Mishler[1], Alan Cheng Hou Tsang[2], and On Shun Pak[1]

[1]Department of Mechanical Engineering, Santa Clara University. [2]Department of Bioengineering, Stanford University.

Introduction

Understanding the hydrodynamic interactions among swimming microorganisms is an important step towards the control of micro-particles and micro-swimmers. A model accounting for the interactions between a motile and a non-motile particle was developed and investigated analytically and numerically.

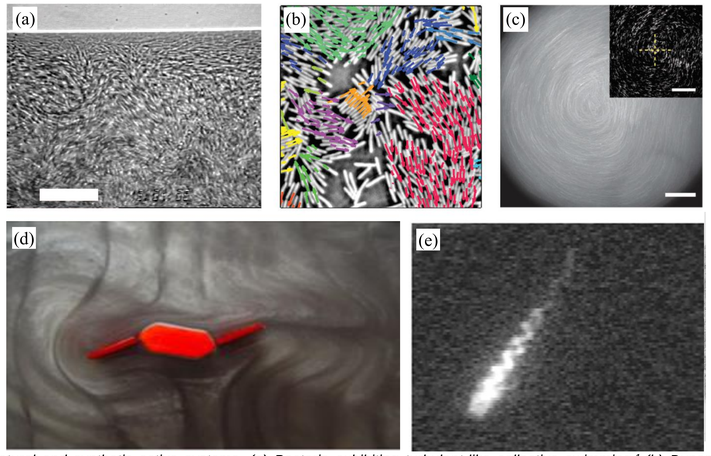

Natural and synthetic active systems. (a) Bacteria exhibiting turbulent-like collective swimming.[1] (b) Dynamic clusters of bacteria.[2] (c) Swirling pattern of actin filaments.[3] (d) Purcell swimmer, a bluff-bodied swimmer.[4] (e) Swimming bacterial E.coli, a slender-bodied swimmer.[5]

We have identified a novel capture mechanism of passively-driven particles by micro-swimmers in confined microfluidic environments. The mechanism may find potential applications in self-assembly of particles and targeted drug delivery by micro-swimmers.

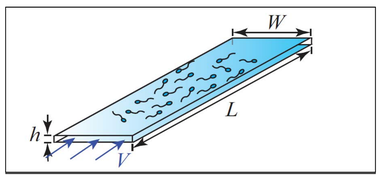

Micro-swimmers in a Hell-Shaw channel

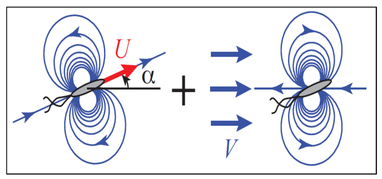

Potential Dipoles of active and driven particles

Problem Formulation

In a Hele-Shaw flow environment, the flow of an active and driven particles can be modeled as a 2D potential dipole. The dynamics of particles can be described by the interaction of the potential dipoles.

Non-motile particle:

$$\dot{\bar{z}}_n = \mu \frac{\sigma_m e^{-i\alpha_m}}{(z_n - z_m)^2} + f_0 \left(\frac{k}{|z_n - z_m|}\right)^{13} \frac{(\bar{z}_m - \bar{z}_n)}{|\bar{z}_m - \bar{z}_n|} + \mu V$$

Velocity induced by motile particle | Steric repulsion | Background flow

Motile particle:

$$\dot{\bar{z}}_m = U_m e^{-i\alpha_m} + \mu \frac{\sigma_n}{(z_m - z_n)^2} + f_0 \left(\frac{k}{|z_n - z_m|}\right)^{13} \frac{(\bar{z}_n - \bar{z}_m)}{|\bar{z}_n - \bar{z}_m|} + \mu V$$

Propulsion velocity | Velocity induced by non-motile particle | Steric repulsion | Background flow

$$\dot{\alpha}_m = Re\left[-\nu \frac{2i\sigma_n e^{2i\alpha_m}}{(z_m - z_n)^2}\right]$$

Jeffery's Orbit

μ: Translational Mobility Coefficient
ν: Rotational Mobility Coefficient

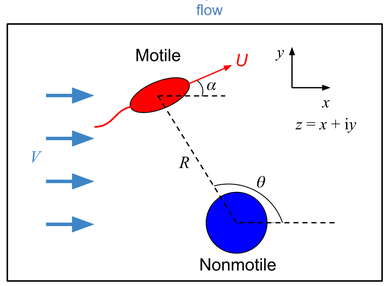

Results

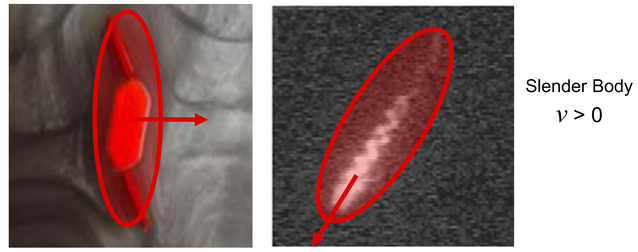

Time-lapse of successful and failed capture scenarios by varying the background flow. In the capturing cases, the equilibrium configuration depends on body geometry of the swimmer.

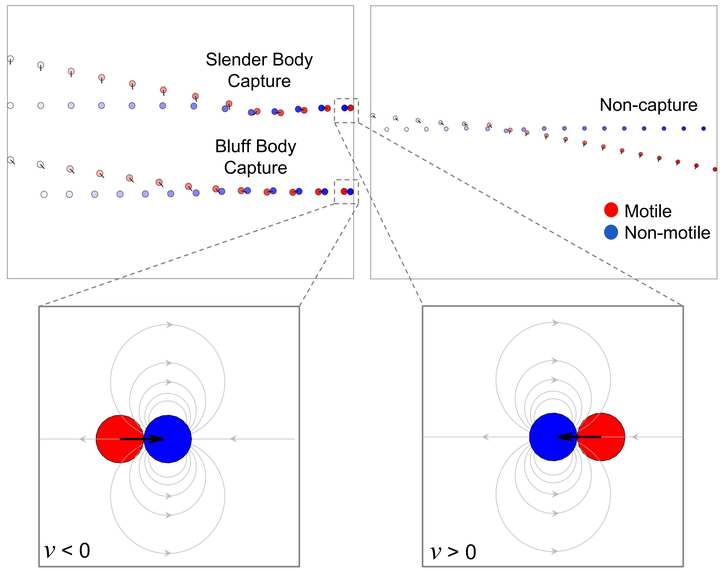

There exists a minimum background flow intensity for the equilibrium configuration to be stable. The stability of the equilibrium configuration is investigated through a linear stability analysis and direct numerical simulations.

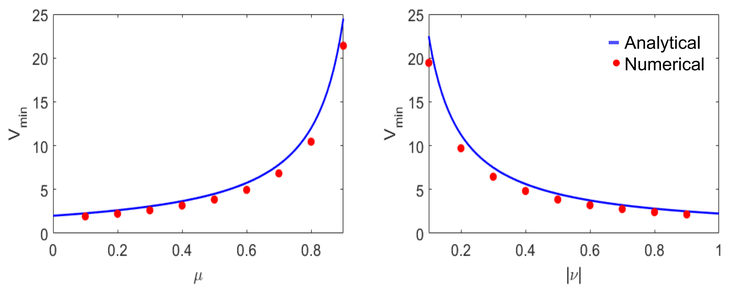

Acknowledgements

Santa Clara University
School of Engineering

This work was partially funded by:

Arthur Hull Hayes, Jr. and Family Endowed Fellowship Fund

Phase Diagrams

We summarized the conditions of successful capturing and mapped the results onto a set of phase diagrams (α-θ, R-θ) at different background flow intensity, V.

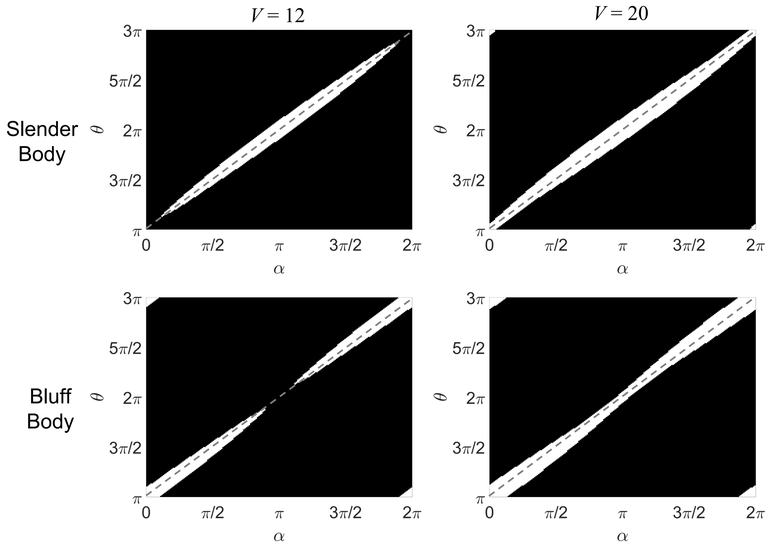

Distance between particles is fixed at R = 20.

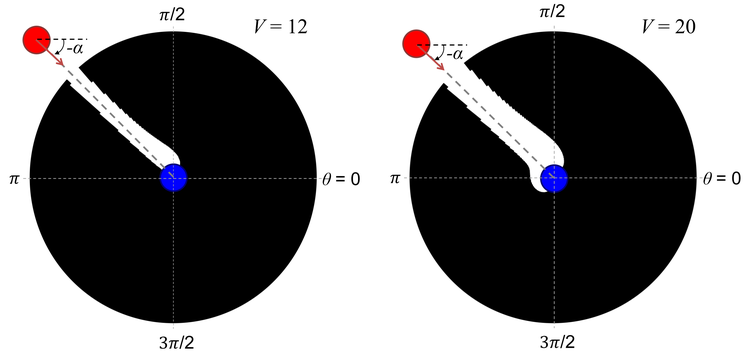

Orientation of the swimmer is fixed at $\alpha = -\pi/4$.

The gray lines in the capture regions correspond to the case where the swimmer is pointed toward the driven particle.

Conclusion

We identified a novel capture mechanism of driven particles by micro-swimmers in confined microfluidic environments. This capture mechanism is mediated by the hydrodynamic interactions between the micro-swimmers, the driven particles, and the background flow.

We determined that beyond a critical background flow intensity, there exists a stable equilibrium configuration of the particles that depends on the body geometry of the swimmer. This stable equilibrium configuration forms the basis of the capture mechanism.

We further investigated the conditions of successful capturing as a function of the distance between the particles, the orientation of the swimmer, and the intensity of the background flow, hence verifying the robustness of the capture mechanism.

This work forms the theoretical basis for subsequent investigations of collective behaviors in systems with active and passive particles, with potential applications in particle self-assembly, capture and delivery of therapeutic nanoparticles, and understanding hydrodynamic interactions in biological active-inactive systems.

References

[1] C. Dombrowski, L. Cisneros, S. Chatkaew, R. E. Goldstein, and J. O. Kessler. *PRL*, 93(9):098103, 2004.
[2] H. P. Zhang, A. Be'er, E.-L. Florin, and H. L. Swinney. *PNAS*, 107(31):13626{13630, 2010.
[3] V. Schaller, C.Weber, C. Semmrich, E. Frey, and A. R. Bausch. *Nature*, 467(7311):73{77, 2010.
[4] E. Lauga, T. Powers. *Reports on Progress in Physics*. 72(9). December 2008.
[5] L. Turner, W. Ryu, H. Berg. *Journal of Bacteriology*. 182(10). May 2000.

Deep Network Optimization for Wearable Computing

Haofeng Kou, Yi Fang, Weijia Shang

Computer Engineering Department Santa Clara University

Magic Leap

Santa Clara University School of Engineering

Santa Clara University School of Engineering

BACKGROUND

Deep Compress

We introduce a three stage pipeline to optimize the neural networks for wearable computing by over 100× without affecting their accuracy

- Pruning
- Quantization
- Platform Optimization

Pruning

- Regularization
- Local Pruning and Parameter Co-adaptation
- Dropout
- Iterative Pruning
- Pruning Neurons
- Pruning Network

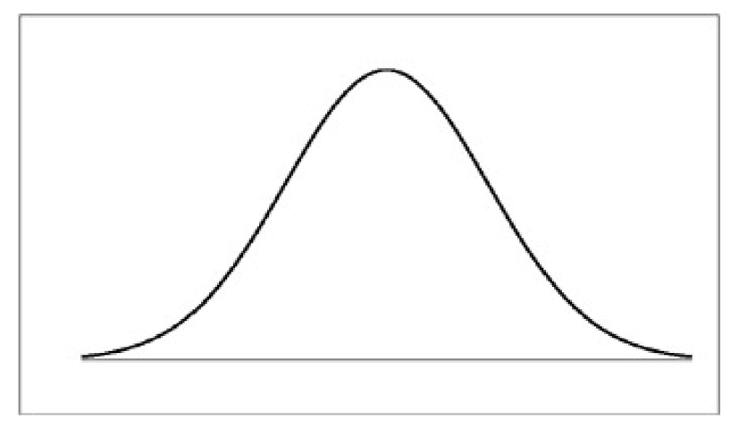

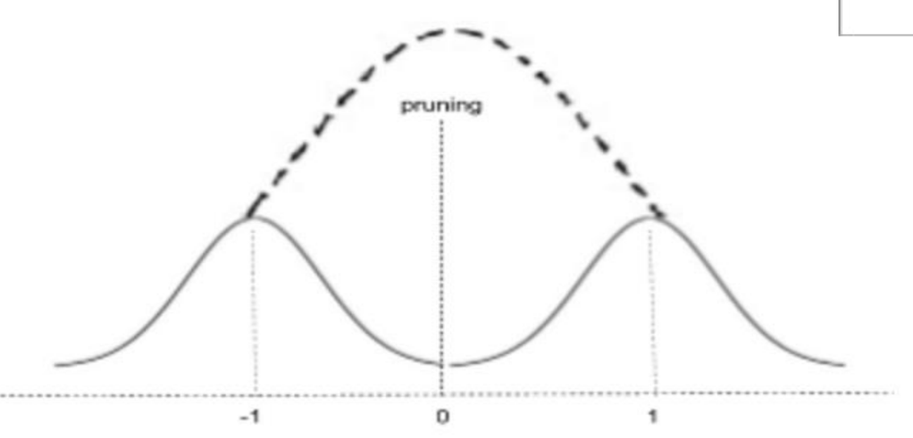

Quantization

- Binary Weight Network
- Mixed Precision Activation

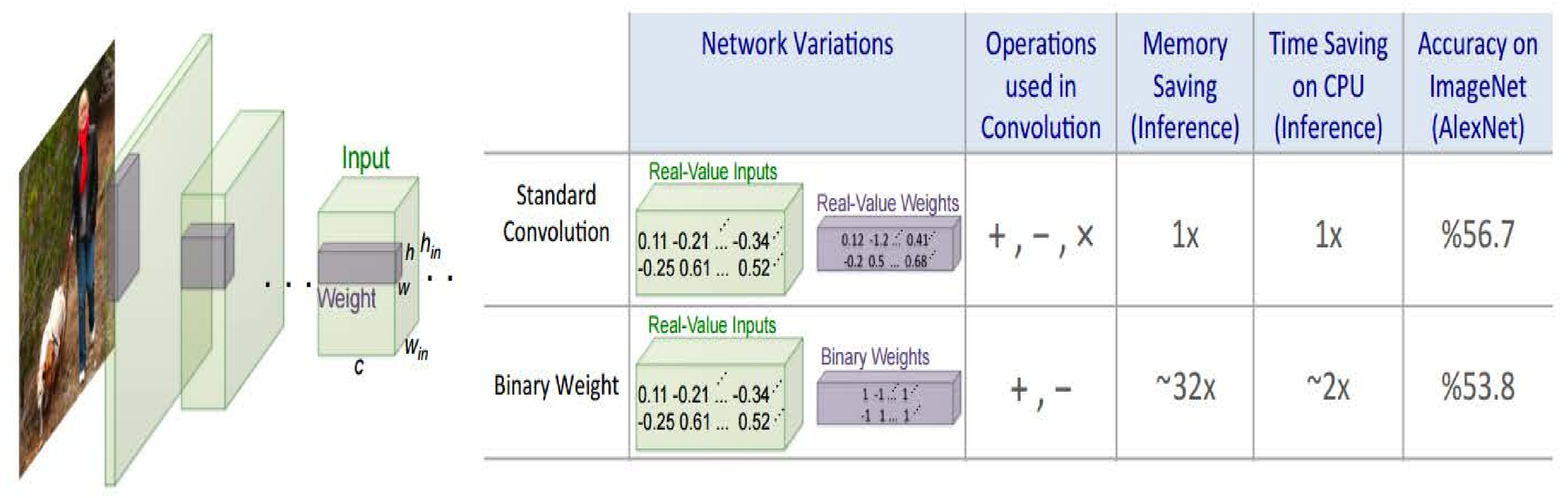

Platform Optimization

Task Driven Plan

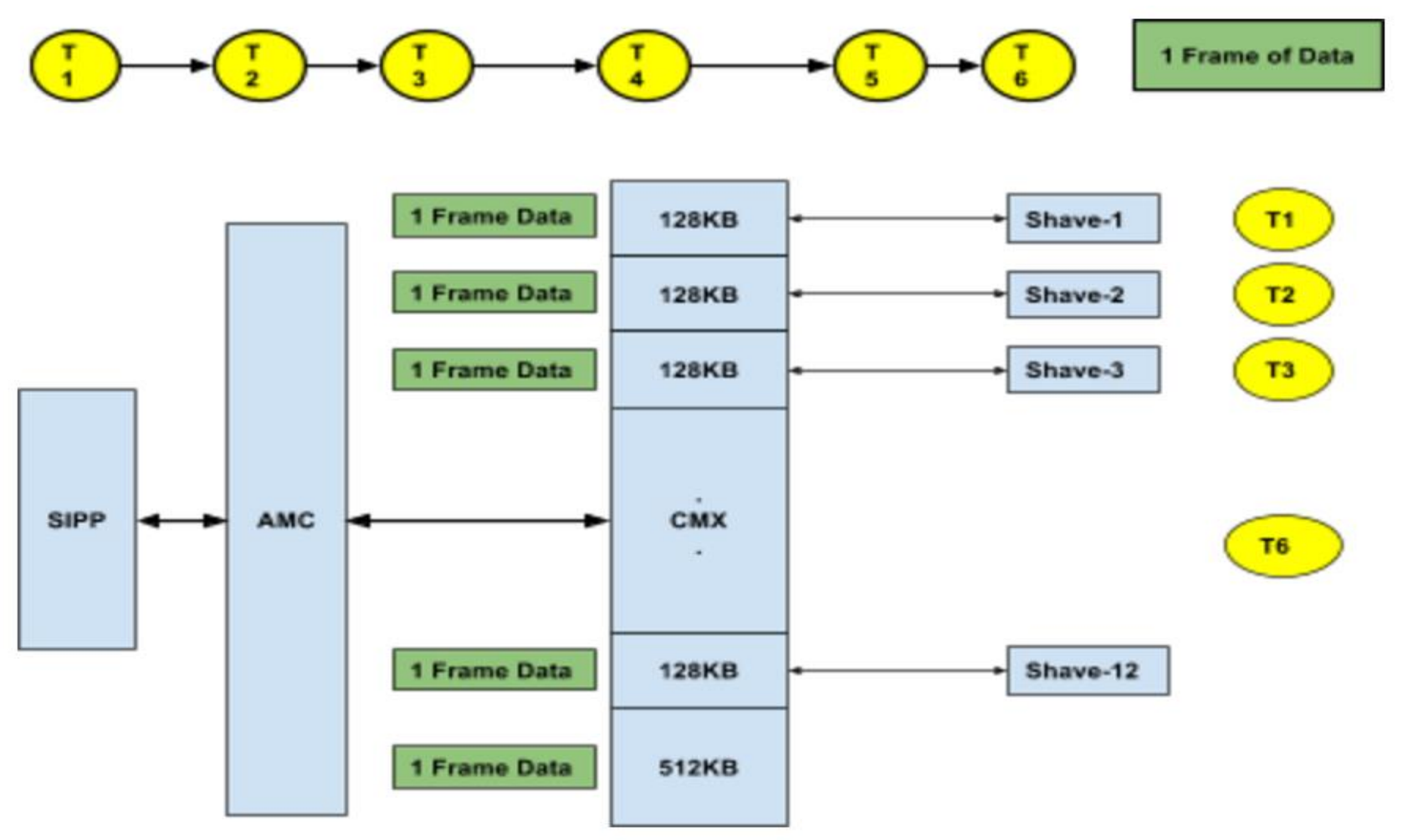

Data Driven Plan

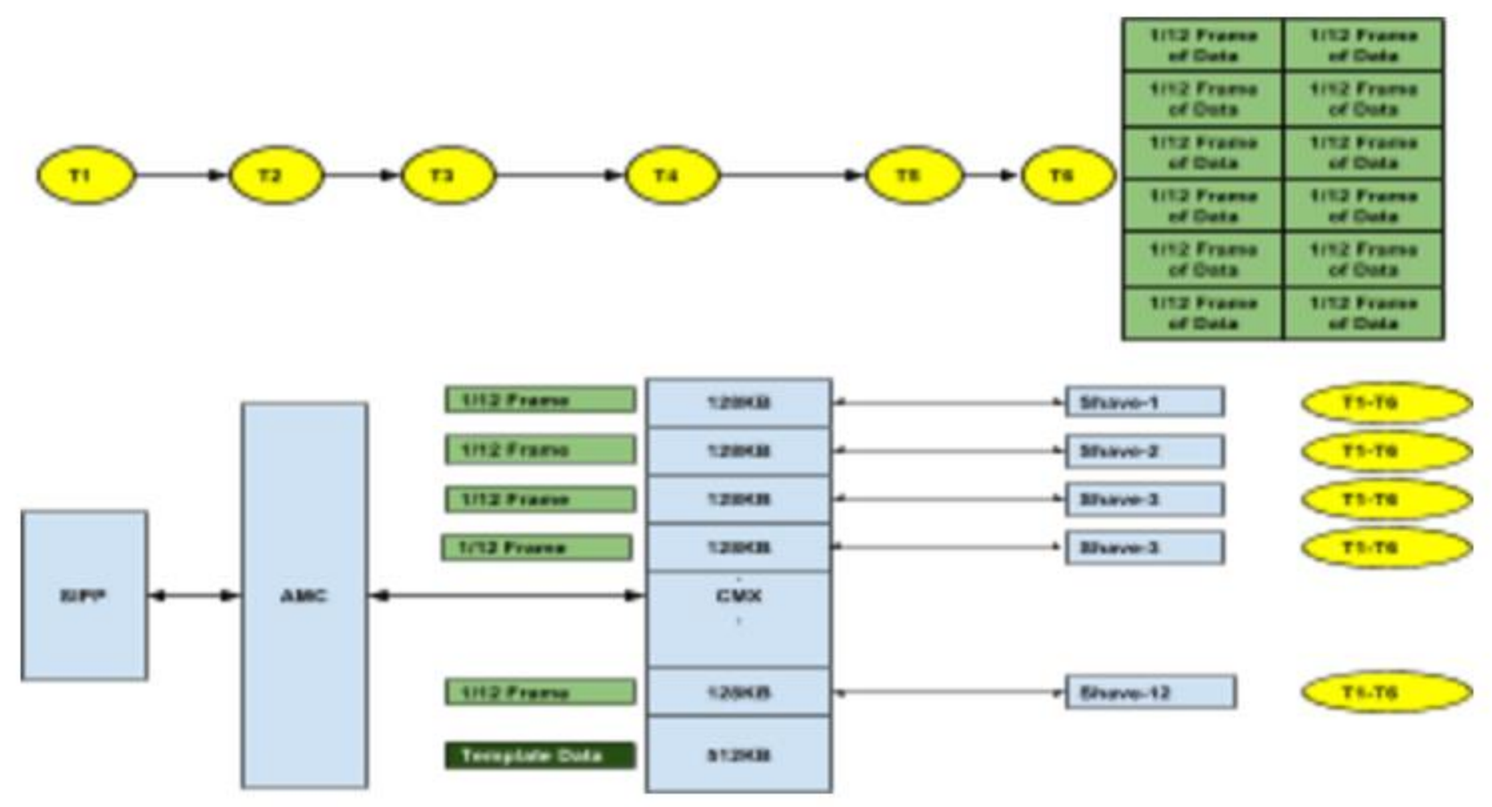

DETAIL IMPLEMENTATION

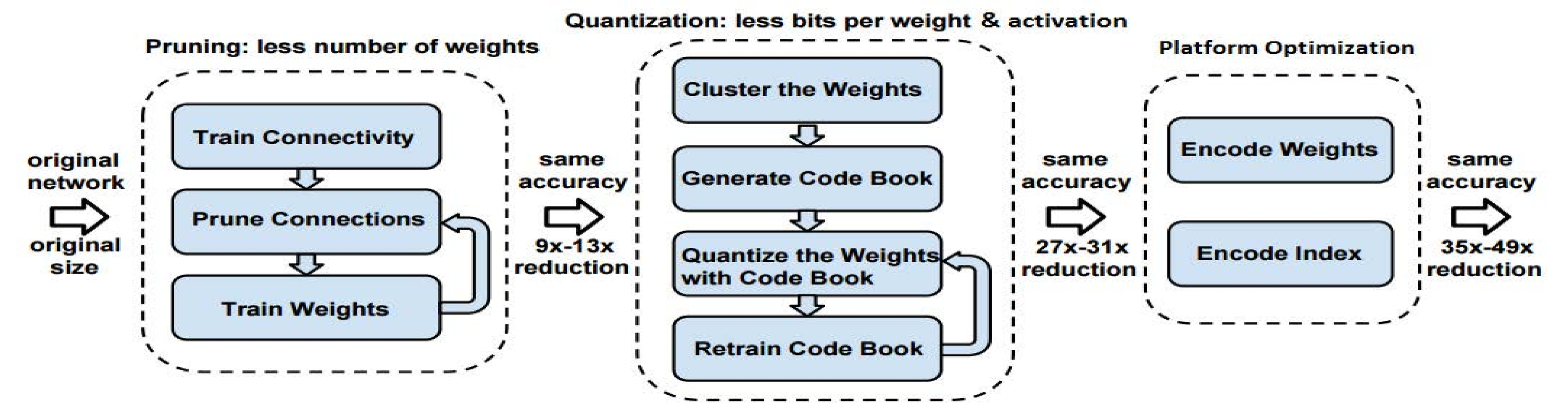

Deep Compression Software Sequence

Requirement Analysis

Size of network & data:	Fit into low-power wearable computation
Power Consumption:	Less than or equal to 1W
Hardware limitation:	DDR: 2G CMX: 2M Computation Units: 12

Challenge 1:

Weights and Activation Compression

This is a general topic for all deep networks on wearable device and every programmer, sooner or later, does face this issue.

Solution 1:

Our approach is to implement binary weights and mixed precision activations:

Mixed precision quantization, for example the activation is represented in the format of the sum of multiple power-of-2 data, which can be in 32 bits, 16 bits or 8 bits. Instead of calculating the activation first and then computing with weights, our approach is to quantitate the activation into multiple pieces in term of mixed precision, compute each of these power-of-2 partial activation with weights in parallel and then sum together. By taking this approach, we remove all multiply and only compute in add/subtract.

Challenge 2:

Data and Task scheduling and parallel computing

This is another general topic for all deep networks on wearable device and every programmer, sooner or later, does face this issue.

Solution 2:

Tile scheduling and parallel computing.

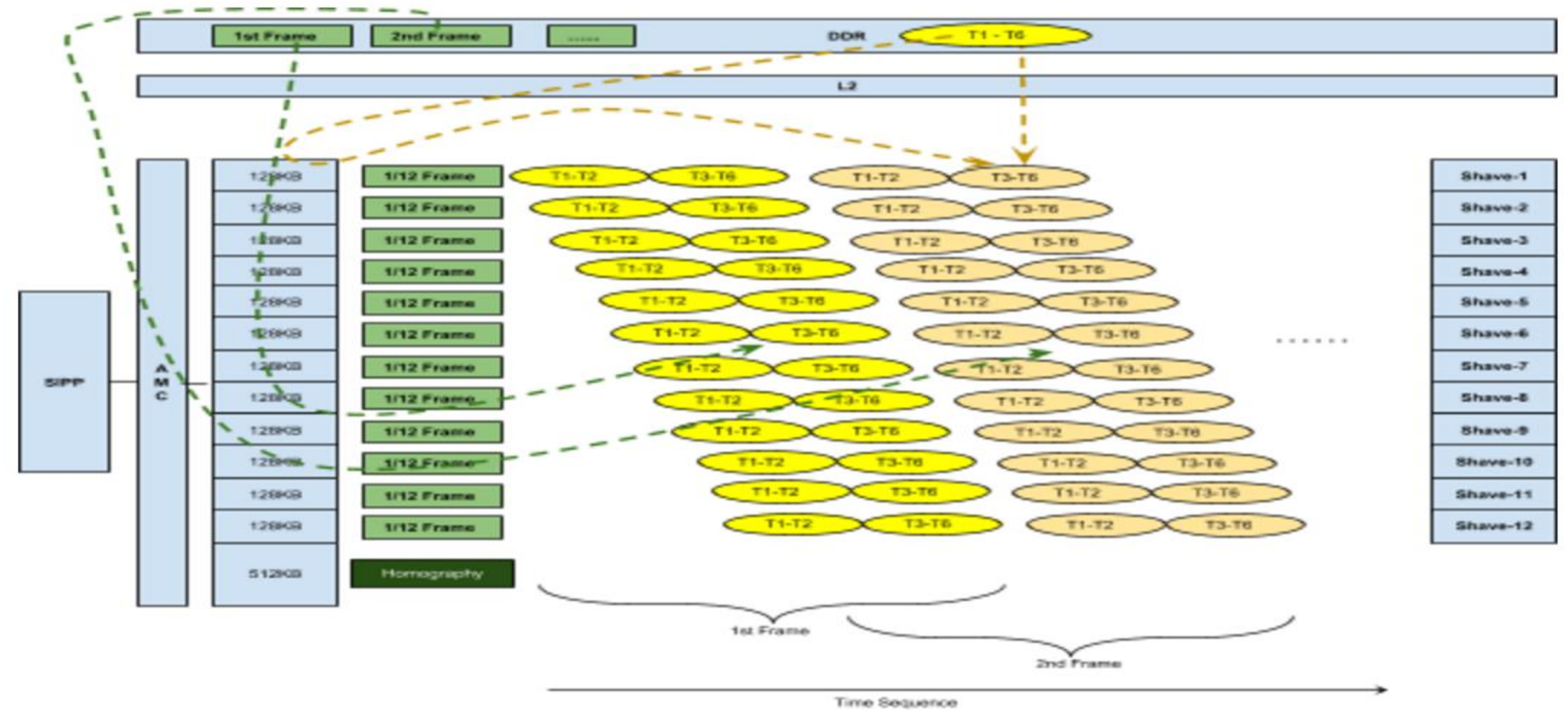

RESULTS

CaffeNet on M2

Layer	Name	MFLOPs	Bandwidth MB/s	time(ms)
0	conv1	210.830	82.48	433.63
1	pool1	0.630	235.85	2.35
2	norm1	0.000	17.34	7.70
3	norm1_s0	0.000	1423.21	0.05
4	conv2_p0	223.949	103.99	34.97
5	norm1_s1	0.000	1224.71	0.05
6	conv2_p1	223.949	103.99	34.97
7	pool2	0.389	236.85	1.50
8	norm2	0.000	10.20	8.09
9	conv3	299.041	51.09	47.57
10	conv3_s0	0.000	1524.30	0.04
11	conv4_p0	112.140	96.39	18.16
12	conv3_s1	0.000	1552.06	0.04
13	conv4_p1	112.140	96.39	18.16
14	conv4_p0_s0	0.000	1333.41	0.05
15	conv5_p0	74.760	126.31	12.18
16	conv4_p0_s1	0.000	1348.21	0.05
17	conv5_p1	74.760	126.34	12.17
18	pool5	0.083	221.39	0.37
19	fc6	0.018	2078.60	34.65
20	fc7	0.008	2065.92	15.49
21	fc8	0.008	2541.97	3.08
22	prob	0.003	10.00	0.19
	Total inference time			685.50

LeNet on M2

Layer	Name	MFLOPs	Bandwidth MB/s	time(ms)
0	conv1	5.530	111.47	2.78
1	pool1	0.014	228.79	0.12
2	conv2	4.301	119.59	1.92
3	pool2	0.004	148.54	0.05
4	ip1	0.002	1941.00	0.44
5	ip2	0.001	402.33	0.03
6	softmax	0.000	0.75	0.03
	Total inference time			5.35

HomographyNet on M2

Layer	Name	MFLOPs	Bandwidth MB/s	time(ms)
0	Convolution1	37.749	8.39	67.47
1	Convolution2	1207.960	89.94	200.93
2	Pooling1	1.049	450.83	4.44
3	Convolution3	301.990	90.60	50.46
4	Convolution4	301.990	90.61	50.45
5	Pooling2	0.262	434.44	1.15
6	Convolution5	150.995	49.87	25.39
7	Convolution6	301.990	54.06	46.84
8	Pooling3	0.131	388.22	0.64
9	Convolution7	75.497	70.88	11.91
10	Convolution8	75.497	70.95	11.90
11	Pooling4	0.033	298.03	0.21
12	InnerProduct1	0.016	1989.10	8.05
13	relu_xform_2	0.002	2026.15	0.14
	Total inference time			479.98

GoogleNet on M2

Layer	Name	MFLOPs	Bandwidth MB/s	time(ms)
0	conv1/7x7_s2	236.028	278.24	50.65
1	pool1/3x3_s2	1.806	618.49	2.48
2	conv2/3x3	693.633	33.00	110.82
3	pool2/3x3_s2	1.355	613.25	1.87
4	inception_3a/1x1	19.268	102.68	3.03
5	inception_3a/3x3_reduce	28.901	72.22	4.46
6	inception_3a/3x3	173.408	55.18	27.28
7	inception_3a/5x5_reduce	4.817	341.21	0.86
8	inception_3a/5x5	20.070	176.13	3.54
9	inception_3a/pool	1.355	304.22	0.94
10	inception_3a/pool_proj	9.634	190.36	1.57
11	inception_3b/1x1	51.380	55.49	8.03
12	inception_3b/3x3_reduce	51.380	55.60	8.01
13	inception_3b/3x3	346.817	41.57	51.67
14	inception_3b/5x5_reduce	12.845	193.16	2.06
15	inception_3b/5x5	120.422	71.61	18.81
16	inception_3b/pool	1.806	288.69	1.33
17	inception_3b/pool_proj	25.690	101.92	4.06
18	pool3/3x3_s2	0.847	519.74	1.38
19	inception_4a/1x1	36.127	59.21	6.01
20	inception_4a/3x3_reduce	18.063	88.06	3.04
21	inception_4a/3x3	70.447	59.63	11.23
22	inception_4a/5x5_reduce	3.011	299.62	0.65
23	inception_4a/5x5	7.526	122.49	1.54
24	inception_4a/pool	0.847	226.26	0.79
25	inception_4a/pool_proj	12.042	115.22	2.07
26	inception_4b/1x1	32.113	70.15	4.96
27	inception_4b/3x3_reduce	22.479	80.26	3.75
28	inception_4b/3x3	88.510	56.73	14.30
29	inception_4b/5x5_reduce	4.817	249.96	0.86
30	inception_4b/5x5	15.053	107.96	2.78
31	inception_4b/pool	0.903	224.27	0.85
32	inception_4b/pool_proj	12.845	123.45	2.06
33	inception_4c/1x1	25.690	79.32	3.99
34	inception_4c/3x3_reduce	25.690	79.40	3.99
35	inception_4c/3x3	115.606	55.19	18.08
36	inception_4c/5x5_reduce	4.817	249.86	0.86
37	inception_4c/5x5	15.053	107.98	2.78
38	inception_4c/pool	0.903	224.38	0.85
39	inception_4c/pool_proj	12.845	123.56	2.06
40	inception_4d/1x1	22.479	80.14	3.76
41	inception_4d/3x3_reduce	28.901	72.53	4.58
42	inception_4d/3x3	146.313	53.79	22.33
43	inception_4d/5x5_reduce	6.423	205.49	1.08
44	inception_4d/5x5	20.070	107.94	3.70
45	inception_4d/pool	0.903	224.54	0.85
46	inception_4d/pool_proj	12.845	123.48	2.06
47	inception_4e/1x1	52.986	56.42	8.08
48	inception_4e/3x3_reduce	33.116	70.51	5.09
49	inception_4e/3x3	180.634	51.99	27.37
50	inception_4e/5x5_reduce	6.623	206.25	1.11
51	inception_4e/5x5	40.141	71.24	7.03
52	inception_4e/pool	0.931	225.37	0.88
53	inception_4e/pool_proj	26.493	79.65	4.10
54	pool4/3x3_s2	0.367	413.41	0.75
55	inception_5a/1x1	20.873	119.51	4.05
56	inception_5a/3x3_reduce	13.046	133.50	2.48
57	inception_5a/3x3	45.158	127.84	7.97
58	inception_5a/5x5_reduce	2.609	213.56	0.60
59	inception_5a/5x5	10.035	126.47	2.18
60	inception_5a/pool	0.367	149.88	0.52
61	inception_5a/pool_proj	10.437	134.92	2.08
62	inception_5b/1x1	31.310	114.15	6.03
63	inception_5b/3x3_reduce	15.655	124.59	3.07
64	inception_5b/3x3	65.028	126.70	11.32
65	inception_5b/5x5_reduce	3.914	170.78	0.90
66	inception_5b/5x5	15.053	129.53	3.17
67	inception_5b/pool	0.367	148.54	0.52
68	inception_5b/pool_proj	10.437	134.89	2.08
69	pool5/7x7_s1	0.100	238.60	0.40
70	loss3/classifier	0.002	2442.29	0.80
71	prob	0.003	9.99	0.19
	Total inference time			531.49

CONCLUSIONS

Our deep compression shows up to **~100** times faster than general CPU version for large amount of data.

Not only the performance, but also the size of network & data, as well as the power consumption are all considered and covered in our research implementation.

FUTURE WORKS

Further breakdown and dive into other deep networks to implement the automatic optimization on embedded SOC platforms.

Besides Myriad2, Tensilica, CEVA and CUDA are also on the list of evaluation.

printed by MegaPrint INC. www.postersession.com

Electro-deformation of a Vesicle

H. Nganguia and O. S. Pak[1], Y.-N. Young[2], and W.-F. Hu and M.-C. Lai[3]

[1]Department of Mechanical Engineering, Santa Clara University

[2]Department of Mathematical Sciences, New Jersey Institute of Technology

[3]Department of Mathematical Sciences, National Chiao Tung University, Taiwan

Objectives

We develop a code based on the second-order Immersed Interface Method (IIM) to simulate the deformation and dynamics of vesicle under a DC electric field. We validate the code by simulating the shape transitions reported in literature (oblate-prolate and prolate-oblate-prolate).

Introduction

Vesicles are closed lipid bilayer membranes that have been used extensively as the most basic model of biological cells.

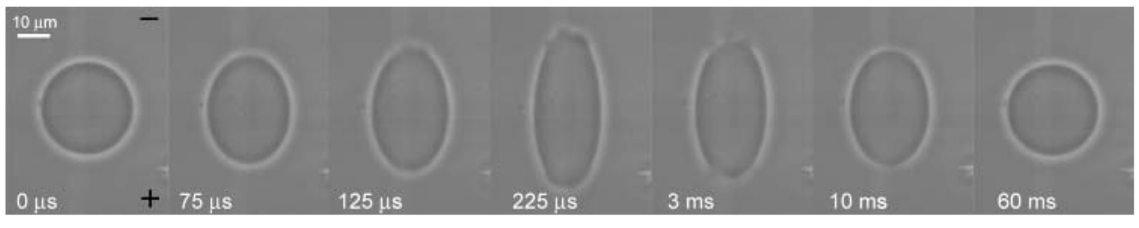

Vesicles electrohydrodynamics is concerned with the dynamics of vesicles under an electric field. It has received increasing attention due to its wide applications in both biological and biomedical systems, such as electroporation [1] and electrofusion [2] to name a few.

Formulation

The deformation of a vesicle under DC electric field is described by a set of PDEs for the flow field,

$$\nabla p + \mu \nabla^2 \boldsymbol{u} + \boldsymbol{f} = 0, \tag{1}$$
$$\nabla \cdot \boldsymbol{u} = 0, \tag{2}$$
$$\boldsymbol{f}(\boldsymbol{x},t) = \int_\Sigma (\boldsymbol{F}_\gamma + \boldsymbol{F}_b + \boldsymbol{F}_E)(s,t)\delta(\boldsymbol{x} - \boldsymbol{X}(s,t))ds, \tag{3}$$
$$\frac{\partial \boldsymbol{X}}{\partial t}(s,t) = \boldsymbol{U}(s,t) = \int_\Omega \boldsymbol{u}(\boldsymbol{x},t)\delta(\boldsymbol{x} - \boldsymbol{X}(s,t))d\boldsymbol{x}, \tag{4}$$
$$\nabla_s \cdot \boldsymbol{U} = 0, \tag{5}$$

and for the electric potential,

$$\nabla \phi = 0, \tag{6}$$
$$[\![\sigma]\!] = V_m(s,t), \tag{7}$$
$$[\![\sigma \phi_n]\!] = 0, \tag{8}$$
$$C_m \frac{\partial V_m}{\partial t} + G_m V_m = \sigma^+ \phi_n^+ = \sigma^- \phi_n^-. \tag{9}$$

Method

The Immersed Interface Method (IIM) was developed to solve two-phase flow problems. It has second-order convergence, and presents many advantages over more widely used numerical methods: more time-efficient compared to the Finite Element method (FEM), and unlike the Boundary Element Method (BEM) is easily adaptable to various situations. The IIM differentiates nodes of the discretized problem into regular and irregular points. A standard Finite Difference Method (FDM) is applied at regular points. At irregular points, a new difference scheme that incorporates jumps at interfaces is derived.
The current scheme is built upon our previous work [3, 4].

OP Transition

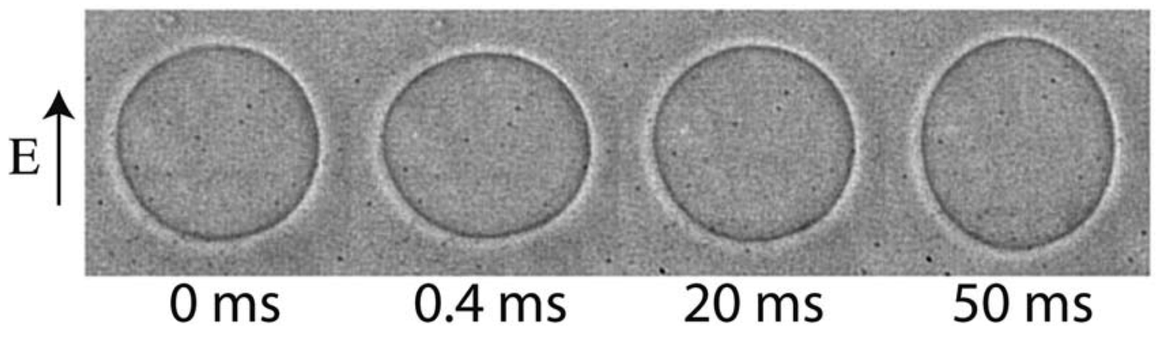

Convergence study

The time step is set as $\Delta t = 10^{-6}$. Simulations up to $T = 10^{-2}$. The ratio is defined as

$$\text{ratio} = \log_2 \left(\frac{\|u_{2N} - u_N\|}{\|u_{4N} - u_{2N}\|} \right). \tag{10}$$

N	$\|u_{2N} - u_N\|_\infty$	ratio	$\|w_{2N} - w_N\|_\infty$	ratio	$\|\boldsymbol{X}_{2N} - \boldsymbol{X}_N\|_\infty$	ratio
32	73.81	-	103.58	-	3.22×10^{-2}	-
64	2.73	4.76	4.77	4.44	1.16×10^{-3}	4.79
128	9.51×10^{-2}	4.84	1.41×10^{-1}	5.08	2.78×10^{-5}	5.39

Simulations

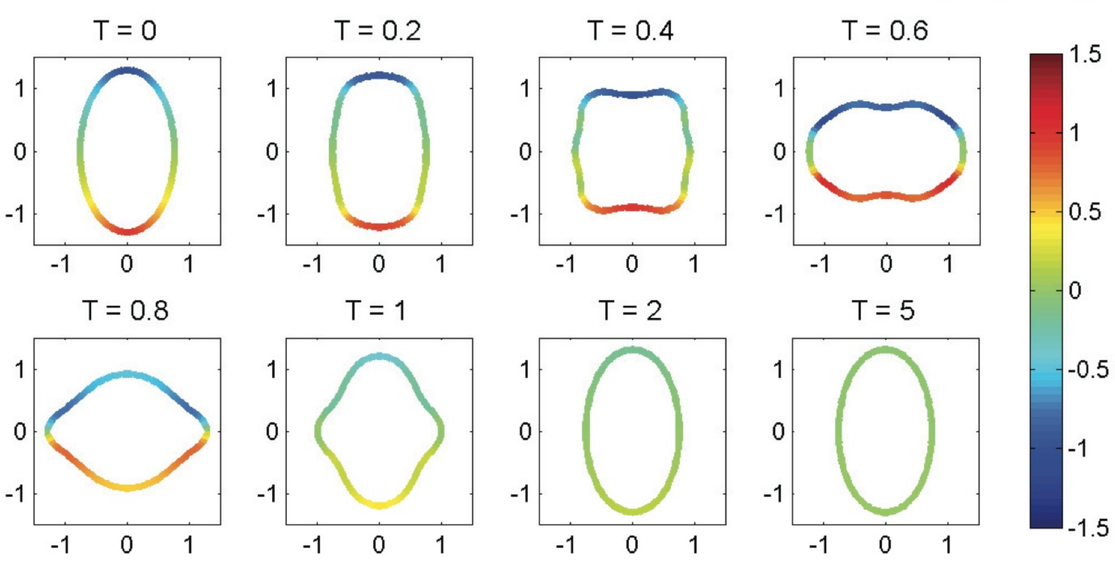

Investigations are ongoing to analyze the effects of inertia and membrane structure (conductance) on 3D axisymmetric vesicles under DC electric field.

References

[1] R. L. Knorr, M. Staykova, R. S. Gracia, and R. Dimova. Wrinkling and electroporation of giant vesicles in the gel phase. *Soft Matter*, 6:1990–1996, 2010.

[2] C. K. Haluska, K. A. Riske, V. Marchi-Artzner, J.-M. Lehn, R. Lipowsky, and R. Dimova. Time scales of membrane fusion revealed by direct imaging of vesicle fusion with high temporal resolution. *Proc. Nat. Acad. Sci.*, 103:15841–15846, 2006.

[3] H. Nganguia, Y.-N. Young, A. T. Layton, W.-F. Hu, and M.-C. Lai. An immersed interface method for axisymmetric electrohydrodynamic simulations in stokes flow. *Commun. Comput. Phys.*, 18:429–449, 2015.

[4] W.-F. Hu, M.-C. Lai, Y. Seol, and Y.-N. Young. Vesicle electrohydrodynamic simulations by coupling immersed boundary and immersed interface method. *J. Comput. Phys.*, 317:66–81, 2016.

LaTeX TikZposter

Knowledge Base Research at SCU

Faculty Research Advisor
Dr. Yi Fang

Hung Nguyen
Department of Computer Engineering
Santa Clara University
h2nguyen@scu.edu

Santa Clara University
School of Engineering

Motivation

- The original information of an entity in the knowledge base is outdated when some events happen, and it needs to be updated.
- New piece of information becomes available for interested entities. This piece of information will need to be added into the knowledge base on time.
- Determine accurate information that needs to be added or updated for entities.

Problem Statement

Given an entity, perform the search in available data sets (corpus, web, …) to detect its relations with other entities.

Tasks

- CCR: Cumulative Citation Recommendation
- SSF: Streaming Slot Filling

Data Set

- KGA Stream Corpus 2014
- 16.1 TB after compression
- 639 GB after filtered by entities and slot name
- Contains 20,494,260 stream items

System

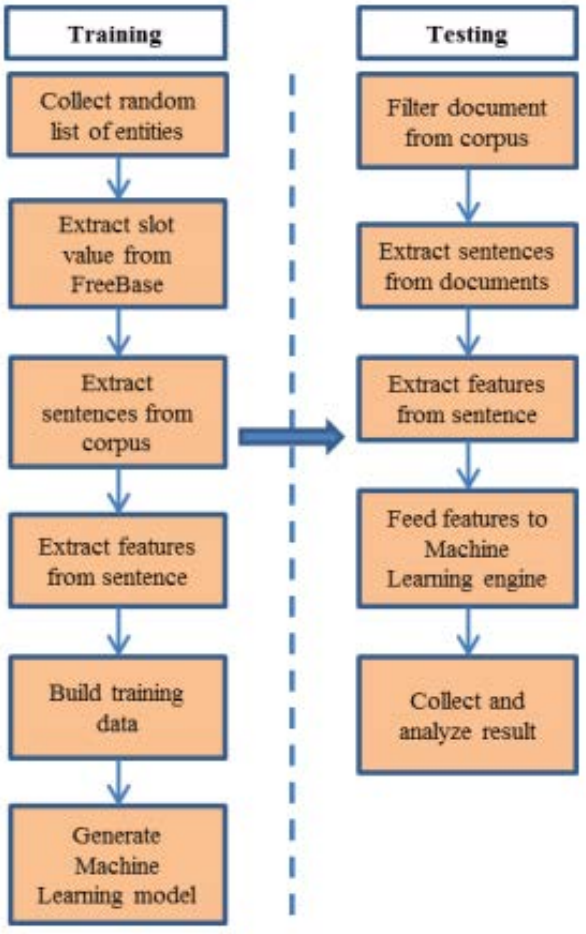

Future Work

- Apply deep learning after extracting features
- Fine tune the model
- Add distance supervise learning

Challenges

- Limited ground truth data

Deep Learning

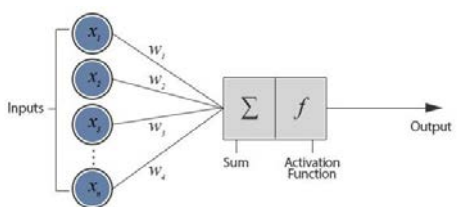

Exposing Privacy Risks on Social Media

Isabela Figueira, Archana Godavarthy, Prof. Yi Fang
Computer Engineering Department

Santa Clara University
School of Engineering

Introduction:

The info social media users post can be used to learn about the user's personal lives.

Objectives:

Use machine learning to learn user traits from their tweets in order to uncover social media privacy risks.

Why bother?

Now, it doesn't seem like such a threat. But give it time!
Machine learning will be able to be used to parse the vast amounts of data we volunteer about ourselves and learn about things we don't even know we don't want shared with the world.
Who knows what future threats to our data there are.

Traits in question:

Married (1) vs unmarried (0)
Democrat (1) and Republican (0)

The Process:

- Scrape Twitter stream
- Get users meeting criteria
- Preprocess their tweets
- Train an algorithm that maps a small selection of users to their positive or negative trait
- Test the algorithm on more users we know the traits of and analyze results

Next Step:

After training the data to uncover the relationship, we want to find a way to change the data so the algorithm no longer works to protect people's privacy

Collect and preprocess data → Train and analyze data → Change the tweets so that the trained algorithm is now ineffective

Fuzzy Model-Based Control of Spacecraft with Fuel Sloshing Dynamics

Ph.D. Candidate: Lilit Mazmanyan
Thesis Advisor: Dr. Mohammad A. Ayoubi
Department of Mechanical Engineering, Santa Clara University

Santa Clara University
School of Engineering

Abstract

We present a Takagi-Sugeno (T-S) observer-based fuzzy controller which stabilizes the attitude of spacecraft with a partially-filled fuel tank while it satisfies the control input constraint. First, the nonlinear equations of motion of spacecraft with a liquid fuel store are presented briefly. Then, we develop a T-S fuzzy model and use the parallel distributed compensation control technique to design the controller. In addition, a fuzzy model-based observer is considered for estimating unmeasurable states. To guarantee the global asymptotic stability of the closed-loop system, we use a quadratic Lyapunov function and cast the fuzzy control and observer-based design problems in terms of linear matrix inequalities (LMIs). In the end, different optimization design case studies are studied to evaluate and compare the performance and robustness of the proposed controller with a baseline controller via numerical simulation.

Upper-Stage Anomalous Attitude Motion

During orbital maneuver, propellant slosh in partially-filled fuel tanks can cause tracking error or dynamic instability.

- DemoSat failed to reach targeted orbit (2007, Falcon 1, SpaceX).

Figure 1: *DemoSat(Credit: SpaceX)*

- NEAR experienced anomalous series of attitude motions and went into safety mode (1996, Delta II 7925-8, NASA).

Figure 2: *NEAR (Credit: NASA)*

- LEASAT experienced attitude control system instability during the preapogee injection phase (1984, Shuttle, HCI).

Figure 3: *LEASAT (Credit: NASA)*

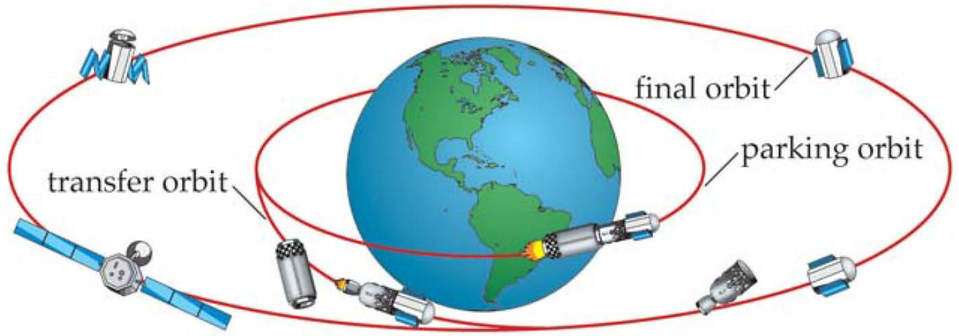

Figure 4: *Space Mission Orbits. (Credit: J.J. Sellers, "Understanding Space: An Introduction to Astronautics," Space Technology Series, 2004.)*

Model

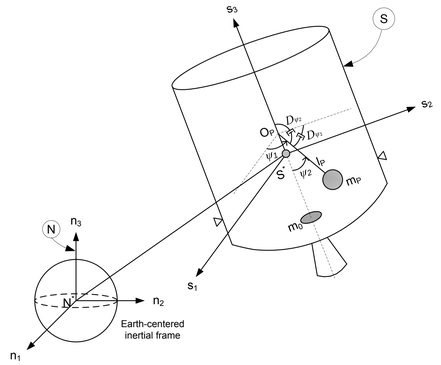

Figure 5: A spacecraft model with spherical pendulum.

Fuzzy Controller Design

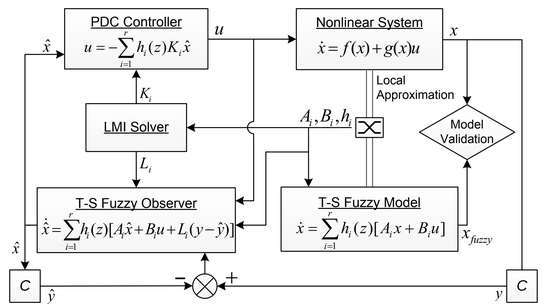

Figure 6: Schematic diagram of the T-S fuzzy observer-based feedback control.

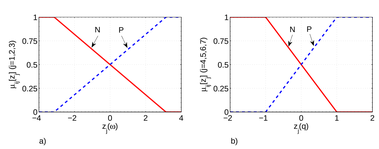

Figure 7: Fuzzy membership functions and universe of discourse for the premise variables.

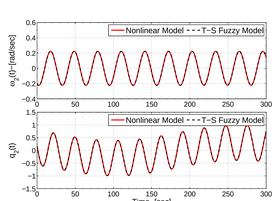

Figure 8: Time response of the selected states for the open-loop validation.

Closed-Loop Simulation

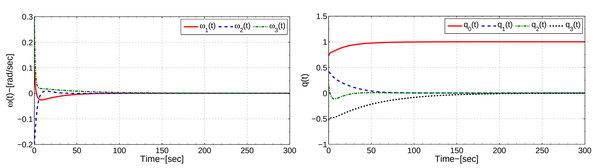

Figure 9: Time response of the spacecraft angular velocity components and quaternions.

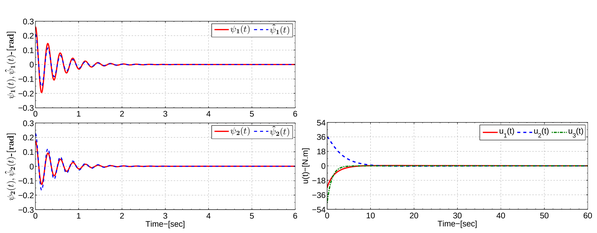

Figure 10: Left: Actual and estimated response of the pendulum angles. Right: Control inputs, $|u_i(t)| \leq 200\ N.m,\ (i = 1, 2, 3)$.

Controller Robustness

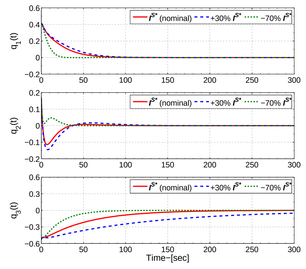

Figure 11: The effect of uncertainty in the mass-moment-of-inertia on the time responses of quaternions.

Conclusion

- Validated the developed T-S fuzzy model.
- Asymptotically stabilizes the attitude motion of spacecraft with fuel sloshing.
- Robust to parameter uncertainties in the model.
- Satisfies the control input actuator constraint.

Future Work

- Design robust and optimal fuzzy model-based attitude controller of spacecraft with fuel sloshing.
- Design a neuro-fuzzy attitude controller of spacecraft with fuel sloshing.

Publications

1. L. Mazmanyan and M.A. Ayoubi, "Attitude Motion of a Spinning Spacecraft with Fuel Sloshing in High-G Maneuvers," AAS 13-060, AAS/AIAA Astrodynamics Specialist Conference, Hilton Head, South Carolina, August 11-15, 2013.
2. L. Mazmanyan and M.A. Ayoubi, "Takagi-Sugeno Fuzzy Model-Based Attitude Control of Spacecraft with Partially-Filled Fuel Tanks," AIAA/AAS Astrodynamics Specialist Conference, San Diego, California, August 4-7, 2014.
3. L. Mazmanyan and M.A. Ayoubi, "Fuzzy Attitude Control of Spacecraft with Fuel Sloshing using Linear Matrix Inequalities," Acta Astronautica, (submitted).

Acknowledgements

This research is conducted during my 2015-16 award of Packard Research Fellowship in the School of Engineering and I am very grateful for the support.

An Approach to Image Compression using R-D Optimal OMP selection

Madhusudan Kalluri, Dr. Minqiang Jiang, Dr. Nam Ling
Santa Clara University Computer Science and Engineering

Introduction

- Traditionally, in image and video coding standards, transforms such as discrete cosine transform (DCT) and discrete Wavelet transform (DWT) are typically used to translate the image/image residual information into coefficients to facilitate compression.
- The original image/frame or the residual image, which is the difference between the original image and its predicted value is divided into smaller blocks or patches (for example 8x8 pixel patches). These patches are encoded using a transform.
- In the transform domain, the lower frequency components contain most of the energy/information while there is little information in the high frequency components.
- The coefficients are quantized to form a sparse set of non-zero coefficients.
- These transforms use a complete dictionary of basis elements to represent the data, i.e. number of elements in the dictionary is the same as the signal dimension.
- By using a redundant or over complete dictionary, the original information may be captured by a more sparse set of basis functions. Finding this sparse set is an NP-hard problem.
- Orthogonal Matching Pursuit is a greedy algorithm to solve this problem.
- Below is an example of an 8x8 pixel block/patch and its final DCT representation. Most of the coefficients are zeros, which helps in compression.

141	144	141	133	104	51	38	51
144	146	133	134	79	44	48	51
152	140	129	125	42	45	49	54
149	140	142	86	40	51	43	58
142	140	141	50	45	48	48	62
138	138	110	43	54	46	52	70
136	138	70	44	51	48	50	70
149	107	39	45	47	50	54	63

A

43	25	10	-2	0	0	0	0
6	5	-6	-3	0	0	0	0
0	-2	-1	1	1	0	0	0
1	0	0	0	0	0	0	0
0	0	0	0	0	0	0	0
0	0	0	0	0	0	0	0
0	0	0	0	0	0	0	0
0	0	0	0	0	0	0	0

Round(Quantised(DCT(A))

Traditional Discrete Cosine Transformation based scheme

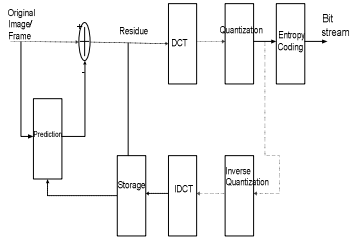

Sparse Representation

- Given a signal vector $y \in R^n$ we wish to represent it as sparse linear combination of a very few elements chosen from an over-complete dictionary $D \in R^{nxm}$, a collection of many signals bases where m is considerably larger than n.
- Given a sparsity level s, the goal of sparse representation is to find coefficients that minimize the reconstruction error under the sparsity constraint, written as

$$\min_x \|y-Dx\|_2 \text{ s. t. } \|x\|_0 \le s$$

where $x \in R^m$ is the vector which consists of the coefficients representing the signal y, and $\|.\|_2$ denotes the l_2 norm of a signal.

OMP Algorithm

- This is an iteration algorithm which tries to reduce a residual term, which is initially set to the original signal that is to be approximated. It has 3 key steps :

1) Project the signal to the selected basis
2) Greedy selection of that basis function that most closely matches the residual
3) Update of the coefficients

Orthogonal Matching Pursuit

- S is the sparsity constraint.
- The support set $x^{(k)}$ is the set of nonzero coefficients at the end of the k^{th} iteration.
- $I^{(k)}$ is the set of coefficient indices.

***Initialization*:**

- Normalize dictionary D.
- Initialize the support set $I^{(0)} = 0$, $x^{(0)} = 0$.

Computation:

for $k = 1, 2, \ldots, S$ *do*

Element selection: To determine an index j^* and add it to $I^{(k-1)}$

$r^{(k)} = y - Dx^{(k-1)}$ (compute the residual)

$j^* = \arg\min_{j=1,\ldots,n} \|r^{(k)} - d_j x\|_2$ (find the column that reduces residual most)

$I^{(k)} = I^{(k-1)} \cup \{j^*\}$ (add j^* to $I^{(k-1)}$)

Coefficient update: with support $I^{(k)}$, minimize the estimation residual,

$x^{(k)} = \arg\max_{x: x_{i=0, i \notin I^{(k)}}} \|y - Dx\|_2$

end for

At the end, there are S sets of non zero solutions available.

Rate Distortion Optimization (RDO) based OMP selection

How to select the optimum set of OMP coefficients for each block – some options

1. When the norm of the residual reaches a target error Ɛ.
   - Disadvantage: High number of coefficients may be selected for blocks with high norm value - may not be the optimal solution.
2. When the number of non zero coefficients reaches global sparsity constraint S.
   - The Peak Signal to Noise Ration (PSNR) of the reconstructed image increases rapidly with number of non zero coefficients k.
   - Bit rate R increases linearly with k.

Rather than using a fixed number of coefficients, we adopt a Rate-Distortion (R-D) optimal method to select the optimal solution amount S solutions

Define R-D cost J of a patch for each value of k (number of non zero coefficients :

$$J = D(k) + \lambda R(k)$$

- $D(k)$ is distortion measured as Mean Square Error (MSE) between original and reconstructed block
- $R(k)$ is the estimated number of bits associated with the k^{th} solution
- λ is the Lagrangian Multiplier: $\lambda = 0.85 * 2^{(qp-12)/3}$ where **qp** is Quantization parameter used in H264/HEVC video standards.
- $\mathbf{R(k) = R_H + R_C + R_I}$
  - $\mathbf{R_H}$ denotes the header bits telling the decoder how many dictionary elements are used for reconstruction
  - $\mathbf{R_C}$ denotes number of entropy coded bits of non zero coefficients
  - $\mathbf{R_I}$ denotes number of fixed length coded dictionary indices of non zero coefficients and is given by $k * \log_2$ [number of dictionary elements]

RDO based OMP selection contd.

Once D(k) and R(k) are available for all solutions, **R-D optimal *k*** can be determined by

$$k^* = \arg\min_{k \in \{1,2,\ldots,S\}} \{D(k) + R(k)\}$$

Experimental Results

- Patch size used is 8x8 pixels.
- Dictionary D is trained by employing K-SVD algorithm (which is a K means clustering method) with 93 training images. Dictionary size is 64x1024.
- Each image is preprocessed by down-scaling by a factor 2 and then scaling back to original size. This is subtracted from the original image to get the residual, which is devoid of low frequency components
- Global sparsity constraint S is set to 16
- 8 bit DCT is used and coefficients are later quantized using JPEG method.
- Sparse coefficients are also coded with 8 bits including sign and this is sufficient to cover their range.
- The coefficients and other information is entropy coded
- Sparse coefficient indices are fixed length coded with 10 bits.

Some sample statistics and results

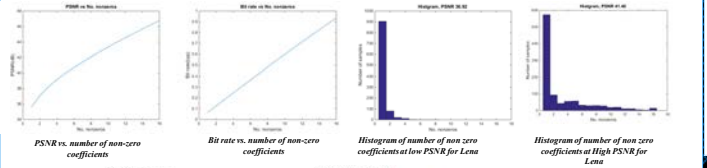

PSNR vs. number of non-zero coefficients — *Bit rate vs. number of non-zero coefficients* — *Histogram of number of non zero coefficients at low PSNR for Lena* — *Histogram of number of non zero coefficients at High PSNR for Lena*

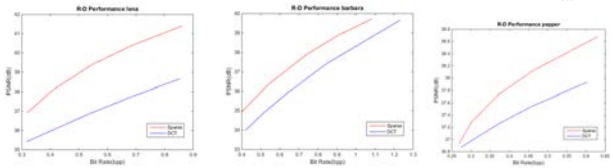

R-D curves for images Lena, Barbara, Pepper comparing R-D optimal sparse coding vs. DCT

R-D optimal sparse coding scheme

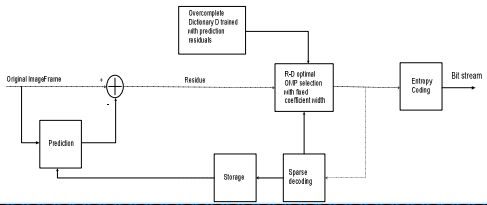

Conclusion

Proposed R-D optimal sparse coding method shows promise in achieving significant gains over traditional DCT based scheme.

Ongoing research includes adaptive sparse and DCT coding scheme, and quantization of sparse coefficients.

References

1) G. K. Wallace, "The JPEG still picture compression standard," Commun. ACM, vol. 34, no. 4, pp. 607–609, 1991.
2) D. Taubman and M. Marcellin, JPEG 2000: Image Compression Fundamentals, Standards and Practice, 1st ed. Norwell, MA, USA: Kluwer, 2001.
3) G. Davis, S. Mallat, and M. Avellaneda. "Adaptive greedy approximations," Journal of Constructive Approximations, vol.13, pp. 57-98,1997.
4) S. Mallat and Z. Zhang, "Matching pursuits with time-frequency dictionaries," IEEE Trans. Signal Process., vol. 41, pp. 3397–3415, Dec. 1993.
5) Y. C. Pati, R. Rezaiifar, and P. S. Krishnaprasad, "Orthogonal matching pursuit: Recursive function approximation with applications to wavelet decomposition," in Proc. Conf. Rec. 27th Asilomar Conf. Signals, Syst. Comput., vol. 1. Nov. 1993, pp. 40–44.
6) G. Rath, C.Guillemot, "Complimentary Matching pursuits Algorithms for sparse Approximation", Journal of Signal Processing, pp.702- 706, January 2009.
7) R. Neff and A. Zakhor, "Very low bit rate video coding based on matching pursuit," IEEE Trans. Circuits Syst. Video Technol., vol. 7, pp. 158–171, Jul. 1997.
8) R. M. F. i Ventura, P. Vandergheynst, and P. Frossard, "Low-rate and flexible image coding with redundant representations," IEEE Trans. Image Process., vol. 15, no. 3, pp. 726–739, Mar. 2006.
9) Horev, I., Bryt, O. and Rubinstein, R. "Adaptive Image Compression Using Sparse Dictionaries", Proc. IWSSIP 2012, Vienna, Austria, April 2012.
10) Je-Won Kang, Moncef Gabbouj, and C.-C. Jay Kuo, "Sparse/dct (s/dct) two-layered representation of prediction residuals for video coding," IEEE Trans. on Image Processing, vol. 22, no. 7, pp. 2711–2722, July 2013.
11) M. Aharon, M. Elad, and A. Bruckstein, "K-svd: An algorithm for designing overcomplete dictionaries for sparse representation," IEEE Transaction on Signal Processing, vol. 54, no. 11, pp. 4311–4322, Nov. 2006.
12) R. Rubinstein, M. Zibulevsky, and M. Elad, "Efficient implementation of the K-SVD algorithm using batch OMP," Dept. Technion Comput. Sci., Haifa State Univ., Haifa, Israel, Tech. Rep. CS-2008-08, Apr. 2008.
13) Je-Won Kang, C. C. Ja Kuo, Robert Choen and Anthony Vetro, "Efficient dictionary based video coding with reduced side information", ISCAS 2011.
14) M. Jiang, M. Kalluri, N. Ling, J. Zheng, P. Zhang "An approach to image compression using R-D optimal OMP selection", Proc. ISCAS 2016, Montreal, Canada, May 2015.

- Special thanks to **Michael Schimpf and Promila Agarwal** for their help with the template for this poster and the DCT matrix example in the first slide.

FEA Analysis of Al-Cu Intermetallic Compounds Growth Mechanism During Thermosonic Ball Bonding Process in Micro-Electronic Packaging

Maryam Gholamirad, Panthea Sepehrband

Department of Mechanical Engineering, Santa Clara University

INTRODUCTION

Thermosonic ball bonding process of copper wire to aluminum pad, is a process to join these two alloys together in micro-electronic packaging industry.

Understanding formation of IMCs (InterMetallic Compounds) is very essential to enhance reliability of interconnections in micro-electronic components.

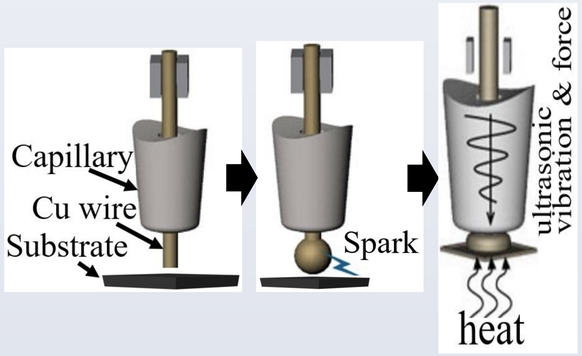

Ball bonding stages

OBJECTIVES

1. A multi-physics Finite Element Analysis (FEA) model will be carried out in ANSYS to define stress distribution on Cu-Al contact surface (where IMCs form)

2. Using the analytical model, thickness of the IMCs will be calculated based on the stress distribution input from ANSYS, material constants from molecular dynamics simulations and other constants from literature

3. To validate the assumptions and predictions, thickness of IMCs obtained from the theoretical analysis is compared to the thickness of IMCs measured experimentally from SEM (Scanning Electron Microscope) images

MATERIALS & METHODS

A multi-physics (thermal, structural & vibration) stress analysis was conducted in ANSYS LS-DYNA.

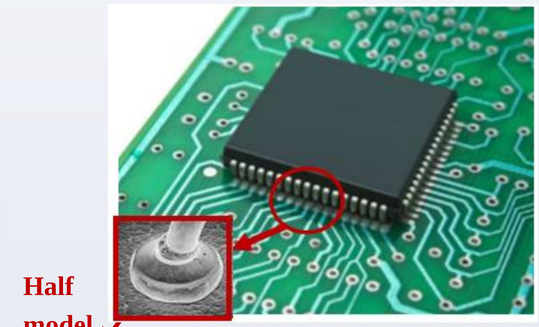

Half model

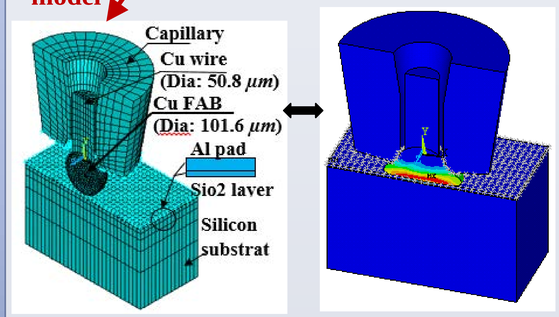

The material behavior for copper FAB (Free Air Ball) and aluminum pad is considered to be non-linear, with Chaboche Kinematic Hardening behavior. The rest (capillary, copper wire, SiO2 layer and Silicon substrate) were considered to be in linear elastic region [1].

Loading stages (impact & ultrasonic vibration):

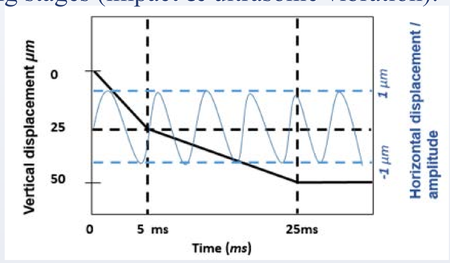

Calculating thickness of IMCs using **analytical** model [2]:

$$x = \sqrt{D_{eff}\,t}$$

x: IMC thickness
D_{eff}: effective diffusion
t: time

Equation 1

$$D_{eff} = D_v\left(1 + \frac{\rho a_c D_c}{D_v}\right)$$

Equation 2

Molecular dynamics simulation:

Dv: lattice diffusion
D_c: dislocation core diffusion
a_c: cross-sectional area of dislocation core
ρ: dislocation density
$\rho = \left(\frac{\sigma_{dis}}{\alpha M G b}\right)^2$

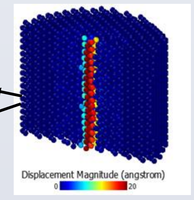

Equation 3

FEA analysis

σ_{dis}: flow-stress
α, M, G, b: Materials constants

Results

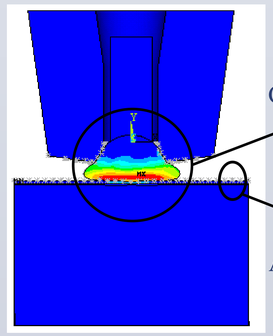

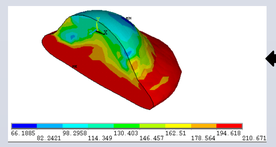

Von mises stress distribution on Cu FAB (Mpa)

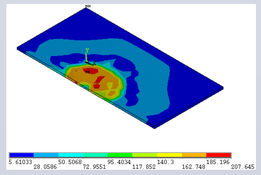

Von mises stress distribution on Al pad (Mpa)

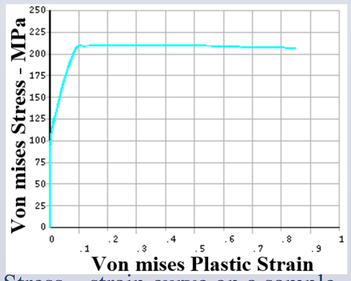

Stress – strain curve on a sample node in plastic region on Cu FAB

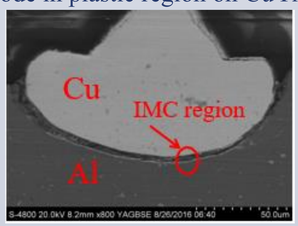

Experimentally defining size of IMCs using SEM

Time (t)=9 *ms*: IMC thickness experimentally measured from SEM: x = 30 *nm*

Time (t)=9 *ms*: IMC thickness calculated in analytical method: x = 34 *nm*

CONCLUSIONS

IMCs (InterMetallic Compounds) thickness was calculated using the analytical model. IMC thickness was also measured experimentally using SEM:

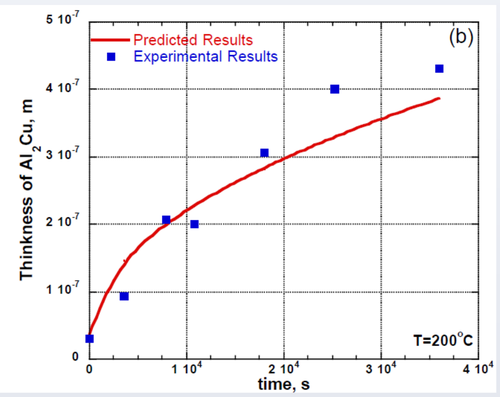

It is concluded that IMCs growth is related to accelerated diffusional processes in atomic structure of metals. Diffusion, itself, is highly influenced by dislocation density. Dislocations are mainly generated and affected by plastic deformation.

FUTURE WORK

Wear mechanism of wedge bonding tool in wedge bonding process will be simulated. A FEA simulation will be carried out which will also include friction.

REFERENCES

[1]- HC Hsu, LM Chu, WY Chang, YF Chen, JH Chien, SL Fu, SP Ju, WJ Feng, "Further characterization of Pd-coated copper wire on wirebonding process: from a nanoscale perspective", Journal of Material Science: Mater Electron 24: 3594–3602, 2013

[2] E.W. Hart, R.E. Hoffman, & D. Tumbull, "Self-diffusion in dilute binary solid solutions," Acta Metallurgica, 5(2), pp. 74-76, 1957

Acknowledgement

This research is supported by the internal grant from the School of Engineering at Santa Clara University.

CONTACTS

M. Gholamirad: mgholami@ucalgary.ca
P. Sepehrband: psepehrband@scu.edu

www.PosterPresentations.com

Breakabot Precomputed Model for Anomaly Management

Matthew Condino; Dr. Christopher Kitts; Mike Rasay
Robotics Systems Laboratory || Department of Mechanical Engineering
Santa Clara University
School of Engineering

Abstract

Model Based Reasoning (MBR) is a systematic reasoning approach that uses first principles design information to manage anomalies in a complex engineering system. Its computational complexity, however, prevents realtime or near-realtime use. In this study, we use MBR to precompute anomaly scenarios prior to the operation of a system using an enhanced model that specifies the likelihood of specific anomalies; during operation the resulting database can be quickly searched to perform anomaly detection and diagnosis. This modelling framework was implemented on Breakabot, a 3 wheeled mobile robot. Initial testing is verifying the technique and highlighting its value.

Reasoning Architecture

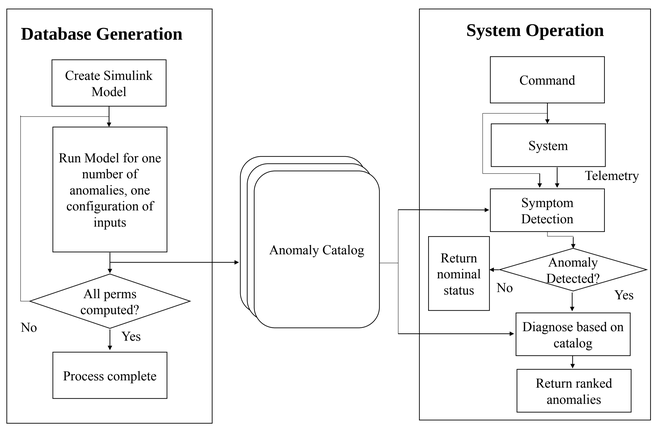

References

- Kitts, Christopher. "Managing space system anomalies using first principles reasoning." IEEE robotics & automation magazine 13.4 (2006): 39-50.
- Rasay, R., *A Graphical Model-Based Reasoning Analysis Environment for Space System Anomaly Management*, Advisor: C. Kitts, SCU Master's Thesis, June 2007.
- Hedlund, Jake, *Implementing Confidences in a Model-based Reasoning System to Build a Prioritized Catalog of Potential Anomalies*, Advisor: C. Kitts, SCU Master's Thesis, draft.

Research Innovation

Current MBR Anomaly Management Approach	Proposed Precomputed Reasoning Anomaly Management Approach
• Model Based Reasoning (MBR) uses deliberative reasoning to detect, diagnose, and resolve operational anomalies in an engineering system. • Approach is faster and more precise than human based analysis. • Computational complexity precludes use in realtime or near-realtime control.	• Pre-compute anomaly scenarios using MBR, sort them in a database, and use a realtime production rule system to select viable scenarios based on configuration and telemetry. • Dramatically reduces computation during realtime operations at the cost of creating a large database prior to operation.

The System: Breakabot

Design Features

- Omnidirectional wheels provide holonomic motion
- Remote piloting via an on board camera and a joystick
- Automated telemetry collection
- Redundant components
- Experimental breakpoints

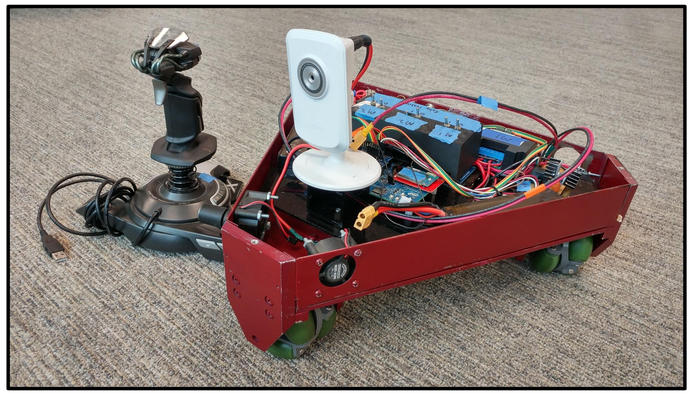

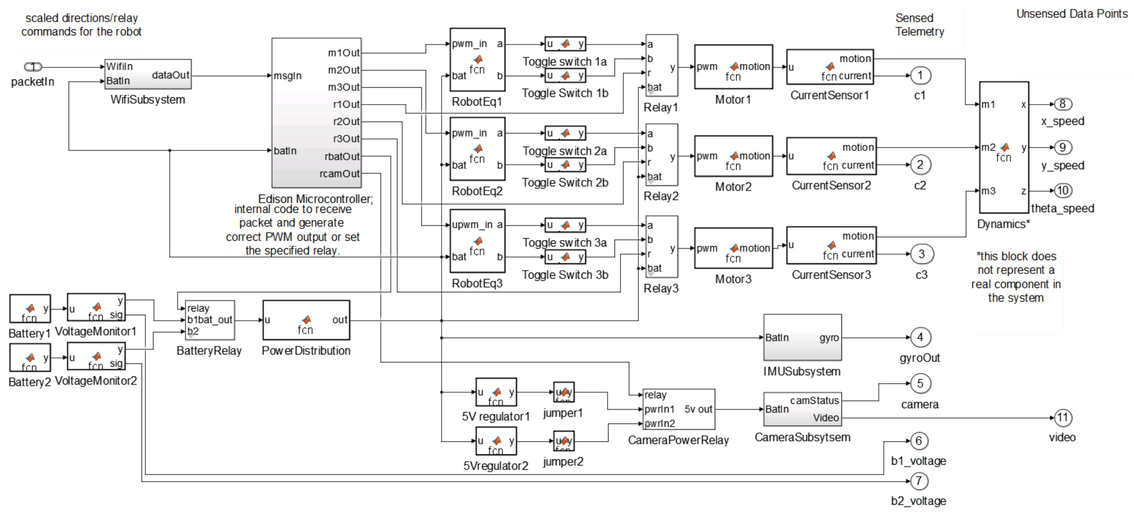

Benefits and Value

Performance Improvement

- Systematic generation of an anomaly catalog
- Likelihood rankings prioritize diagnoses
- Precomputation accelerates detection & diagnosis

Value for Applications

- Lowers personnel costs due to reduced anomaly team manpower
- Improves service level and reduces losses associated with system downtime; this can be millions of dollars for spacecraft missions

Analytics

Statistic	Value
Number of Components in System	28
Number of Connections in System	65
Number of Checked Telemetry Outputs	7
Number of configuration/command permutations	2,496
Number of lines currently in the database	33,424,752
Number of permutations for 1 anomaly with a single configuration	56
Number of permutations for 2 anomalies with a single configuration	1,540
Number of permutations for 3 anomalies with a single configuration	27,720

Status of Work

- Robot model has been verified for several test cases.
- Initial MySQL database has been automatically generated for all single and double anomaly cases.
- Precomputed MBR Anomaly Management appears to be a viable, precise, and fast method for detecting and diagnosing anomalies.

Future Work

- Full validation of simulated telemetry outputs on all input cases.
- Run formal blind experiments to fully validate the modelling technique.
- Further refinement of detection algorithm using traditional MBR techniques.

Hybrid Force/Position Control Architecture for Mobile Robot Formations

Michael Neumann; Advisor: Dr. Christopher Kitts
Department of Mechanical Engineering
Santa Clara University
School of Engineering

Abstract

Multirobot collaboration has the potential to provide a range of benefits from redundancy to improved data products and capabilities. We propose a hybrid force/position control architecture to allow multirobot formations to control position in some degrees of freedom while applying desired forces and torques to other degrees of freedom. The hybrid control architecture is validated through both simulations and experiments with a hardware testbed.

Background

The Robotic Systems Laboratory has developed the cluster control architecture, which simplifies the specification and control of multirobot formations. To date the cluster space architecture controls the size, shape, position, and velocity of mobile robot formations and has been used in applications ranging from dynamic guarding of marine assets to gradient based navigation. This work extends the cluster space control architecture to allow the mobile robot formations to apply desired forces and torques on an object.

Control Architecture

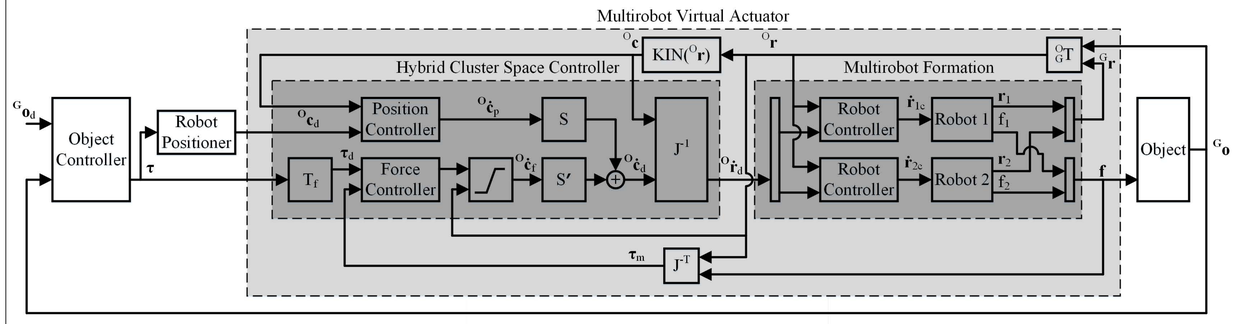

Results

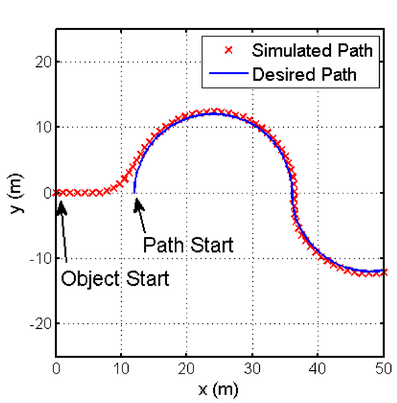

Matlab/Simulink Simulation Results

Experimental Testbed

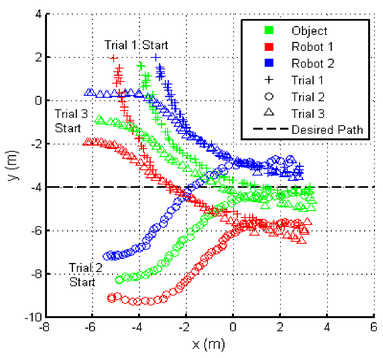

Experimental Results
Line Following

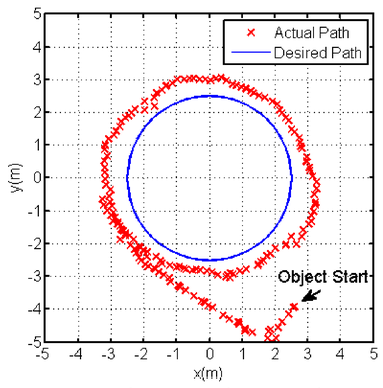

Experimental Results
Circle Following

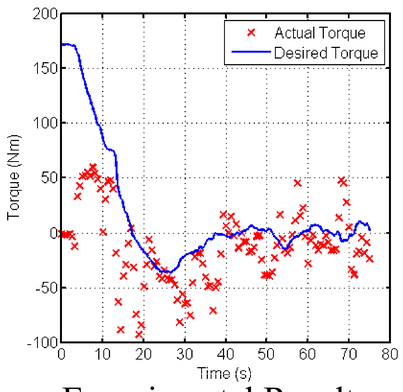

Experimental Results
Torque Control

Conclusion

A hybrid force/position control architecture was developed and shown to work in a Matlab/Simulink simulation environment and with a hardware testbed. This architecture holds promise for diverse tasks such as space construction and undersea infrastructure maintenance.

Future Work

Future improvements include:

- Creating a more dynamic testbed for experimentation
- Transporting and manipulating a flexible object
- Developing a state machine to seamlessly switch between pure position control (for approaching the object) and hybrid control (for pushing the object)

Acknowledgements

Thanks to Matt Chin, Jackson Arcade, Thomas Adamek, and Robert McDonald for their help with the testbed and also the School of Engineering, the Robotic Systems Laboratory, and NSF for providing funding.

Molecular dynamics study of effect of crystallographic orientation on critical distance for Jump to Contact

M. Khajehvand, P. Sepehrband
Dept. of Mechanical Engineering, Santa Clara University, CA, USA

Abstract

The purpose of this ongoing study is to determine the effect of crystallographic orientation on the critical distance between two metal substrates below which Jump to Contact occurs and also, the relaxation time which is needed afterwards in order to create a perfect contact.

Background

- Wire boding: an interconnection technique used in IC packaging, wherein a wire (Au, Al or Cu) and a bond pad (Al) are bonded using a combination of temperature, force and ultrasonic power.
- Jump to Contact (Avalanche in Adhesion): As two substrates approach each other, the short range attractive interactions between the atoms on the opposing substrate surfaces elastically stretches the two materials.

Experimentally proved:

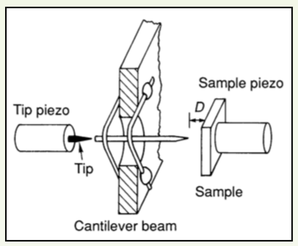

Atomic Force Microscopy (schematic) [1]

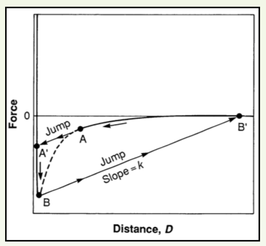

"Force - Displacement" curve (schematic) [1]

Computationally proved:

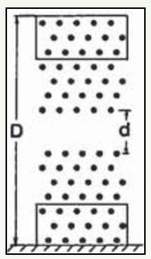

Initial configuration of two substrates (schematic) [2]

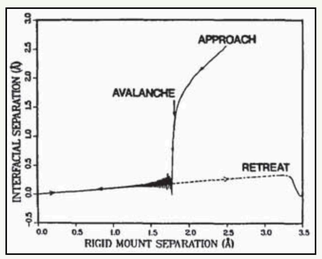

"d - D" curve during simulation of contact and separation [2]

Objectives

- Effect of existence of nano-asperities on bond strength
- Effect of crystallographic orientation on:
  - critical distance below which Jump to Contact occurs
  - relaxation time which is needed for achieving a perfect bonding, for the cases with distances below the critical distance

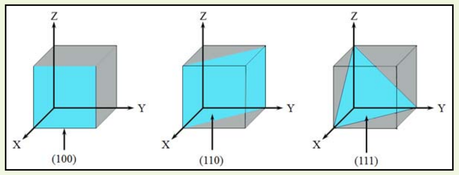

Different crystallographic planes

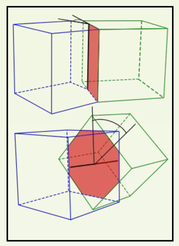

Same crystallographic plans with mis-orientation

Methods

- Molecular Dynamics simulation
  - widely used in atomic simulations at the nanoscale
- MD Simulator: LAMMPS
- Visualization tool: OVITO
- Simulation cell:
  - periodic in x and y-directions
  - non-periodic in z-direction

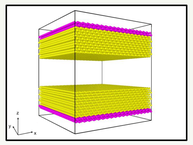

- Simulation details: T = 300K , Pxx = Pyy = 0 bars
- Materials: Au, Al and Cu

Preliminary Results

Contact, compression and separation simulations are performed for the setup that contains two substrates where an asperity is placed on top of the lower one. The upper slab is displaced towards the other one with a constant velocity and at a pre-given distance the sign of velocity is reversed until complete separation happens. The sum of z-component of force on upper substrate atoms is calculated throughout the simulation.

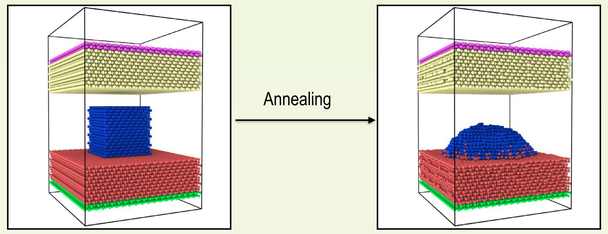

Initial configuration — Relaxed-shape of asperity

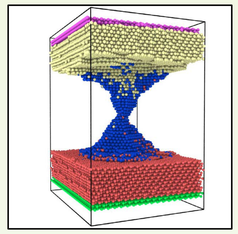

Final configuration

"Force-displacement" curve shows the occurrence of Jump to contact and also the bond force (maximum tensile force that is needed for complete separation.

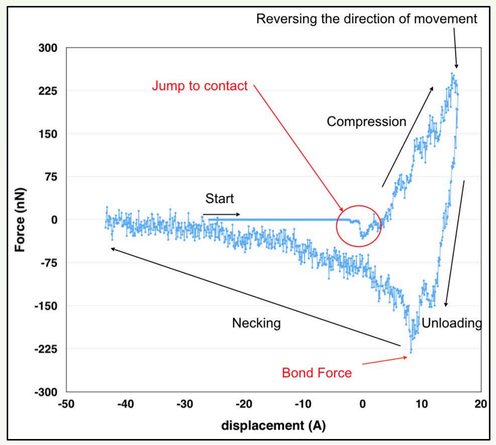

"Force - Displacement" curve

Future Work

Currently, we are performing simulations with different initial surface distances between two flat slabs. We believe that we will get a plot similar to the plot below which shows us what is the critical distance for Jump to Contact. Additionally, the necessary simulation time for reaching to a value very close to zero will tell us how much relaxation time is needed for achieving a perfect contact. This model will enable us to investigate on the effect of crystallographic orientation.

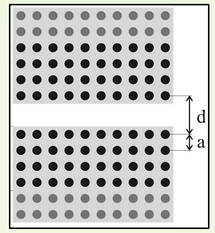

Initial configuration of two flat substrates (schematic) [3]

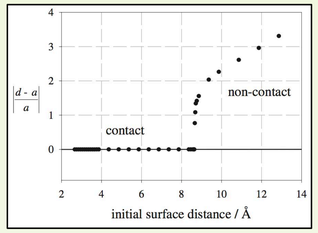

"Deviation of final surface distance from layer distance - Initial surface distance" curve [3]

Summary

Prior to this time, we saw that Jump To Contact occurs and we were able to measure the bond force. We also have a model that can help us to study the effect of crystallographic orientation on the critical distance for happening of Jump to Contact and the relaxation time that is necessary for having a perfect contact. We believe that the result of this study can shed light on some issues in the area of IC packaging techniques.

Acknowledgement

This study is supported by Santa Clara University, School of Engineering.

References

1. U. Landman, W. D. Luedtke, N. A. Burnham and R. J. Colton, Atomistic Mechanisms and Dynamics of Adhesion, Nanoindentation, and Fracture, Science, New Series, Vol. 248, No. 4954 (Apr. 27, 1990), pp. 454-461
2. P. A. Taylor, Atomic-Scale Simulation of Adhesion Between Metallic Surfaces, MRS Online Proceedings Library Archive, Volume 209 January 1990, 225
3. O. Miesbauer, M. Götzinger and W. Peukert, Molecular dynamics simulations of the contact between two NaCl nano-crystals: adhesion, jump to contact and indentation, Nanotechnology 14 (2003) 371–376

Engineering exosomes towards therapeutics

Natalie Duong | Dr. Biao Lu | Santa Clara University | Department of Bioengineering

Introduction: Therapeutic Potential of Exosomes

Exosomes are extracellular nanovesicles that are naturally secreted by most of the cells in our body for transporting and communicating between tissue and organs. Their unique features and therapeutic potential are summarized in the table below.

Table 1: Therapeutic potential of exosomes.

Traits	Potential Therapeutic Benefit
Small size (~30-100 nm)	Easy transportation throughout the body
Lipid bilayer	Protection of biological cargo
Naturally secreted	No immune response
Ability to cross the blood brain barrier	CNS drug delivery

Approach: Surface Engineering

To harness the therapeutic potential of exosomes, we engineer the surface of the exosomes using a tetraspanin CD63 scaffold or a vesicular stomatitis virus G glycoprotein scaffold.

Tetraspanin CD63

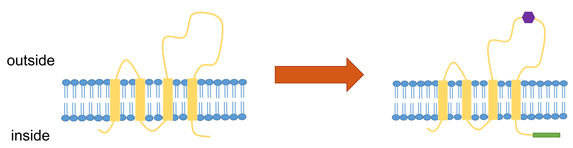

Figure1: Tetraspanin CD63 scaffold unmodified (left) and modified (right).

Benefits of using tetraspanin CD63:

- Natural molecule on exosome surface
- "M" morphology allows variety of options
  - Multiple intracellular and extracellular domains

Santa Clara University
School of Engineering

Vesicular Stomatitis Virus G Glycoprotein (VSVG)

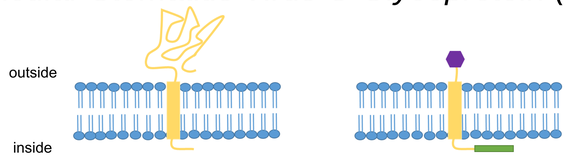

Figure 2: VSVG scaffold unmodified (left) and modified (right).

Benefits of using VSVG:

- Enhanced production and uptake of exosomes
- Simple structure and membrane configuration

Methods

Create Design
- Plasmid design
- 3rd party production of plasmid

Produce the Design
- Transfection of plasmid into mammalian cells
  - Use lipofectamine transfection reagent

Evaluation of Production
- Fluorescent live cell monitoring
  - Searching for localization into exosomes

Results

Table 2: Exosome localization of CD63-GFP and VSVG-RFP in mammalian cells.

	Tetraspanin CD63-GFP	VSVG-RFP	Cytosolic GFP
Phase	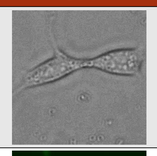	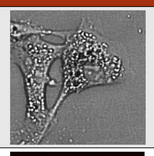	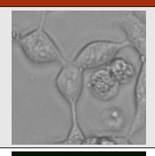
Fluorescent	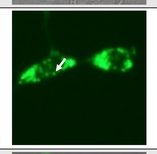	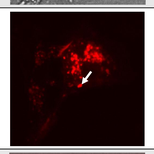	
Overlay	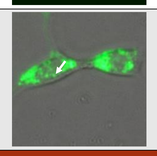	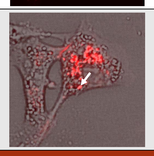	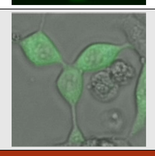
	HEK 293	Hep G2	HEK 293

Discussion

Our research has confirmed that tetraspanin CD63 and VSVG are potential scaffolds for the surface engineering of exosomes, displayed by the successful localization of the modified protein into exosomes. Further modifications of these scaffolds could have many applications including therapy, delivery of biologically active cargo, and specifically targeted therapy (Table 2).

Table 3: Potential applications of engineered exosomes.

Application	Proposed Modification
Visualizing exosome biogenesis	Fusion with red/green fluorescent protein (RFP/GFP)
Drug delivery	Loading of drug inside of exosome
Targeted Therapy	Cell-specific targeting molecule on outside surface of exosome

This research can be further advanced through creating designs for multiple purposes such as a TNF-receptor treatment for rheumatoid arthritis and targeted drug delivery for cancers. Our researches focus on exosome-based therapeutics, and our immediate goal is to build up a general strategy for exosome surface engineering using mammalian cells.

References

Gao, J., Chu, D., & Wang, Z. (2016). Cell membrane-formed nanovesicles for disease-targeted delivery. Journal of Controlled Release : Official Journal of the Controlled Release Society, 224, 208–216. http://doi.org/10.1016/j.jconrel.2016.01.024

Hassuna, N., Monk, P. N., Moseley, G. W., & Partridge, L. J. (2009). Strategies for targeting tetraspanin proteins: Potential therapeutic applications in microbial infections. BioDrugs, 23(6), 341–359. http://doi.org/10.2165/11315650-000000000-00000

Stickney, Z., Losacco, J., McDevitt, S., Zhang, Z., & Lu, B. (2016). Development of Exosome Surface Display Technology in Living Human Cells. Biochemical and Biophysical Research Communications, 472(1), 53–59. http://doi.org/10.1016/j.bbrc.2016.02.058

Théry, C., Zitvogel, L., & Amigorena, S. (2002). Exosomes: composition, biogenesis and function. *Nature Reviews. Immunology*, *2*(8), 569–579. http://doi.org/10.1038/nri855

Compact Microstrip Yagi-Uda Antenna Arrays for Microwave Hyperthermia at 5.8 GHz

Nivedita Parthasarathy, PhD Student; Dr. Ramesh Abhari, Advisor
Department of Electrical Engineering
Santa Clara University
School of Engineering

Fullwave Electromagnetic Simulation in CST

Motivation:

- Designing a compact antenna array to create a focused beam into a bioelectromagnetic CAD human model for Microwave Hyperthermia
- Hyperthermia is a medical procedure that involves elevating the temperature of tumor cells by means of a microwave applicator. Controlled exposure to microwave radiation destroys cancer cells which makes hyperthermia an effective form of non-invasive radiation therapy.
- Studies of Specific Absorption Rate (SAR) patterns in human tissues have shown optimum radiation absorption at the skin/fat interface occurs at 5.8 GHz.

Objectives:

1. Design a 2-element collinear PCB Yagi antenna array to use as an on-body applicator for delivering microwave radiation. The Yagi-Uda antenna array was chosen for its high gain and unidirectional beam pattern.
2. Adapt design for double-sided 4-element array with parasitic dipole elements to enhance isolation while maintaining compact structure.
3. Study power loss density and SAR in human body by using a heterogeneous biomodel in CST.

Design of free-standing antenna arrays:

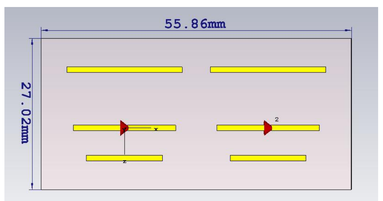

S-Parameter results of standalone antenna arrays

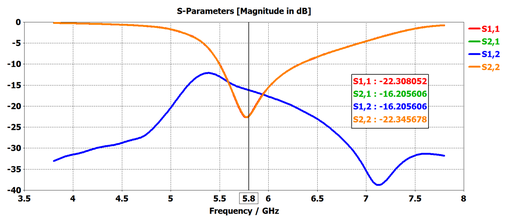

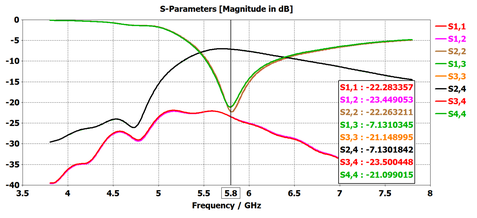

Placement of hyperthermia applicator in stomach region

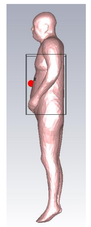

Radiation Pattern of Collinear and Non-planar Yagi antennas

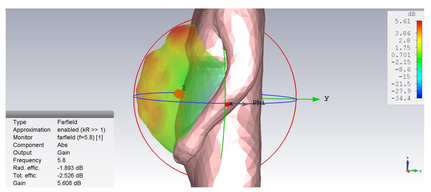

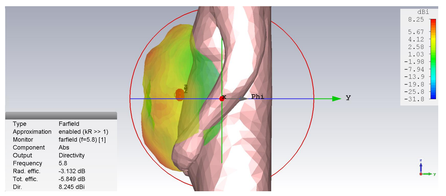

Power loss density and SAR

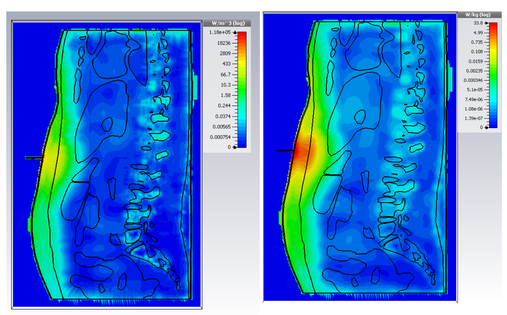

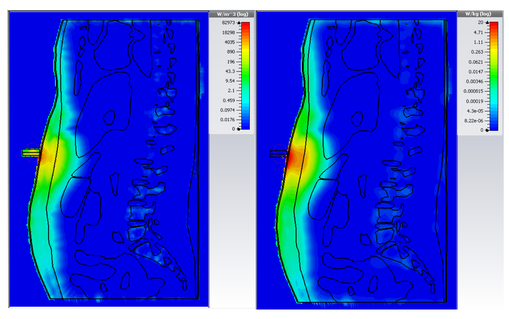

Key findings of this project:

- Parasitic structures can be used as a simple and effective method to reduce mutual coupling in closely-spaced antennas.
- Observe power absorbed, mainly at skin-fat interface and record values at varying tissue depths.
- Record average and point SAR.

Preliminary Experiments:

- Development of a homogeneous gel-based body phantom to mimic human tissues at 5.8 GHz frequency.

Sample of body phantom

- Dielectric characterization of phantom material via capacitance measurements.
- Transmission line termination technique to determine complex reflection coefficient to characteristic dielectric material.

Next steps:

- Improve design of RF applicator by use of housing structures and shielding to provide highly focused heating of biological tissues at required depth.
- Fabrication of body phantom to accurately model microwave energy transfer from antenna array.
- Setup and measurement of transmit-receive module for hyperthermia.

SIGNATURE BASED FAST MOTION ESTIMATION FOR HD VIDEO

Pavel Arnaudov, Dr. Tokunbo Ogunfunmi

Department of Electrical Engineering,
Santa Clara University, Santa Clara, California 95053, USA
pdarnaudov@scu.edu, togunfunmi@scu.edu

2017 SCU School of Engineering Research Showcase
Signal Processing Research Lab (SPRL)

Abstract

- Motion estimation consumes the major part of time and power in both video compression standards – HEVC and H.264. This poster presents a Fast Motion Estimation algorithm, which targets Full Search quality even at HD resolution. It is an enhancement of existing Fast Motion Estimation algorithms with the main purpose of reducing cost and power consumption for devices performing Motion Estimation while collecting and transmitting video data (used for deep learning). The proposed algorithm is based on dimensionality reduction and uses Content Addressable Memories (CAMs) and locality sensitive signatures to achieve "Quantitative Expression of Similarity". The algorithm also presents an enhancement to one of the most efficient existing Fast Motion Estimation algorithms – HMDS. The quality achieved with the new algorithm is only 3dB below Full Search.

Summary

The proposed algorithm has two components - one is location-blind (the signature CAM based part, which achieves the last 1dB improvement, which is the hardest to achieve) and the other locality-aware (the Enhanced HMDS part, which covers half of the quality gap to Full Search) to complement each other in cases of either more dynamic or less dynamic videos. The power savings will result in prolonged battery life for hand held devices. The proposed algorithm is scalable and will have the same complexity for higher than UHD resolutions. This makes it suitable for low power devices. It can be also used in self-driving cars or as a Motion Estimation Co-Processor

Motion Estimation

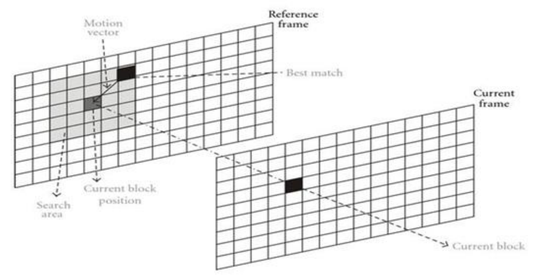

$$SAD = \sum_{i=0}^{15}\sum_{j=0}^{15}|x_{ij} - y_{ij}| \qquad PSNR = 10 \cdot \log_{10}\frac{255^2}{\frac{1}{\#pixels}\sum_{i,j}(x_{i,j} - y_{i,j})^2}$$

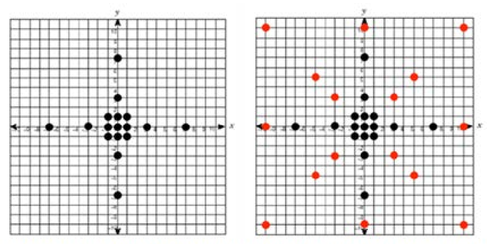

HMDS Step 1 Search Pattern – Original (a) and Enhanced (b)

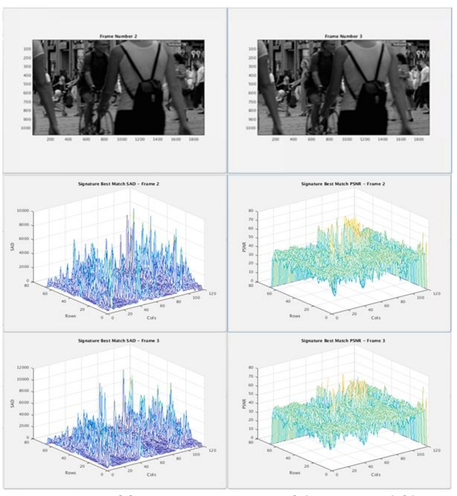

Comparison of frequency responses of the proposed filters.

Architecture for Fractional-Pel Motion Estimation

❖ Our proposed algorithm first adds an enhancement to HMDS (similar to the enhancement HMDS adds to DS), which closes about half the gap between HMDS and Full Search in HD (~29dB and ~37dB respectively). The remaining quality gap needs locality unaware search which we propose to be assisted by an array of CAMs performing searches across locality based signatures followed by majority vote to find the best match. The similarity between MBs is derived through their signature equality. The signature of a MB is a number (a point in one dimensional space), that represents the MB (MB being a point in 256 dimensional space for 16x16 MBs). Proximity in this one dimensional space however (proximity of signatures), does not guarantee in any way proximity in the 256 dimensional space (quantified as low SAD). If two MBs are the same, their signatures are the same, but if the MBs are very similar, their signatures are not guaranteed to be the same.

Signature Based Algorithm

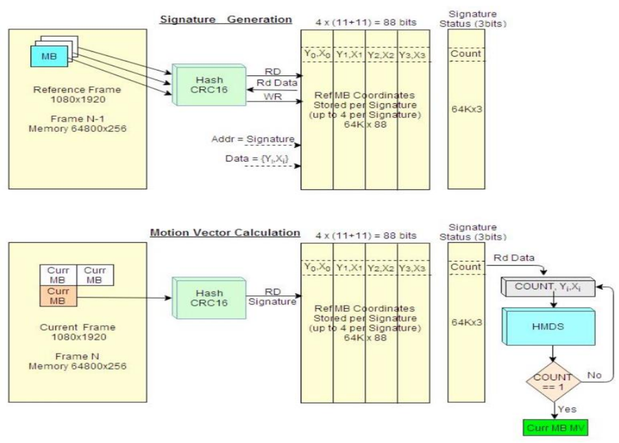

Resource	Area [um^2]	Power [uW]
Logic (~100,000 gates; ~4 gates/um^2)	24773 (2%)	19293 (99%)
Signatures Memory (64K x 88)	956355	181
Status Memory (64k x 3)	70813	23
Total	1051941	19497

Sequence	PSNR [dB]
Full Search	36-37
HMDS	30
Proposed Algorithm	32-33

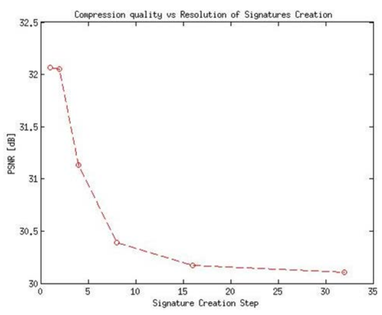

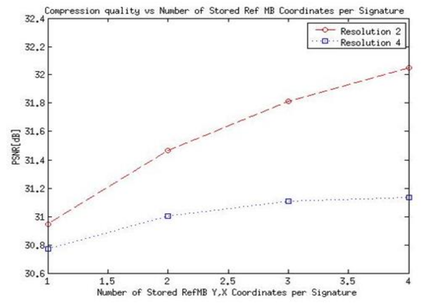

Step of Sig. Creation	1	2	4	8	16	32
PSNR [dB]	32.06	32.05	31.13	30.39	30.17	30.10

Num Coord Pairs [Y,X]	1	2	3	4
PSNR [dB] (Resolution 2)	30.95	31.46	31.82	32.05
PSNR [dB] (Resolution 4)	30.77	31.00	31.11	31.13

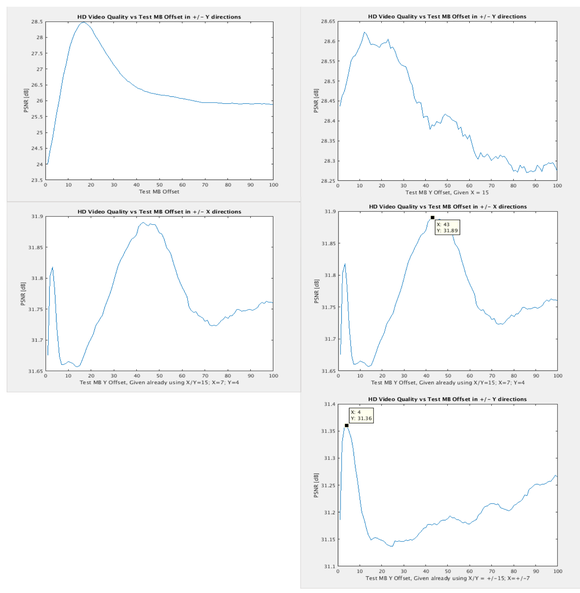

Signature

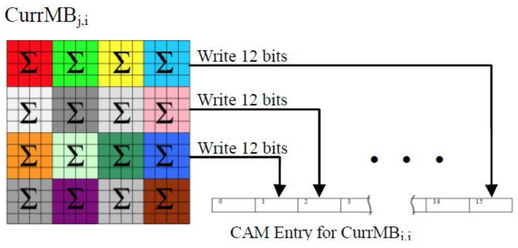

Curr MB Signature Generation: 16 patches x 12 bit sums = 192bits

MB Sig[15:0]=CRC16({P_{15}[11:0]&Mask[11:0], P_{14}[11:0]&Mask[11:0], … , P_0[11:0]&Mask[11:0]})

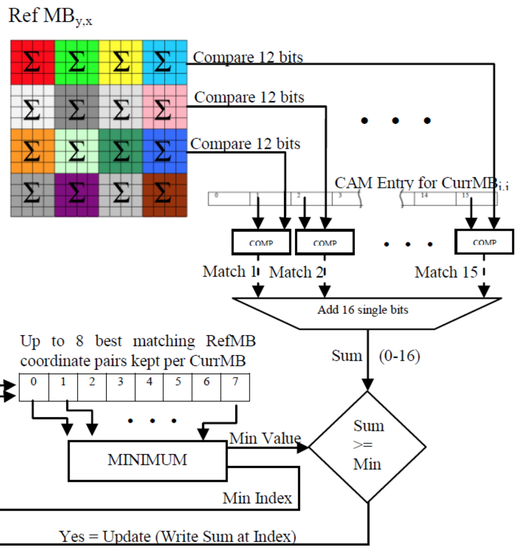

Signature CAM comparison: RefMB vs CurrMB

Algorithms' Quality

Sequence	PSNR [dB]
Full Search	36-37
HMDS	29-30
Enhanced HMDS (RS)	33-34
Proposed Algorithm	34-35

Resolution for RefMB Signature

Step of Sig. Creation	1	2	4	8	4*	8*
Frame (i) PSNR [dB]	33.28	33.32	33.24	33.16	33.83	33.89
Frame (i+1) PSNR [dB]	33.33	33.41	33.35	33.44	34.10	34.03
Average PSNR [dB]	33.31	33.36	33.30	33.30	33.97	33.96

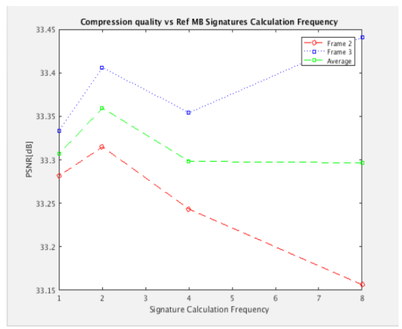

RefMB signature resolution impact on ME quality

Motion Vectors

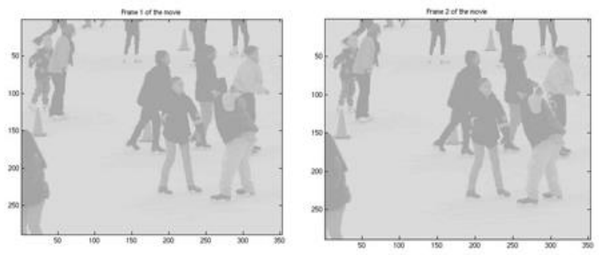

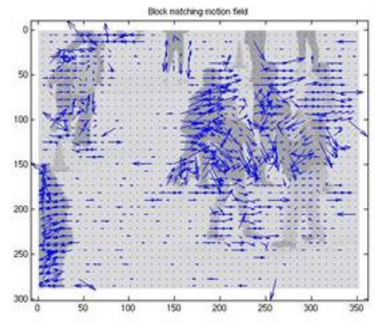

Per CurrMB CAM

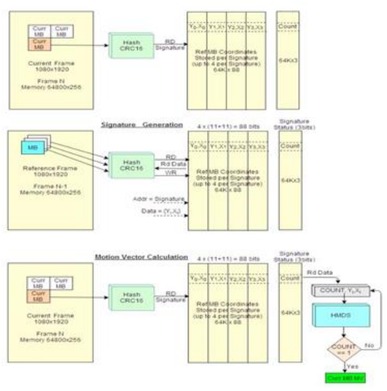

Towards Efficient Resource Provisioning in MapReduce

Peter P. Nghiem and Silvia M. Figueira, Department of Computer Engineering
{pnghiem, sfigueira}@scu.edu

Santa Clara University
School of Engineering

Abstract

In the era of Big Data, energy efficiency has become an important issue for the ubiquitous Hadoop MapReduce framework. However, the question of what is the optimal number of tasks required for a job to get the most efficient performance from MapReduce still has no definite answer. Our method and algorithm for optimal resource provisioning allow users to identify the Best Trade-off Point on an elbow curve of performance vs. resources to build a database of resource consumption signatures for subsequent behavioral replication. The results verify that the currently well-known rules of thumb for calculating the required number of reduce tasks are inaccurate and could lead to significant waste of computing resources and energy.

Best Trade-off Point Method

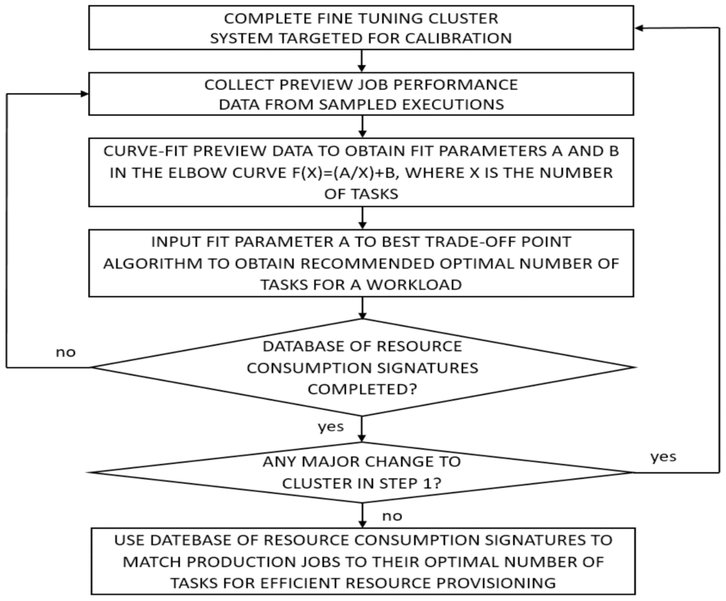

Design of BToP Algorithm

1. Compute the number of tasks over a range of slopes from the 1st derivative of *f(x)=(a/x)+b* and the acceleration over a range of slopes from the 2nd derivative.

2. Apply the Chain Rule to look for break points and major plateaus on the graphs of acceleration, slope, and task resources over a range of incremental changes in acceleration/slope increment.

$$f(x) = \left(\frac{a}{x}\right) + b$$

$$f'(x) = \lim_{\Delta x \to 0} (f(x + \Delta x) - f(x))/\Delta x$$

$$f'(x) = -ax^{-2}$$

$$x = \sqrt{-a/f'(x)}$$

$$f''(x) = f'(f'(x))$$

$$= \lim_{\Delta x \to 0} \frac{(f(x + \Delta x) - 2f(x) + f(x - \Delta x))}{\Delta x^2}$$

$$f''(x) = 2ax^{-3}$$

$$\frac{d(acceleration)}{d(tasks)} = \frac{d(acceleration)}{d(slope)} \cdot \frac{d(slope)}{d(tasks)}$$

Results

```
# Table of number of tasks over range of slopes from -0.25 to -39.25 for x=sqrt(-a/slope)
# Slope     Terasort 10GB   Terasort 100GB   Terasort 1TB
 -0.25          8.82            31.55           111.33
 -1.25          3.94            14.11            49.79
 -2.25          2.94            10.52            37.11
 -3.25          2.45             8.75            30.88
 -4.25          2.14             7.65            27.00
 -5.25          1.92             6.89            24.29
 -6.25          1.76             6.31            22.27
 …
#Table of acceleration over range of slopes from -0.25 to -39.25 for accele=2a(1/pow(slope,3)
# Slope     Terasort 10GB    Terasort 100GB    Terasort 1TB
 -0.25          2487.78         31862.78         396631.04
 -1.25            19.90           254.90           3173.05
 -2.25             3.41            43.71            544.08
 -3.25             1.13            14.50            180.53
 -4.25             0.51             6.49             80.73
 -5.25             0.27             3.44             42.83
 -6.25             0.16             2.04             25.38
 …
# Table of recommended acceleration, slope and optimal number of tasks over range of
incremental changes in acceleration per slope increment from 1 to 70
#Accele     Terasort 10GB           Terasort 100GB           Terasort 1TB
#Change Accele  Slope  Tasks    Accele   Slope  Tasks    Accele   Slope   Tasks
1       3.41   -2.25  2.94     3.44   -5.25  6.89      5.75   -10.25   17.39
2       3.41   -2.25  2.94     6.49   -4.25  7.65      7.83    -9.25   18.30
3      19.90   -1.25  3.94     6.49   -4.25  7.65     11.04    -8.25   19.38
…
*********************************************************************************
For Terasort 10GB, the recommended number of task resources is   3.94
For Terasort 10GB, the recommended number of task resources is   8.82
For Terasort 100GB, the recommended number of task resources is  10.52
For Terasort 100GB, the recommended number of task resources is  14.11
For Terasort 1TB, the recommended number of task resources is  24.29
For Terasort 1TB, the recommended number of task resources is  27.00
For Terasort 1TB, the recommended number of task resources is  30.88
*********************************************************************************
First recommended number of tasks for same workload provides highest efficiency
in performance/energy ratio. Subsequent number(s) slightly improves job runtime.
```

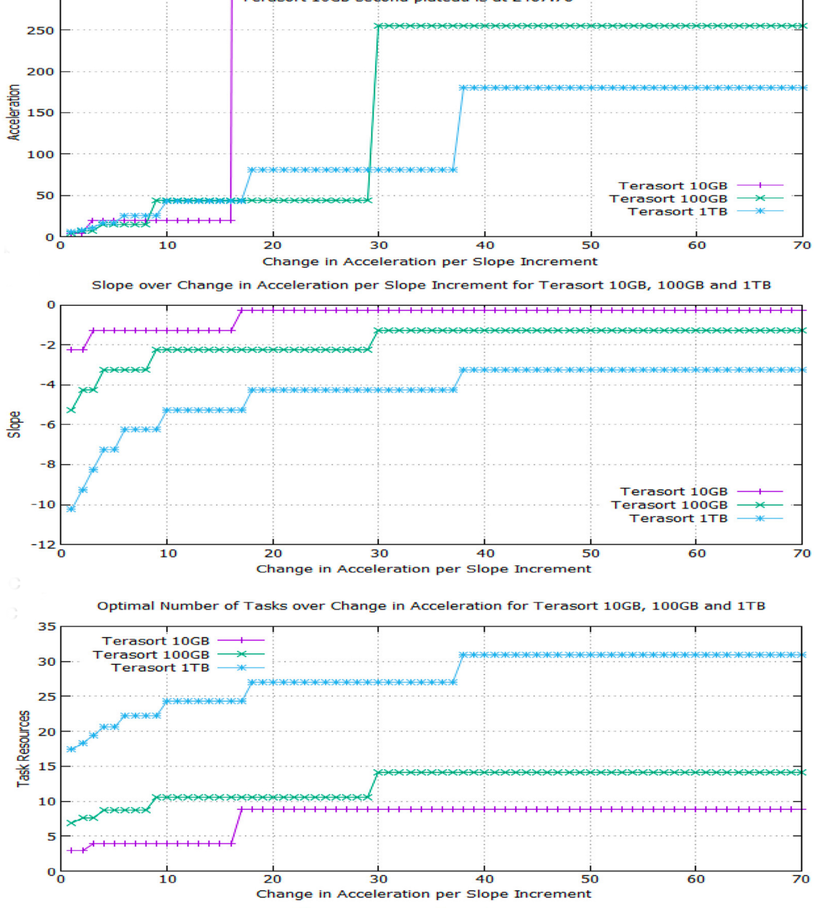

Best Trade-off Point Algorithm

Algorithm BestTrade-offPoint for an Elbow Curve *f(x)=(a/x)+b*
Input: Parameter *a* for a workload with runtime curve *f(x)=(a/x)+b*
Output: Optimal number of tasks

foreach *incremental slope value* **do**
    output *number of tasks x=sqrt(-a/slope)*;
end
foreach *incremental slope value* **do**
    output *acceleration=2a/pow(slope, 3)*;
end
foreach *incremental target value of change in acceleration* **do**
    foreach *incremental slope value* **do**
        if *change in acceleration in the current slope increment is >= to the target value AND change in acceleration in the next slope increment is < the target value* **then**
            output *acceleration, slope and number of tasks*;
            store *number of tasks in an array register*;
            break;
        end
    end
end
foreach *incremental target of change in acceleration* **do**
    if *numbers of tasks do not change in 8 increments* **then**
        output *number of tasks as recommended optimal value*;
        break;
    end
end

Conclusion and Future Plan

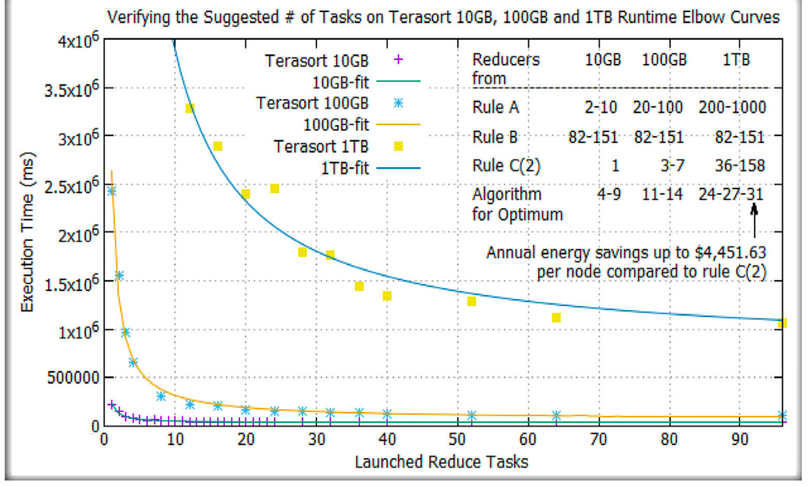

- Compare BToP algorithm (31tasks = 9nodes) to Rule C(2) (158tasks = 44nodes) for an active TDP/node = 250W, idle at 235W, and an average job arrival time of 2000s.
- ***Energy(N) = [$Time_{run}$(N)*$Power_{active}$(N)]+[$Time_{idle}$* $Power_{idle}$]***
  - E(44) = [969s*(250W*44)]+[(2000s-969s)*235W] = 10,901.285kJ = 3.028kW/job
  - E(9) = [1773s*(250W*9)]+[(2000s-1773s)*235W] = 4,042.595kJ = 1.123kWh/job
  - (1.905kWh saved/job)*[(365*24)h/yr)/(2000/3600)h/job)] = 30,038kWh saved/yr
- **Annual saving of $4,451.63/compute node** (for $0.1482/kWh).
- Apply BToP method to other computing systems including Spark.

References

J. Parallel Distrib. Comput. 95 (2016) 29–41. http://dx.doi.org/10.1016/j.jpdc.2016.04.001

PN020817

Enhanced Intra Prediction Mode Coding by using Reference Samples in Video Compression

Promila Agarwal, Michael Schimpf, Dr. Jiang, Dr. Ling
Santa Clara University Computer Engineering

Santa Clara University
School of Engineering

INTRODUCTION

HEVC (High Efficiency Video Coding) utilizes 35 intra prediction modes for prediction of luma block. To ensure the selected mode for a luma block is signaled with minimal overhead, HEVC defines a set of three most probable modes (MPM) , which are derived based on the modes of its two neighbors. If the intra prediction mode is not one of these three MPM, it is coded as one of the remaining modes. To further improve the coding efficiency for intra prediction mode, this disclosure presents a method to derive a second set of most probable modes, by using neighboring reconstructed pixels.

What is intra prediction mode coding ? Where and Why is it used ?
Intra frame prediction exploits spatial redundancy, i.e. correlation among pixels in the same frame, by calculating prediction values through extrapolation from already coded pixels.

What are most probable modes (MPM) ?

In general, the mode of the current block has a higher probability to be one of the neighboring blocks. The block if encoded by one of the MPM's can be encoded with less number of bits than the total set of modes (32 modes needs 5 bits, three modes need just 3 bits!)

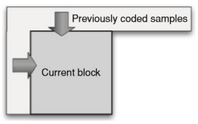

Intra prediction: spatial extrapolation

ALGORITHM

To improve the coding efficiency of intra prediction mode, this disclosure presents an approach to derive a second set MPM, by using neighboring reconstructed samples.

(0, 0) specifies the top-left sample of the current luma prediction block of size NxN.
P(x, y) specifies reference samples of the current block with x < 0 or y < 0 or both less than zero.
For example, 4N+1 reference samples with:
x = -1, y = -1..N * 2 − 1 and
x = 0..N * 2 − 1, y = −1, are used to predict the current block in HEVC.

The steps to derive the second set MPM:

1. A block of size NxN is created/generated with a luma location (-L, -L) specifying the top-left sample of this block relative to the top-left sample of the current luma block.
   In the following figure 2, a 4x4 block is used as an example.
2. The original samples origSamples(x, y) of the created block with
   x = -1, y = -1..N - 2 and x = 0..N – 2, y = -1, are filled by corresponding reference samples.
   These reference samples are derived using the substitution process in HEVC.
3. The neighboring reference samples of this created block with x = -2, y = -2..N*2 – 2 and x = -1..N*2 – 2, y = -2, are derived using the substitution process in HEVC. In the following figure 3, a 4x4 block is used as an example.
4. ModeIntra is used to denote one of the available intra prediction modes. The total number of intra prediction modes, is denoted as NumModes. The predicted samples predSamples(x, y) with x = -1, y = -1..N - 2 and x = 0..N – 2, y = -1, are derived by using the 4N+1 reference samples from step 3 for each ModeIntra = 0..NumModes – 1, following the intra prediction process in HEVC. All modes in the first MPM set may be excluded. For each ModeIntra, the distortion between origSamples(x, y) and predSamples(x, y) is measured by SAD (Sum of Absolute Difference), denoted as sad(ModeIntra).
5. All SAD values obtained in step 4, are then sorted in increasing order together with their corresponding modes. The first M modes with the smallest SAD values are chosen as the second set MPM, in the sorted order.
6. The intra prediction mode coding is enhanced by using the second set MPM as shown in Figure 4.

Enhanced Intra Prediction Mode Illustrated

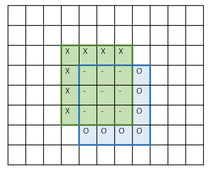

Figure 1 In this figure a 4x4 block is used. Blue rectangles (with "O" inside) is the current luma block with top left location (0,0). Green rectangles (with "X" inside) is the created luma block which is filled with reference samples, with top left location (-1, -1). Green rectangles (with "-" inside) are not filled.

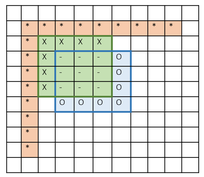

Figure 2. Blue rectangles (with "O" inside) is the current luma block with top left sample location (0,0). Green rectangles (with "X" inside) is the created luma block which is filled with reference samples, with top left location (-1, -1). Green rectangles (with "-" inside) are not filled. Red rectangles (with "*" inside) are the neighboring reference samples of this created block with
x = - 2, y = -2..N*2 – 2 and x = -1..N*2 – 2, y = -2.

```
if  prev_intra_luma_pred_flag
      mpm_idx
else
   if  sec_intra_luma_pred_flag
         mpm_idx2
   else
         rem_intra_luma_pred_mode
```

Fig. 4 Modified intra prediction mode coding using second set MPM

```
If prev_intra_luma_pred_flag
      mpm_idx
else
      rem_intra_luma_pred_mode
```

Fig. 1 Current HEVC intra prediction mode coding

EXPERIMENTAL RESULTS

The proposed method is implemented on top of HM-16.6 (HEVC Test Model 16).
In the tests, the number of modes in the second set is set to be 4. This value is determined based on extensive testing results. Using smaller or larger value, for example, 3 or 5 will degrade overall BD-rates. The BD-rate performance over HM-16.6 is demonstrated in Table I. It shows that the proposed method effectively reduces the BD-rates for all video classes except Class A1 for U. The reduction of BD-rate can be up to -0.99% with an average -0.54%, -0.34%, and -0.34% for Y, U, and V, respectively

TABLE I. BD-rate performance of proposed method compared with HM-16.6 (AI Main 10)

Video Sequence Classes	Y BD-rate	U BD-rate	V BD-rate	Enc Time (%)	Dec Time (%)
Class A1	-0.32%	0.02%	-0.12%	111%	111%
Class A2	-0.68%	-0.34%	-0.34%	111%	114%
Class B	-0.39%	-0.20%	-0.20%	109%	114%
Class C	-0.60%	-0.47%	-0.56%	103%	120%
Class D	-0.44%	-0.47%	-0.29%	95%	138%
Class E	-0.99%	-0.72%	-0.60%	108%	119%
Overall	-0.54%	-0.34%	-0.34%	106%	119%

The effectiveness of proposed method can be evaluated in a different point of view. It is well known that if the intra prediction mode of the current block equals to one of mode in MPM set then coding the index of this MPM will use less bits than coding the remaining mode. It is expected that more PUs are hit by MPM set(s).

totalPU as total number of PUs,
totalPUHitFirst as total number of PUs hit by the first set,
totalPUHitSecond as total number of PUs hit by the second set,
totalPUHitFirstAndSecond as total number of PUs hit by both sets altogether,
origTotalPURemaining as total number PUs not hit by the first set,
finalTotalPURemaining as total number PUs coded using remaining modes
Some relations among above defined:
totalPU = totalPUHitFirst + totalPUHitSecond + finalTotalPURemaining
origTotalPURemaining = totalPU - totalPUHitFirst
Then we define the hit rates as following:
HitRateFirst = totalPUHitFirst / totalPU,
HitRateSecond = totalPUHitSecond/ totalPU
HitRate1Plus2 = totalPUHitFirstAndSecond/ totalPU,
FinalHitRateRem = finalTotalPURemaining / totalPU
HitRateSecOvrOrigRem = totalPUHitSecond / origTotalPURemaining

TABLE II. BD-rate performance of proposed method compared with HM-16.6

Video Sequence Classes	HitRateFirst	HitRateSecond	HitRate1Plus2	FinalHitRateRem	HitRateSecOvrOrigRem
Class A1	67.57%	18.41%	85.98%	14.02%	56.77%
Class A2	63.88%	23.08%	86.96%	13.04%	63.91%
Class B	65.84%	21.11%	86.95%	13.05%	61.70%
Class C	57.39%	25.61%	83.00%	17.00%	60.11%
Class D	51.40%	26.63%	78.03%	21.97%	54.80%
Class E	59.69%	29.22%	88.92%	11.08%	72.50%
Overall	60.96%	24.01%	84.97%	15.03%	61.65%

CONCLUSIONS

Testing results of above defined hit rates are presented in Table II. It shows that *HitRateSecOvrOrigRem* can reach 61.65%, which means that PU originally having to be coded using remaining modes, is coded using the index of the second MPM set. This proves the effectiveness of the proposed method. On average, *HitRateFirst, HitRateSecond, HitRate1Plus2, and FinalHitRateRem* are 60.96%, 24.01%, 84.97% and 15.03%, respectively. The major contributor of coding efficiency is the first set. Further improvement comes from the second set. Both sets altogether can hit 84.97% PUs and leave only 15.03% coded using remaining modes.

BACKGROUND

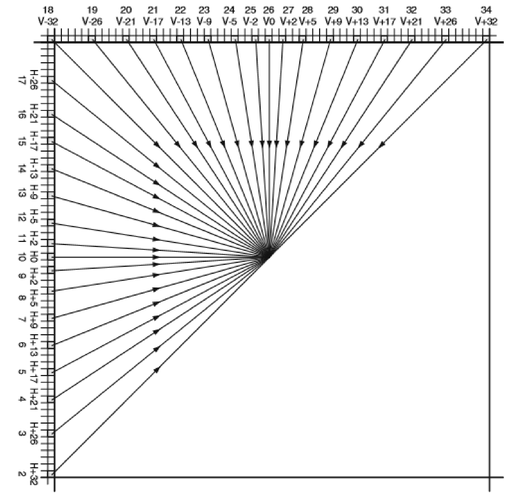

Fig. 4.5 Angle definitions of angular intra prediction in HEVC numbered from 2 to 34 and the associated displacement parameters. *H* and *V* are used to indicate the horizontal and vertical directionalities, respectively, while the numeric part of the identifier refers to the sample position displacements in 1/32 fractions of sample grid positions. Reproduced with permission from [8], ©

FUTURE DIRECTIONS...

-- Fast Search Algorithm for bringing down the timing
-- Moving the implementation to JEM4 (Next generation HEVC)
-- Incorporating Probability estimates for a Fast Search generation
-- Alternate Methods for Intra Mode Prediction

ACKNOWLEDGEMENTS

Thanks to Dr. Jiang for lots of advise! Thanks to Dr. Ling for supporting research!
References: Patent Application Number 62425425
Books referenced: HEVC Video Coding (Algorithms & Architecture)The H.264 Advanced Video Compression Standard

Personalized Data Visualization Aids for Improving Visualization Understanding

Undergraduate Student: **Renee Prescilla**
Faculty Advisor: **Ben Steichen**
Department: **Computer Engineering**

Santa Clara University
School of Engineering

Why Data Visualization Aids?

With so much crucial information in the world, it's important to know how to effectively handle information overload.
I am investigating what types of visualizations and aids hinder, aid, or have no effect on how different people analyze information.

The overall goal is to know what visualization aids help different users parse information. Knowing this, our research will help users better understand the underlying data through personalized visualizations and visualization aids.

Research Plan

Current Step

- **Create visualizations and aids**
  using HTML/CSS and the Javascript library D3.js.
- **Set up study sequences and surveys for user testing**
  and apply for SCU IRB approval to conduct studies.
- **Conduct user studies with 30 participants**,
  compensating participants with a $20 voucher.
- **Perform statistical analysis and write academic paper**
  that will be submitted to a scientific conference or paper.

Visualizations and Visualization Aids

We focused our study to use common visualizations, mainly **bar, line, and pie graphs**. For visualization aids, we narrowed down to a handful of aids, including enabling vertical/horizontal/dot grids and area-filling.

We have a total of **10 different graphs** for our study. We are using 2 sets of data. Each set has a high and low information density graph. High density graphs have line and bar graphs; pie graphs have line, bar, and pie graphs.

Conducting User Studies

For our user studies, we have created sequences of tasks that participants will go through. We have stored them using MySQL tables and we will use separate tables to record answers, aid usage, and performance time.

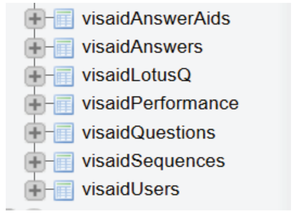

We plan to have **30 sequences with 50 tasks** each.
While each particpiant will answer the same questions, each task will be a random combination of a question and a graph.

We plan on conducting the studies on campus using **eye-tracking devices** provided by SCU to further study how people interact with the visualization and visualization aids.

Partipants will each receive a $20 voucher as compensation.

Sample Visualizations and Tasks

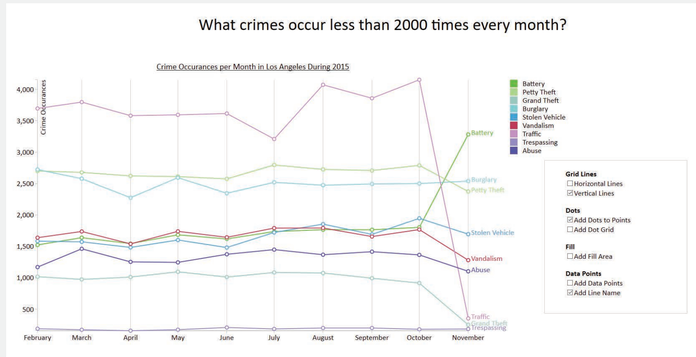

High Density Line Graph
with a horizontal grid and dot point aid enabled.

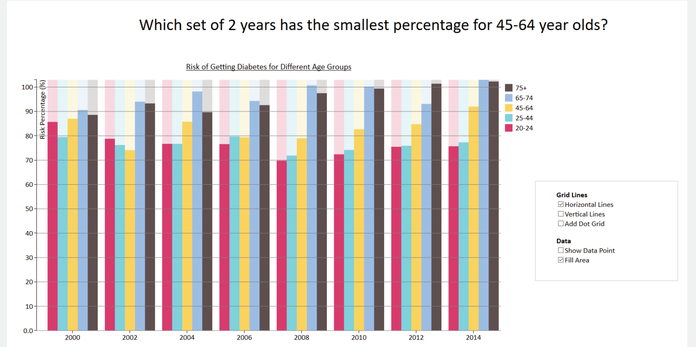

High Density Bar Graph
with the 'fill area' and 'horizontal grid' aid enabled.

Aggregated Search User Interface Research

Dr. Ben Steichen and Robert Bayer

Santa Clara University Department of Computer Engineering

Introduction

A key challenge for search systems lies in their ability to *retrieve* and *present* the right information in the right form for each individual user's needs, abilities, preferences, and context. In particular, a wide variety of content may be presented to each user for a given query (e.g. web results, news results, images, video, etc.), and search engines crucially need to decide *what* and *how* this information should be presented. In recent years, a new search paradigm called *Aggregated Search* has emerged, which attempts to achieve search result page diversity by presenting search results from different information sources, or verticals, in addition to the standard web results, on one result page [1]. However, this type of search system has seldom been personalized to individual users, as adaptation typically only focuses on the queries.

Objectives

The objectives of our research into Aggregated Search systems are to:

- Identify which individual user characteristics (e.g. cognitive style, cognitive abilities, personality) have an effect on user experiences, behaviors, and preferences
- Develop the first personalized algorithms for modern aggregated search interfaces using the identified characteristics in order to display tailored result pages for increasingly diverse individual users

Our research aims to generate the first personalization of modern aggregated search interfaces, in order to better serve increasingly diverse users. By analyzing eye gaze data, the research aims to tie individual cognitive abilities, such as perceptual speed, visual working memory, and verbal working memory to specific preferred interfaces [2]. The goal of the presented experiment is to gather significant user behavioral data in order to ultimately design and develop novel *Personalized Aggregated Search* systems that adapt to a large variety of individual needs, abilities, preferences, and context.

Research System Design

The three interfaces of interest are **Blended** (Fig. 1), **Panelled** (Fig. 2), and **Tabbed** (Fig. 3). Our custom system will be able to test the effects of different verticals in different layouts in each interface.

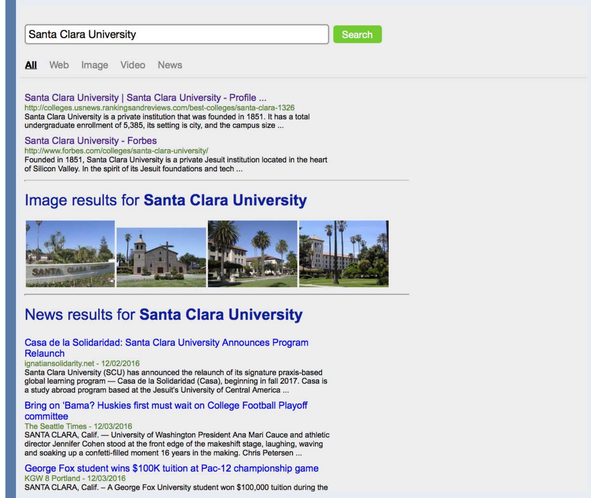

Figure 1: Blended Display of Search Results

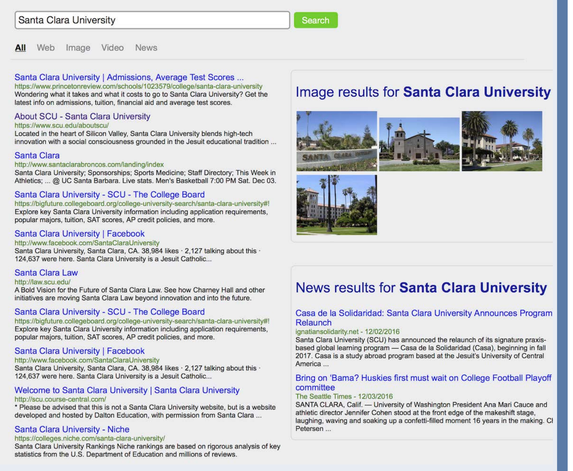

Figure 2: Panelled Display of Search Results

Materials

The following materials are required to complete the research:

- Software research system with the ability to control the interface and record user data during sessions
- Eye tracker and physiological sensors

Procedure

After the participant fills out a consent form and answers a short demographic questionnaire and cognitive tests using the standard Ekstrom Kit, the following procedure will be performed with each interface option in a controlled order with different tasks:

1. The participant receives training and instructions for the system prototype
2. The eye tracker and physiological sensors are calibrated
3. The participant performs a practice task using the system prototype
4. The eye tracker and physiological sensors are re-calibrated
5. The participant performs 3 tasks using the system prototype
6. The participant fills in the usability and cognitive load questionnaires for this specific system

After performing the above steps for all three systems, the participant will fill in the final exit comparative questionnaire.

Current State

The initial interface layouts (shown in the images below and to the left) have been developed and are currently being integrated into an experimental software framework to handle the controlled administration and data collection of the experiment. After this stage of development, the user studies will begin.

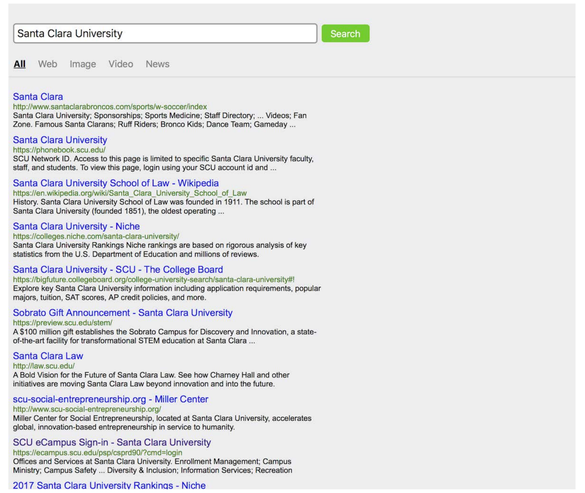

Figure 3: Tabbed Display of Results from a Single Vertical

References

[1] Mounia Lalmas.
Aggregated search.
In *Advanced topics in Information Retrieval*, pages 109–123. Springer Berlin Heidelberg, 2011.

[2] Ben Steichen, Cristina Conati, and Giuseppe Carenini.
Inferring visualization task properties, user performance, and user cognitive abilities from eye gaze data.
ACM Trans. Interact. Intell. Syst., 4(2):11:1–11:29, July 2014.

Contact Information

Dr. Ben Steichen

- Email: bsteichen@scu.edu
- Web: http://www.engr.scu.edu/~bsteichen

Robert Bayer

- Email: rbayer@scu.edu

Applications of Adaptive Navigation of Multirobot Clusters

Robert McDonald; Advisor: Dr. Christopher Kitts
Department of Mechanical Engineering
Santa Clara University
School of Engineering

Abstract

Sensor based adaptive navigation techniques are a powerful class of controllers that can enable more time-efficient exploration and search of scalar characteristics of a field of interest (e.g., temperature, concentration level, etc.). With this presentation we report on our identification of a complete class of reactive multirobot adaptive navigation control primitives and how they may be sequenced to perform real world applications of interest.

Real World Applications

- **Environmental Sensing** – Identify critical quantities, locate resource caches and starvation zones, etc.
- **Disaster Response** – Locate/identify harmful quantities, safety thresholds, and minimum exposure paths
- **Exploration** – Find features of interest using a methodical search that exploits knowledge of the field

Acknowledgements

Strickland Scholarship Fund
Robotic Systems Laboratory
Michael Neumann
School of Engineering
Monterey Bay Aquarium Research Institute
National Institute of Underwater Science and Technology
NOAA

Background

The Robotic Systems Laboratory has developed the first complete set of control multirobot adaptive navigation control primitives capable of locating or moving along all critical features of a scalar field.

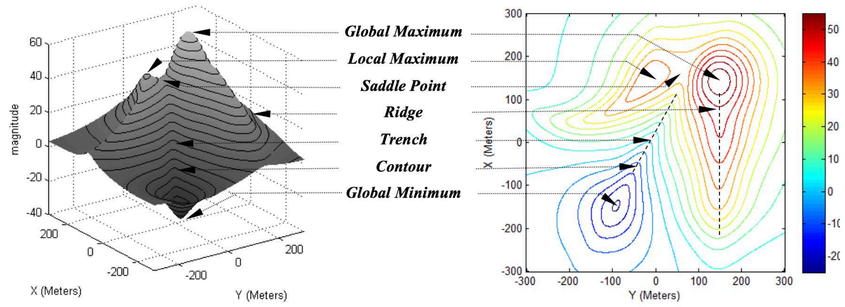

Mission Scenarios

Three scenarios were implemented in a simulation environment to verify their viability. These methods make use of the control primitives above, applying them in a sequence appropriate to the objective. The transitions between controllers are dependent upon current conditions and sequenced by a state machine.

Peak Exploration:
Moving from one maximum to another

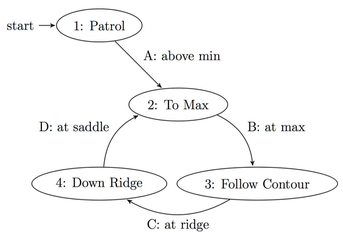

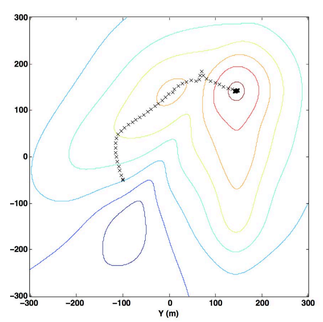

Characterizing a Peak:
Mapping the contours around a maximum

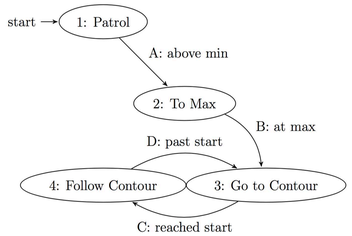

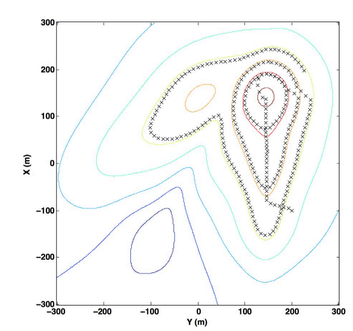

Maintain Service:
Maintaining a scalar magnitude while traveling to a set point

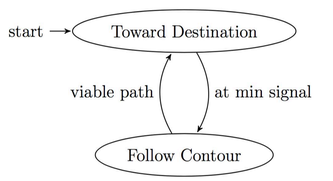

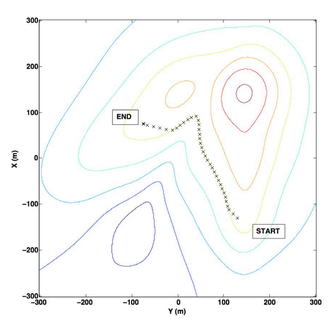

Control Architecture

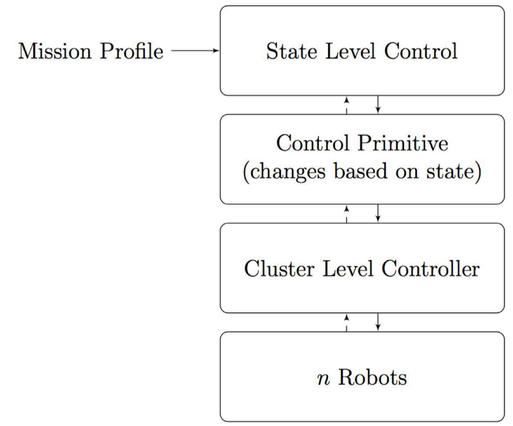

- **Robot**: Manages individual robot dynamics
- **Cluster**: Responsible for keeping formation
- **Primitive Controller:** Navigates a basic feature of the field
- **State Level:** Links primitive controllers to achieve mission objective.

Conclusion

Multiple scenarios were successfully implemented and verified in a simulation environment, laying the groundwork for field testing and application.

Future Work

- Field experiments
- Applications with Industry Partners
- More robust transition criteria
- Additional backtracking prevention
- 3D and time-varying fields

Santa Clara University
School of Engineering

A Novel Algorithm for MPM Derivation

Shanxi Li, Nam Ling, Minqiang Jiang
Department of Computer Engineering

INTRODUCTION

- Coding Unit (CU) is a basic processing unit in image and video compression formats. A Coding Unit consists of from 256 x 256 samples to 8 x 8 samples.
- There are very close relationships within the neighboring units.
- These relationships are used to predict and compress image.

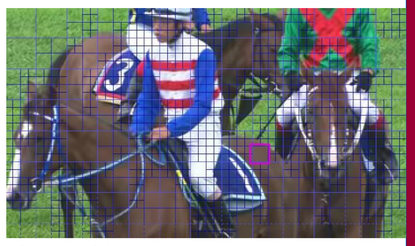

$$e(x,y) = f(x,y) - f'(x,y)$$

- There are billions of relationships in the composition of neighboring units.
- The purpose of this proposal is to figure out and simplify the relationships by offline learning methods.

METHOD

- For each CU, 6 Most Probable Modes (MPMs) is used to predict the direction mode of current CU.

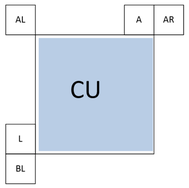

- A fixed MPM list is equal to {*left, above, planar, DC, below left, above right, above left, left - 1, left + 1, above - 1, above + 1, below left - 1, below left + 1, above right - 1, above right + 1, above left - 1, above left + 1, vertical, horizontal, 2, diagonal*}.
- The first 6 available and different modes are used as derivation the MPMs since the modes in above list might be same or not exist.
- Each neighboring block is classified into 8 statuses:
  0 status, the prediction mode of this neighboring block is equal to Planar mode.
  1 status, the prediction mode of this neighboring block is equal to DC mode.
  2 status, the prediction mode of this neighboring block is from 2 to 14 (zone 1).
  3 status, the prediction mode of this neighboring block is from 15 to 27 (zone 2).
  4 status, the prediction mode of this neighboring block is from 28 to 40 (zone 3).
  5 status, the prediction mode of this neighboring block is from 41 to 53 (zone 4).
  6 status, the prediction mode of this neighboring block is from 54 to 66 (zone 5).
  7 status, this neighboring block is not exist.

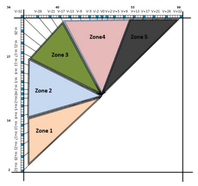

- Current CU is classified into 8 statuses depend on its shape and size

- **Status_id** = **AL** + **AR***8 + **BL***8^2 + **A***8^3 + **L***8^4 + **Size***8^5 + **Shape***8^6
- For the MPM list
  {*L, A, 0, 1, BL,AR,AL,L-1,L+1,A-1,A+1,BL-1,BL+1,AR-1,AR+1,AL-1,AL+1, 50, 18, 2, 34*}
- The following hit probabilities list correspondingly
  $\{P_0,P_1,P_2,P_3,P_4,P_5,P_6,P_7,P_8,P_9,P_{10},P_{11},P_{12},P_{13},P_{14},P_{15},P_{16},P_{17},P_{18},P_{19},P_{20}\}$

$$P_i = \left(\frac{Sum\ of\ hit\ PU\ by\ Item_i}{Sum\ of\ PU\ in\ a\ frame} \mid Status\_id\right)$$

- Sort the list by P_i from maximum to minimum.
- Sort the ***Item*** by P_i correspondingly to derivate new order of first MPM list.

DIAGRAM OR EXAMPLE OF STIMULI

- Extracting 655,360 status from billions of probable status to predict mode of current CU. (Left Fig.)

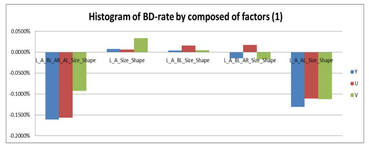

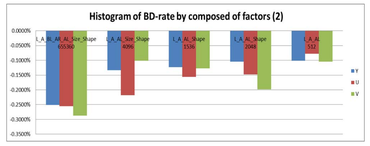

Figure out the most important factors for prediction current CU.

- Fixed MPMs lists derivation under only 6 conditions.

	A (above)
L (Left)	CU

Conditions			MPM0	MPM1	MPM2	MPM3	MPM4	MPM5
L=A	L≠Planar and L≠DC		L	Planar	L+1	L-1	L+2	DC
	Otherwise		Planar	DC	50 (Ver)	18 (Hor)	2	34
L≠A	L≠Planar and R≠Planar	L=DC or A=DC	L	A	Planar	Max-1	Max+1	Max+2
		otherwise	L	A	Planar	DC	Max+1	Min-1
	otherwise	L+A<2	L	A	50(Ver)	18(Hor)	2	34
		otherwise	L	A	DC	Max-1	Max+1	Max+2

RESULTS

- The proposed method is implemented using the JEM-3.0 framework. The following tables summarize the experimental results for AI configuration following the JVET common test conditions.
- Table 1. This proposal compared with JEM-3

	Over JEM-3.0 655360_33				
	Y	U	V	EncT	DecT
Class A1	-0.12%	-0.12%	-0.04%	105%	100%
Class A2	-0.27%	-0.20%	-0.25%	104%	102%
Class B	-0.12%	-0.04%	-0.13%	105%	99%
Class C	-0.25%	-0.23%	-0.25%	100%	100%
Class D	-0.19%	-0.24%	-0.02%	99%	107%
Class E	-0.44%	-0.39%	-0.44%	104%	102%
Overall	-0.22%	-0.19%	-0.18%	103%	101%

Table 2. JEM-3.0 compared with last version

	Over JEM-2.0 QTBT				
	Y	U	V	EncT	DecT
Class A1	-0.08%	-0.04%	-0.09%	100%	101%
Class A2	-0.27%	-0.21%	-0.27%	102%	102%
Class B	-0.19%	-0.16%	-0.18%	96%	93%
Class C	-0.21%	-0.15%	-0.31%	95%	97%
Class D	-0.03%	-0.05%	-0.05%	99%	99%
Class E	-0.19%	-0.19%	-0.24%	97%	95%
Overall	-0.16%	-0.13%	-0.19%	98%	98%

CONCLUSIONS

- In this proposal, a novel adaptive derivation MPM list algorithm for intra prediction was presented.
- This proposal described the details of extracting 655,360 status from billions of probable status to predict mode of current CU.
- As a result, the proposed algorithm decreased BD rate down to -0.44% compared to the test model JEM3.0, moreover the increased encoding and decoding time is acceptable.
- Since the MPM list is derived differently from the anchor, context modeling has to be modified as well.
- To signal an MPM index, only first three bins are context coded (as in the anchor), but context modeling is defined based on the MPM mode related to the bin currently being signaled, the MPM mode is classified into one of three categories: (a) whether the mode belongs to horizontal (MPM mode is less than or equal to diagonal direction), (b) vertical (MPM mode greater than the diagonal direction), or (c) non-angular (DC and planar) class. As a result, only three contexts are used to signal the MPM index, instead of the 9 contexts that are used for the anchor.

FUTURE DIRECTIONS...

- To ensure the selected mode for a block is signaled with minimal overhead, second set of most probable modes is defined. The selection is based on the modes of its five neighboring blocks. Machine learning methods will be used to derivate the relative table(or a dictionary) for Most Probable Modes (MPMs)
- To further improve the coding efficiency for intra prediction mode, using this method to derive a second set of MPMs.
- The method in this disclosure is friendly for hardware implementation and nearly no coding loss for the current design. The depth map intra coding complexity for hardware implementation is reduced.
- To derivate the MPMs, more than five neighbour blocks will be references. Which reference blocks are farther than current five neighbours.
- To further simplify the computations.

Molecular Dynamics Study of Self-diffusion Along Dislocations in FCC Metals

Siavash Soltani, Panthea Sepehrband
Department of Mechanical Engineering, Santa Clara University

Santa Clara University
School of Engineering

Abstract

Self-diffusion along a screw dislocation core in Al, Ni, Cu and Ag is studied using molecular dynamics. Simulations show that the mobility of atoms is significantly higher in dislocation core regions than in bulk. We observed that the dislocation core acts as a high diffusivity path for atoms, which is due to high distortion in these regions. More over, it was found that the diffusivity at high temperatures depends on the stacking fault energy and the configuration of partial dislocations.

Motivation: Ultrasonic Bonding

Ultrasonic bonding is the method of making interconnections between IC and its packaging, using a combination of force, temperature and ultrasonic power.

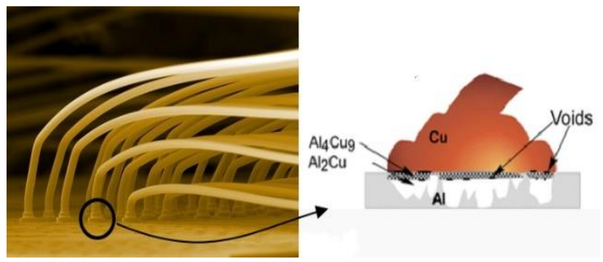

Formation of intermetallic phases at the interface of the wire and the pad during ultrasonic bonding

Aluminum, gold or copper wires are bonded to a pad, often made of Al. Formation of intermetallic phases at the interface of the wire and the pad, which is a diffusion-controlled process, strongly affects the conductivity and strength of the bond. It has been suggested that plastic deformation caused by ultrasonic vibrations increases the dislocation density at the interface, which leads to higher diffusion rates.

Method of Simulation

- Molecular Dynamics (MD) and LAMMPS package are utilized.
- A cylindrical model is used with the dislocation core at the center of the cylinder:

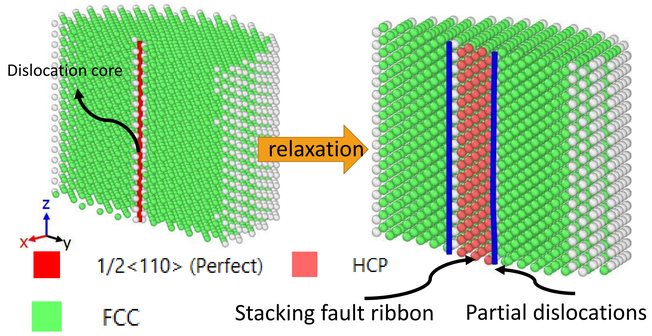

- To study self-diffusion in each of the metals, the temperature is ramped up to a target value during 1 nanosecond followed by 30 ns of isothermal annealing.

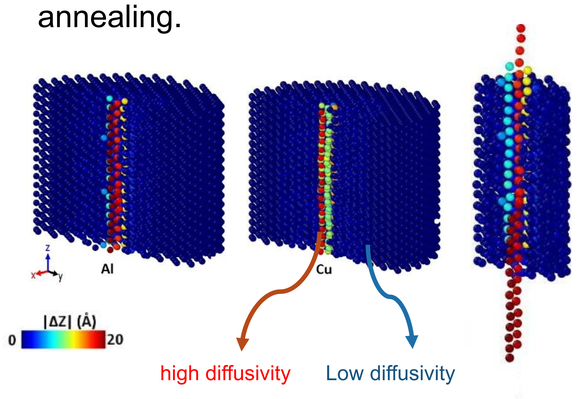

Atoms are colored using displacement magnitude after annealing. It can be observed that atoms in core regions have higher mobility than atoms in perfect lattice regions. This confirms that the diffusivity is higher in dislocation core regions than in bulk.

Results and Conclusion

To find the activation energy of self-diffusion along the dislocation core (E_d), Mean Squared Displacement (M.S.D) of atoms along the dislocation core are plotted vs. time, and diffusion coefficient (D) is calculated vs. the distance from the dislocation core, R: $MSD = 2Dt$

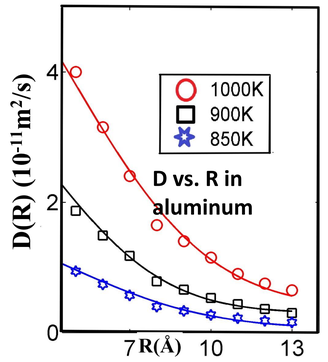

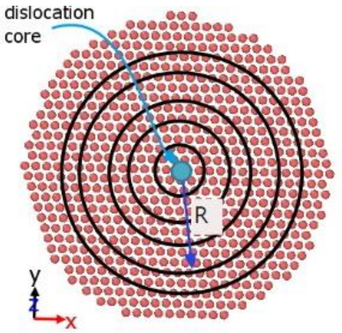

Activation energies are then calculated using Arrhenius relation, as reported in Table: $D_d = D_d^0 exp\,(-\frac{E_d}{kT})$

Element	E(bulk) eV	E_d eV	E(bulk) / E_d
Al	1.2	0.57	0.48
Ni	2.76	1.58	0.57
Cu	1.96	1.61	0.82

Lower activation energy of self-diffusion along the core (E_d), than activation energy of self-diffusion in bulk confirms high diffusivity of atoms in core regions of dislocation. It can be observed that the effect of dislocation on enhancing the diffusion is more remarkable in Al and Ni than in Cu, which is due to high stacking fault energy and low dissociation distance of partial dislocations (which leads to high distortion in core regions) in Al and Ni.

Acknowledgement

This work was supported by Santa Clara University, School of Engineering. We thank Dr. Abdolrahim from University of Rochester for her constructive comments in this research. Resources for fast computing were provided by the Center for Integrated Research Computing (CIRC) at University of Rochester.

Causal Modeling for Data Security and Protection of Transparency

Dr. Suchitra Abel | Adel Abdalla | Department of Computer Engineering, Santa Clara University

Santa Clara University
School of Engineering

Background

There is a current trend in improving the quality and protection of research related to transparency. Data Sharing security is an issue that has attracted attention from various fields.

While there is an ever growing body of literature on the negative consequences of poor research transparency (fraud and misuse of vital research data placed in open source, by certain users) there is almost no operational research related to protection of research transparency that exists.

We need solutions, based on research, that improve the protection of transparency in open source data.

Research design/program

We investigate and use TETRAD V, a heuristic, Artificial Intelligence based software that can be used for discovering cause-effect relationship between variables based on a specific model. To perform our task, we have to define some case studies. Using our data, we should find results of causal linkage. It is critical to explore the relationships among the variables in the model, for example, those that represent some aspect of data breaches, using exploratory research tools, as those present as modules within TETRAD V, to aid and guide the researcher. Our program will perform this task.

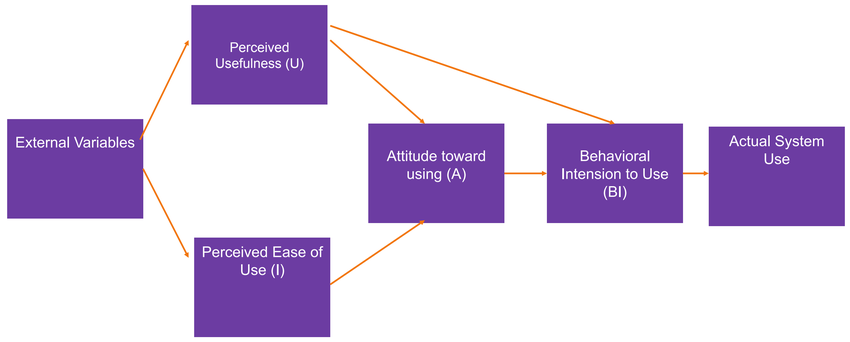

Technology Acceptance Model

Objectives

We will develop a practical view and implementation of how to share data in a way that protects privacy. The discovery of causal relationships from empirical data is an important problem in data sharing security.

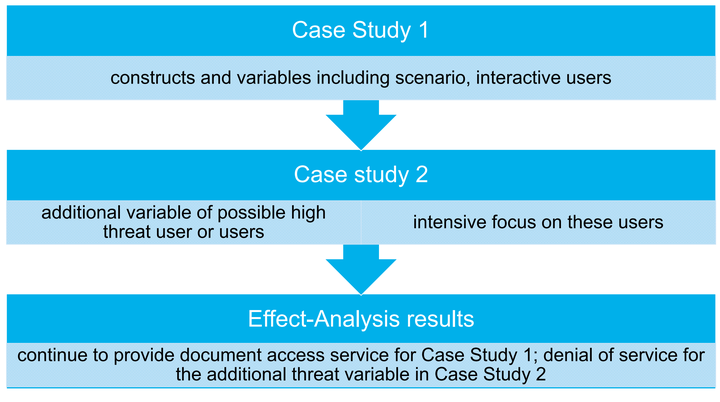

Conclusion and plans

Building of an actual computer program is ongoing. Once built, it will be tested by the utilization of different scenarios and the results will be noted. Statistical analysis of the results will be provided. Evaluation will include possible minor alteration as the practical cases demand. The future plans include dissemination of the results in the form of journal publication and research grant application.

Variational Deep Semantic Hashing for Text Documents

Suthee Chaidaroon, Yi Fang

Department of Computer Engineering,
Santa Clara University, Santa Clara, CA 95053
{schaidaroon, yfang}@scu.edu

Santa Clara University
School of Engineering

1. Introduction

SEMANTIC HASHING is an effective solution to accelerate similarity search by designing compact binary codes in a low-dimensional space so that semantically similar documents are mapped to similar codes. This approach is much more memory and computational efficient because:

- a binary code requires lesser storage space.
- computing similarity between two binary code is fast (using XOR operation).

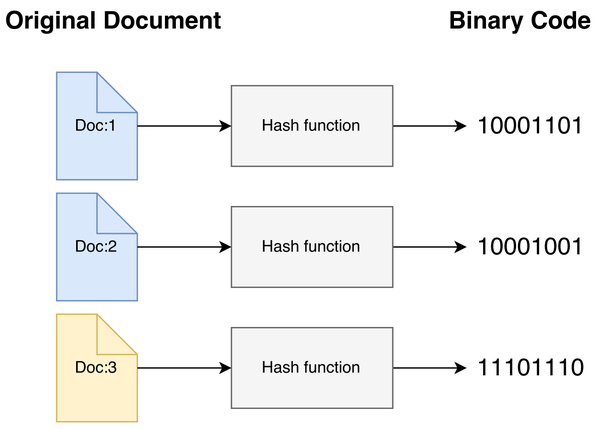

Query Code	Binary Code	XOR	Bit Difference
10001101	10001001	00000100	1
10001101	11101110	01100011	4

2. Objectives

We seek to learn a binary code that is:

1. requires a small number of bits to encode each text document.
2. preserves similarity by mapping similar documents to similar binary code.

3. Contributions

1. We proposed a series of deep learning models for document hashing.
2. The proposed model can learn complex nonlinear distributed representations while providing a principled framework for probabilistic reasoning.
3. The parameter estimation for the proposed models is efficient and scalable.
4. The proposed models have outperformed the competitive baselines.

4. Generative Model

Generative models are a rapidly advancing area of research in deep learning. The main goal is to train the model to generate similar data as the training data. One such approach is to train a deep neural network to approximate the true data distribution.

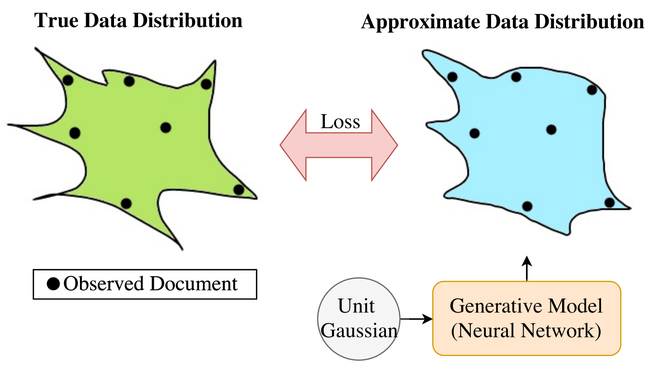

5. Notations

symbols	description
$\boldsymbol{d}$	a document in a bag-of-words representation
$\boldsymbol{w}_i$	the i^{th} vocabulary in $\boldsymbol{d}$
$\boldsymbol{s}$	a semantic latent vector
$\boldsymbol{v}$	a private latent vector
$\boldsymbol{Y}$	a collection of tags/labels
$\boldsymbol{y}_j$	the j^{th} tags/labels in $\boldsymbol{Y}$
$P(\boldsymbol{w}_i\|f(\boldsymbol{s};\theta))$	word likelihood parameterized by neural nets, $f(\boldsymbol{s};\theta)$
$P(\boldsymbol{y}_j\|f(\boldsymbol{s};\tau))$	tag likelihood parameterized by neural nets, $f(\boldsymbol{s};\tau)$
$Q(\boldsymbol{s}\|\boldsymbol{d};\phi)$	an approximate posterior distribution, maps $\boldsymbol{d}$ to $\boldsymbol{s}$
$Q(\boldsymbol{s}\|\boldsymbol{v};\phi)$	an approximate posterior distribution, maps $\boldsymbol{d}$ to $\boldsymbol{v}$
$Q(\boldsymbol{s}\|\boldsymbol{d},\boldsymbol{Y};\phi)$	an approximate posterior distribution, maps $\boldsymbol{d},\boldsymbol{Y}$ to $\boldsymbol{s}$
$P(\boldsymbol{s})$	a prior distribution on $\boldsymbol{s}$
$P(\boldsymbol{v})$	a prior distribution on $\boldsymbol{v}$

6. Unsupervised Learning (VSDH)

This model maps documents with similar themes to similar binary code.

$$\mathcal{L}_1 = \mathbb{E}_Q\left[\sum_{i=1}^{N}\log P(\boldsymbol{w}_i|f(\boldsymbol{s};\theta))\right] - D_{KL}(Q(\boldsymbol{s}|\boldsymbol{d};\phi)\parallel P(\boldsymbol{s})) \quad (1)$$

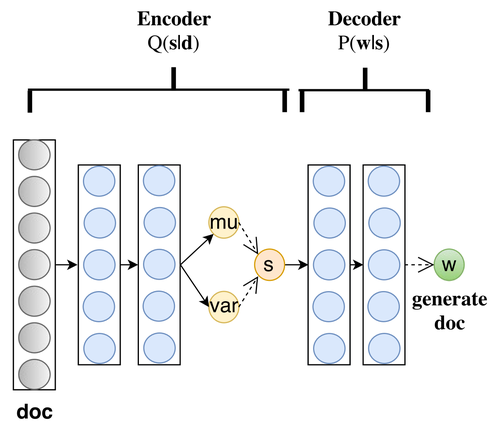

7. Supervised Learning (VDSH-S)

This model extends the VSDH by utilizing document tags. Documents with similar tags and themes will be mapped to similar binary code.

$$\mathcal{L}_2 = \mathbb{E}_Q\left[\sum_{i=1}^{N}\log P(\boldsymbol{w}_i|f(\boldsymbol{s};\theta)) + \sum_{j=1}^{L}\log P(\boldsymbol{y}_j|f(\boldsymbol{s};\tau))\right] - D_{KL}(Q(\boldsymbol{s}|\boldsymbol{d},\boldsymbol{Y};\phi)\parallel P(\boldsymbol{s})) \quad (2)$$

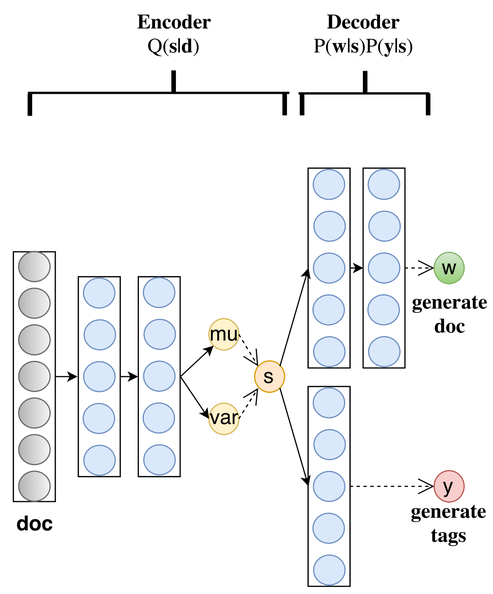

8. Document-specific Modeling (VDSH-SP)

This model extends VDSH-S by adding a private variable to capture document specific information. The private variable allows the model to keep only relevant information in a semantic latent vector $\boldsymbol{s}$, while the rest will be in $\boldsymbol{v}$.

$$\mathcal{L}_3 = \mathbb{E}_Q\left[\sum_{i=1}^{N}\log P(\boldsymbol{w}_i|f(\boldsymbol{s}+\boldsymbol{v};\theta)) + \sum_{j=1}^{L}\log P(\boldsymbol{y}_j|f(\boldsymbol{s};\tau))\right] - D_{KL}(Q(\boldsymbol{s}|\boldsymbol{d};\phi)\parallel P(\boldsymbol{s})) - D_{KL}(Q(\boldsymbol{v}|\boldsymbol{d};\phi)\parallel P(\boldsymbol{v})) \quad (3)$$

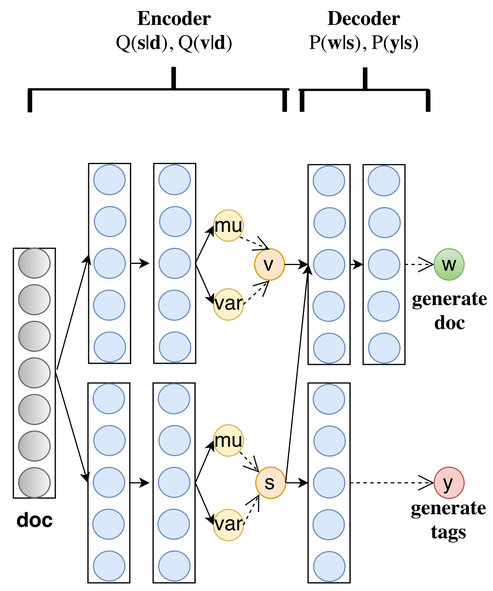

9. Results

	32 bits			
Methods	RCV1	Reuters	20ng	TMC
LSH [1]	0.4716	0.3862	0.0666	0.4514
SpH [5]	0.7475	0.6513	0.3709	0.6281
STHs [6]	0.5592	0.7554	0.5860	0.4105
Stacked RBMs [3]	0.6130	0.6154	0.0533	0.5166
KSH [2]	0.9221	0.8480	0.6103	0.7047
SHTTM [4]	0.9258	0.8323	0.2357	0.6485
VDSH	0.8481	0.7753	0.4327	0.7108
VDSH-S	**0.9801**†	**0.9337**†	**0.7564**†	0.7883†
VDSH-SP	0.9788†	0.9283†	0.7125†	**0.7891**†

Table 3: *Precision of the top 100 retrieved documents on four datasets with the 32-bit hash code. The bold font denotes the best result at that number of bits. † denotes the improvement over the best result of the baselines is statistically significant based on the paired t-test (p-value < 0.01).*

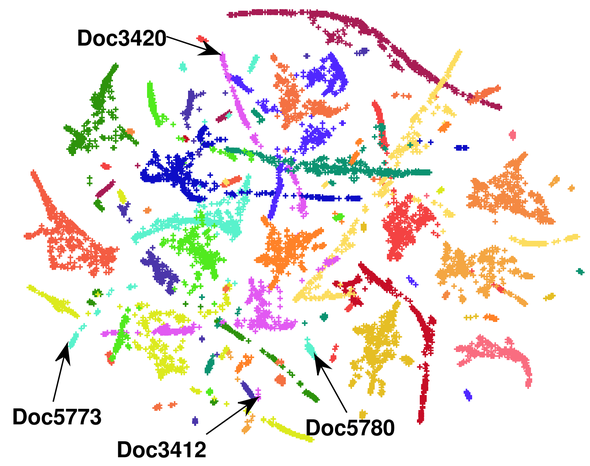

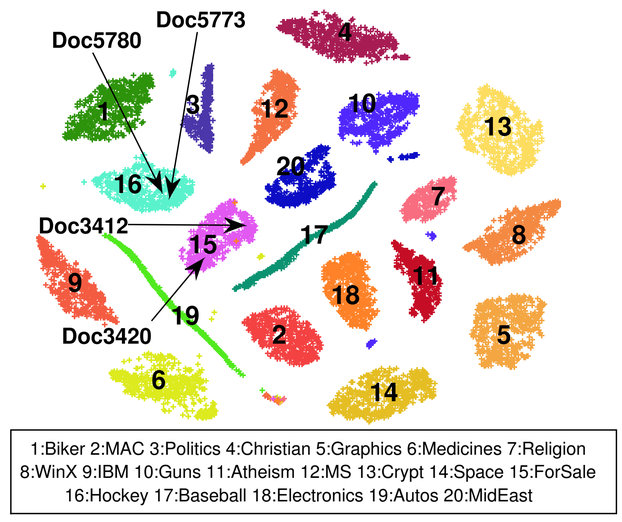

Figure 6: *Visualization of the 32-dimensional document latent semantic vectors by SHTTM and VDSH-S on the 20Newsgroup dataset using t-SNE. Each point represents a document and different colors denote different categories based on the ground truth. In (b)VDSH-S, each number is a category ID and the corresponding categories are shown below the plot.*

DocId	Category	Title/Subject
Doc5780	Hockey	Trade rumor: Montreal/Ottawa/Phillie
Doc5773	Hockey	NHL team leaders in +/-
Doc3420	ForSale	Books For Sale [Ann Arbor, MI]
Doc3412	ForSale	*** NeXTstation 8/105 For Sale ***

Table 4: *The titles of four sample documents in Figure 6*

References

[1] M. Datar, N. Immorlica, P. Indyk, and V. S. Mirrokni. Locality-sensitive hashing scheme based on p-stable distributions. In *Proceedings of the twentieth annual symposium on Computational geometry*, pages 253–262. ACM, 2004.

[2] W. Liu, J. Wang, R. Ji, Y.-G. Jiang, and S.-F. Chang. Supervised hashing with kernels. In *Computer Vision and Pattern Recognition (CVPR), 2012 IEEE Conference on*, pages 2074–2081. IEEE, 2012.

[3] R. Salakhutdinov and G. Hinton. Semantic hashing. *International Journal of Approximate Reasoning*, 50(7):969–978, 2009.

[4] Q. Wang, D. Zhang, and L. Si. Semantic hashing using tags and topic modeling. In *Proceedings of the 36th international ACM SIGIR conference on Research and development in information retrieval*, pages 213–222. ACM, 2013.

[5] Y. Weiss, A. Torralba, and R. Fergus. Spectral hashing. In *Advances in neural information processing systems*, pages 1753–1760, 2009.

[6] D. Zhang, J. Wang, D. Cai, and J. Lu. Self-taught hashing for fast similarity search. In *Proceedings of the 33rd international ACM SIGIR conference on Research and development in information retrieval*, pages 18–25. ACM, 2010.

A Quantitative Survey Of Two Eigenvalue Bounds Of Matrix Polynomials

Tim Shur, Department of Computer Engineering, Santa Clara University
Advisor: Aaron Melman, Department of Applied Mathematics, Santa Clara University

Objective

We examine two improvements on the Cauchy and Pellet radii of matrix polynomials. These improvements may be significant but no comprehensive comparison has been carried out to date to verify their effectiveness. Our goal is to do precisely that for matrix polynomials arising from real-world applications.

Introduction

The polynomial eigenvalue problem is to solve $P(z)v = 0$ for a nonzero eigenvector v and corresponding eigenvalue z, where the matrix polynomial P is given by

$$P(z) = A_n z^n + A_{n-1} z^{n-1} + \cdots + A_0, \qquad (1)$$

with $A_j \in \mathbb{C}^{mxm}$ for $j = 0, 1, ..., n$. We will use this definition for $P(z)$ henceforth.

Matrix polynomials arise in many engineering fields such as structural dynamics, fluid mechanics, and vibration analysis. Their eigenvalues often have physical significance. For example, if a matrix polynomial is constructed to model the vibrations of a bridge affected by wind, the eigenvalues correspond to the natural resonance frequencies and can be used to build efficient solutions to minimize resonance in the bridge [4]. While the degree of these matrix polynomials is typically low (2-4), the coefficients can sometimes be quite large (hundreds to thousands of rows and columns).

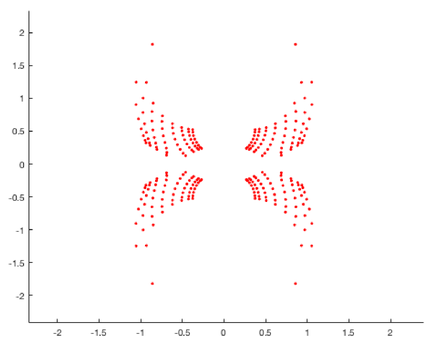

Figure 1: Example of eigenvalues of the 60x60 butterfly problem.

Cauchy Bound Results

Generalized Cauchy Theorem. All eigenvalues of $P(z)$, as defined in (1), lie in $z \leq R$ when A_n is nonsingular, and lie in $z \geq r$ when A_0 is nonsingular, where R and r are the unique positive roots of $||A_n^{-1}||^{-1}x^n - ||A_{n-1}||x^{n-1} - \cdots - ||A_1||x - ||A_0|| = 0$ and $||A_n||x^n + ||A_{n-1}||x^{n-1} + \cdots + ||A_1||x - ||A_0^{-1}||^{-1} = 0$, respectively, for any matrix norm. [1]

Improved Cauchy Theorem. Let $P(z)$ be defined as in (1), with A_n nonsingular. Denote by k the smallest positive integer such that A_{n-k} is not the null matrix, and define $Q^{(L)}(z) = (A_n z^k - A_{n-k})P(z)$ and $Q^{(R)}(z) = P(z)(A_n z^k - Z_{n-k})$. If $A_n A_{n-k} = A_{n-k} A_n$ and $||A_n^{-2}||^{-1} = ||A_n|| \, ||A_n^{-1}||^{-1}$, then the Cauchy radii of $Q^{(L)}$ and $Q^{(R)}$ are not larger than the Cauchy radius of P when the same matrix norm is used for all radii. [2]

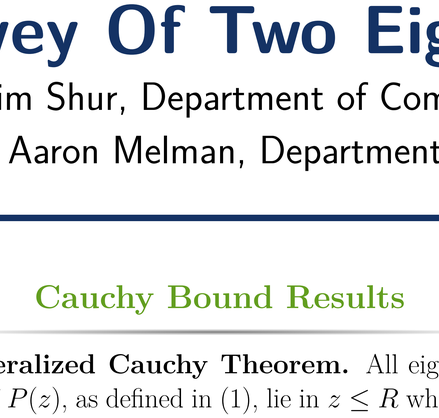

Figure 2: cd_player (above) improved by an order of magnitude.

In Figure 2 and Table 1, we compare the Generalized Cauchy Theorem with its improvement and observe significant improvement in many cases. Below are some of the most significant.

Problem	Cauchy	Improvement	Statistic
cd_player	1.07E+07	1.87E+06	**3.82E+07**
omnicam1	18.80	4.110	**5.469**
power_plant	9.94E+04	6.45E+03	**16.29**
speaker_box	8.01E+07	9.18E+04	**1.05E+03**

Table 1: Data from a few of the tested problems.

Pellet Bound Results

Generalized Pellet Theorem. Let $P(z)$ be defined as in (1) with $A_0 \neq 0$. Let A_ℓ be invertible for some ℓ with $1 \leq \ell \leq n-1$, and let the polynomial $||A_n||x^n + ||A_{n-1}||x^{n-1} + \cdots + ||A_{\ell+1}||x^{\ell+1} - ||A_\ell^{-1}||^{-1}x^\ell + ||A_{\ell-1}||x^{\ell-1} + \cdots + ||A_1||x + ||A_0||$ have two distinct positive roots ρ_1 and ρ_2 with $\rho_1 < \rho_2$ for any matrix norm. Then $\det(P)$ has exactly ℓm zeros in or on the disk $|z| = \rho_1$ and no zeros in the open annular ring $\rho_1 < |z| < \rho_2$. [1]

Improved Pellet Theorem. Let $P(z)$ be defined as in (1) with A_ℓ nonsingular, and with Pellet ℓ-radii ρ_1 and ρ_2, where $1 \leq \ell \leq n-1$ and $0 < \rho_1 < \rho_2$. Denote by k the smallest positive integer such that $A_{\ell-k}$ is not the null matrix, let $A_\ell A_{\ell-k} = A_{\ell-k} A_\ell$, and define $Q^{(L)}(z) = (A_\ell z^k - A_{\ell-k})P(z)$ and $Q^{(R)}(z) = P(z)(A_\ell z^k - Z_{\ell-k})$. If $||A_\ell^{-2}|| = ||A_\ell^{-1}|| \, ||A_\ell||^{-1}$, then $Q^{(L)}$ has Pellet $(\ell + k)$-radii $\sigma_1^{(L)}$ and $\sigma_2^{(L)}$, satisfying $0 < \sigma_1^{(L)} \leq \rho_1 < \rho_2 \leq \sigma_2^{(L)}$, and $\det(P)$ has exactly ℓm zeros in or on the circle $z = \sigma_1^{(L)}$, and no zeros in the open annular ring $\sigma_1^{(L)} < z < \sigma_2^{(L)}$. An analogous result holds for $Q^{(R)}$. [3]

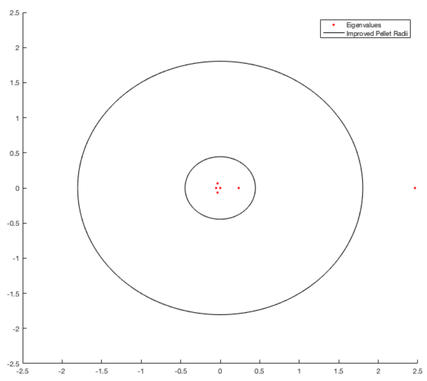

Figure 3: Improved Pellet radii for the bilby problem.

Analysis suggests that the improved Pellet radius is usually only slightly better than the Pellet radius. Nevertheless, the most interesting case is in the bilby problem (pictured in Figure 3). Here, the improved theorem returned a radius while the original theorem did not.

Conclusion

We surveyed improvements of Cauchy and Pellet radii for a large number of engineering problems, some shown here, proving their practical worth. Given their low computational cost, there is no reason not to apply the improvements. To our knowledge, this is the first such survey of real-world applications, previous comparisons having relied on artificial, randomly generated problems.

Further Research

Further research can be done on the iterative quality of these improvements, different multipliers with guaranteed improvement (currently nonexistent), and on left- and right-multiplication of the polynomial multipliers, which may affect sparsity, depending on the structure of the matrix coefficients.

References

[1] Melman, A. *Generalization and variations of Pellet's theorem for matrix polynomials.* Linear Algebra Appl., 439 (2013), 1550–1567.

[2] Melman, A. *Bounds for eigenvalues of matrix polynomials with applications to scalar polynomials.* Linear Algebra Appl., 504 (2016), 190–203.

[3] Melman, A. (in press). *Improvement of Pellet's theorem for scalar and matrix polynomials.* C. R. Math. Acad. Sci. Paris, 354 (2016), 859âĂŞ863.

[4] Tisseur, F. and Meerbergen, K. *The quadratic eigenvalue problem.* SIAM Rev., 43 (2001), 235–286.

Acknowledgements

This research was carried out with a grant from the Kuehler undergraduate research program at Santa Clara University.

Santa Clara University
School of Engineering

Contact Information
Web: http://students.engr.scu.edu/~tshur/
Email: tshur@scu.edu

Neural Semantic Personalized Ranking for Item Cold-Start Recommendation

Travis Ebesu, Yi Fang

Department of Computer Engineering
Santa Clara University

Santa Clara University
School of Engineering

Problem

The item cold-start problem, which is caused by the recommendation system's incapability of dealing with new items due to the lack of ratings feedback.

Key Contributions

- We address the item cold-start recommendation task by inferring semantic representation of items using deep neural network and implicit user feedback.
- We propose a novel probabilistic generative modeling approach to characterize how a preference of items is observed based on implicit feedback.
- We derive two variants based on various pairwise probability functions including the Logistic and Probit functions.
- Extensive experiments on two public real-world datasets demonstrate that NSPR can significantly advance the state of the art.

Neural Semantic Personalized Ranking

We take a pairwise approach to item recommendation by assuming that a user prefers the items that she has interacted with rather than those items that she has not interacted with.

Given user $i \in U$, we use j^+ to denote a positive item (i.e., interacted/observed item) and j^- for a negative item (i.e., uninteracted/unobserved item). We form preference triplets (i, j^+, j^-). We define the neural network as $\mathbf{d}_j$ as the input term vector, $\mathbf{y}_j$ as the output vector, l as the l^{th} hidden layer ($l \in [1, L-1]$). $\mathbf{a_l}$, $\mathbf{W_l}$ and $\mathbf{b_l}$ are the activation output, weight matrix and bias vector respectively.

$$\mathbf{a}_{1,j} = \mathbf{W}_1\mathbf{d}_j \qquad \mathbf{a}_{l,j} = \psi(\mathbf{W}_l\mathbf{a}_{l-1,j} + \mathbf{b}_l)$$

$$\mathbf{y}_j = \mathbf{W}_L\mathbf{a}_{L-1,j} + \mathbf{b}_L \qquad \psi(x) = \frac{1 - e^{-2x}}{1 + e^{-2x}}$$

The probability that user i prefers item j^+ over j^- is given as:

$$\mathcal{S}(r(i, j^+) - r(i, j^-)) = \mathbf{u}_i^T(\mathbf{v}_{j+} - \mathbf{v}_{j-})$$

The posterior log likelihood of observing all the preference triplets is:

$$\mathcal{L} = \sum_i \sum_{j^+, j^-} \log \mathcal{S}\Big(r(i, j^+) - r(i, j^-)\Big) - \frac{1}{2\sigma_v^2} \sum_{j^+, j^-} ||\mathbf{v}_j - \mathbf{y}_j||_2^2 - \frac{1}{2\sigma_u^2} \sum_i ||\mathbf{u}_i||_2^2$$

For the cold-start problem for the unobserved item j we score

$$r(i, j) \approx (\mathbf{u}_i^*)^T(\mathbf{W}_L\mathbf{a}_{L-1,j} + \mathbf{b}_L)$$

Parameters are estimated with Stochastic Gradient Descent (SGD) to obtain the Maximum A Posteriori (MAP).

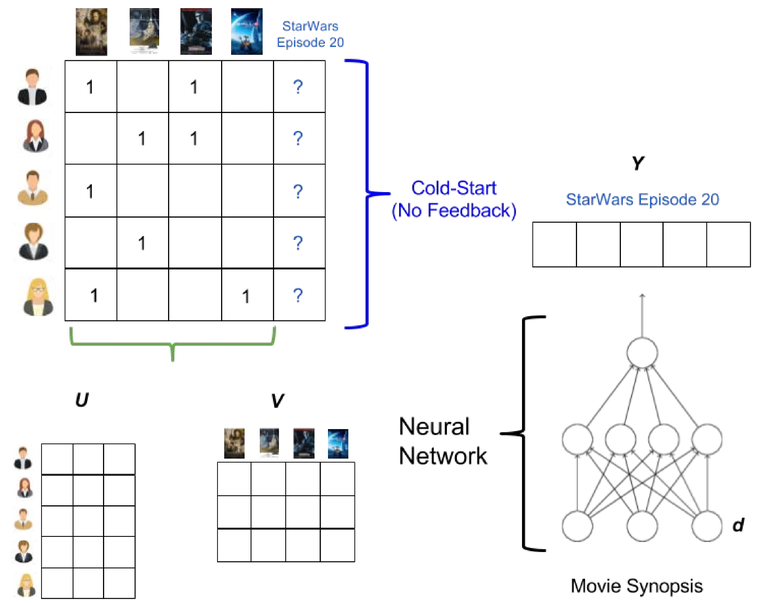

Pairwise Probability

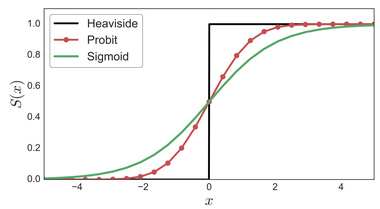

Sigmoid:

$$\mathcal{S}(x) = \frac{1}{1 + \exp(-x)}$$

Probit:

$$\mathcal{S}(x) = \Phi(x) = \int_{-\infty}^{x} \frac{1}{\sigma\sqrt{2\pi}} \exp\left(-\frac{(x-\mu)^2}{2\sigma^2}\right) dx$$

Datasets

	citeulike-a	*Yahoo! Movies*
Users	5,551	7,642
Items	16,980	11,915
Ratings	204,987	221,36

Results

citeulike-a Recall@300 (left) and NDCG@10 (right) for varying number of latent factors (K) and hidden layers (L) averaged over 5-folds.

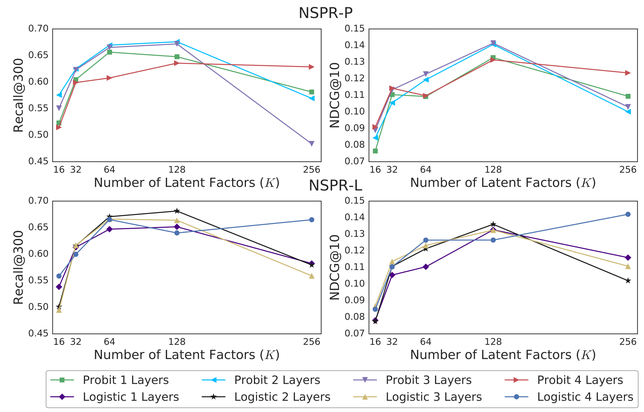

Yahoo! Movies Recall@300 (left) and NDCG@10 (right) for varying number of latent factors (K) and hidden layers (L) for the *Yahoo! Movies* dataset.

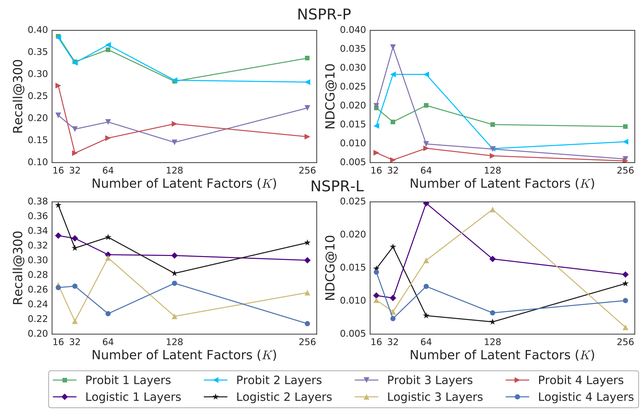

Future Directions

- Incorporate other types of deep learning architectures e.g. Convolutional neural networks (CNN), Recurrent neural networks (RNN).
- Deeper architectures by applying data normalization techniques.
- Investigate other Learning-to-Rank paradigms such as listwise and pointwise.

Energy-Efficient Channel Assignment and Association Management in Centralized WLANs

February 2017

Vahid Esmaeelzadeh and Behnam Dezfouli

SCU's Internet of Things Technologies Research Lab (SIOTECH), Department of Computer Engineering

Email: vesmaeelzadeh@scu.edu, bdezfouli@scu.edu

Introduction

Continuous growth in the number of WiFi-enabled devices and the traffic conveyed through wireless local area networks (WLANs) necessitate the use of centralized architectures to ease the management of WLANs (based on the global network view) and decrease the deployment cost of new applications and protocols.

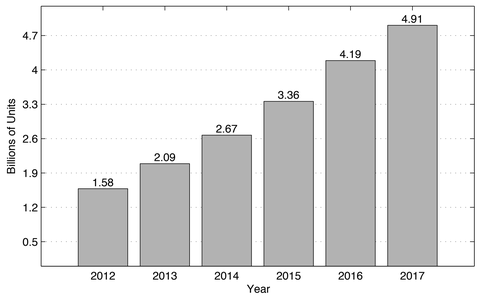

Increasing Growth in the number of WiFi-enabled Devices

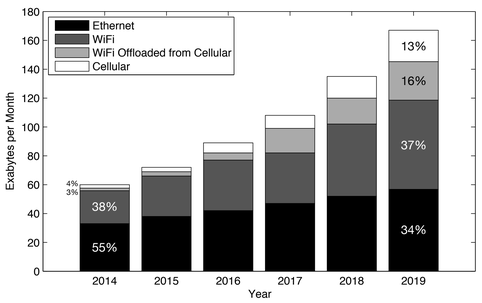

Traffic Trend of WLANs

Almost all organizations use WLANs as an essential component to be connected to an always-on network so that WiFi has become the favorite type of network connection. Hence, the size of WLANs is getting larger in terms of the number of clients, APs and WiFi traffic. Consequently, the design and implementation of high performance enterprise WLANs are so crucial that bolds the essence of centralized architectures for WLANs.

Two main challenges in enterprise WLANs are:

- Interference mitigation
- Association management

The main approaches to handle the interference and association are:

- Dynamic Channel Assignment (DCA)
- Dynamic Association Management (DAM)
- Transmit Power Control (TPC)

Centralized WLAN Architectures

Industry and academia have focused on the centralized solutions for WLANs because of the following main benefits:

- Facilitating and reducing WLAN operating costs
- Enabling the granular control of data plane
- Providing easier and integrated security and mobility handling in WLANs
- Ease of implementing new mechanisms and schemes

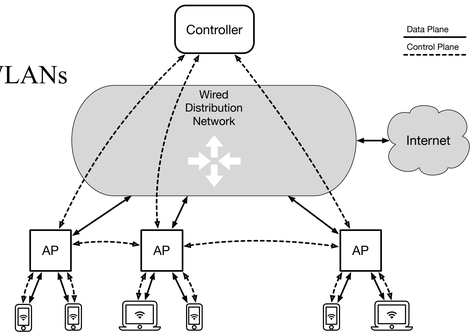

A Typical Central WLAN

An effective central architecture provides some protocols, primitives and tools to

- Collect information across all components of a WLAN through the control plane,
- Evaluate and analyze the collected data to generate useful statistics in the controller,
- Run WLAN management protocols and schemes that rely on QoS requirements and the collected information to make management and control decisions, and
- Apply the decisions on different components of WLAN through the control plane in an efficient way.

The evolution of centralized WLAN architectures is as follows:

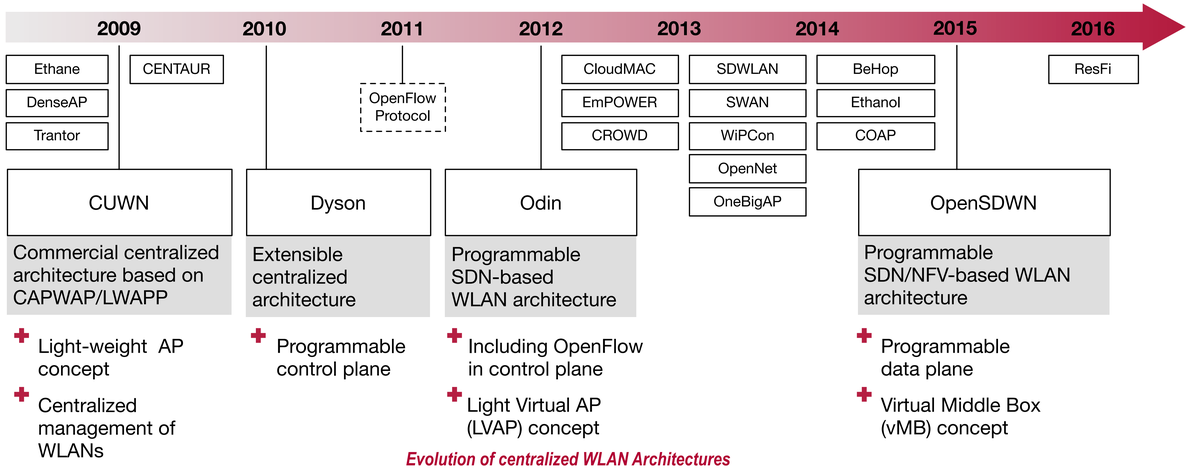

Evolution of centralized WLAN Architectures

Main Challenges in DCA, DAM and TPC Schemes

Interference and **client-AP association metrics** are the basics of DCA, DAM and TPC algorithms. In order to enable QoS-aware WLAN management, it is required to consider the traffic demand-based interference as well as proportional time and bandwidth fairness. Different types of metrics which can be used are:

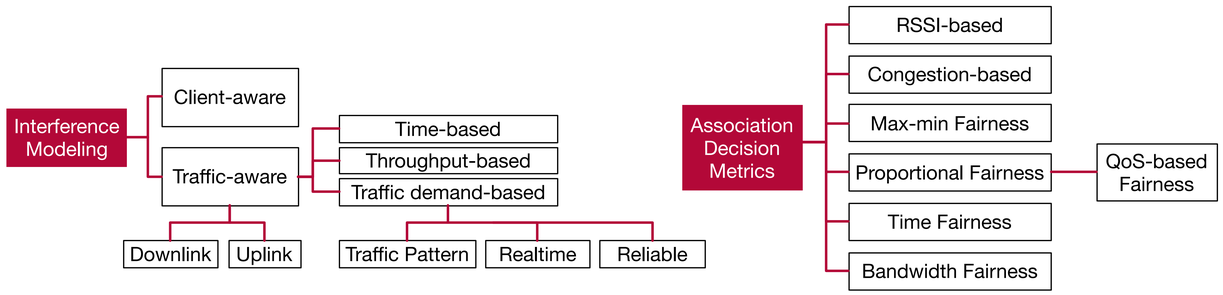

Optimization Problem

Sets of **APs**, **Clients** and available **Channels**

Realtime Traffic Demand of Clients	**Reliable** Traffic Demand of Clients
Downlink Traffic Demand of Clients	**Uplink** Traffic Demand of Clients

Multi-Objective Optimization Problem

- Minimization of **Total Power Consumption** of APs
- Maximization of **Proportional Bandwidth Fairness** among Clients (based on *realtime traffic demands*)
- Maximization of **Proportional Reliability Fairness** among Clients (based on *reliable traffic demands*)

Association Matrix | Channel Assignment Matrix | Transmit Power vector

The approach aims to support realtime and reliable applications considering both traffic directions, i.e., downlink and uplink. Simultaneous tuning of the transmit power of APs, assignment of operating channels of APs, and AP-client associations are performed with the goal of minimizing total power consumption and maximizing proportional bandwidth and reliability fairness among clients.

Conclusions & Future Work

A centrally-controlled and QoS-aware WLAN network is introduced through a multi-objective optimization problem considering QoS demands of clients focusing on two types of applications:

- Internet-of-Things (IoT)
- High throughput communications such as video streaming

The nature of traffic in IoT is usually reliable and the dominant traffic is in the uplink direction. However, in video streaming, the dominant traffic is in the downlink direction and in a realtime manner. A new architecture for the deployment of proposed approach is considered as one of the future works.

Recommendation System Based on Dynamic Matrix Factorization

Advisor : Yuhong Liu

Author : Yaojian Wang / Department : School of Engineering

Santa Clara University
School of Engineering

What is Collaborative Filtering?

In everyday life, people rely on recommendations from other people by spoken words, reference letters, news reports from news media, general surveys, and so forth.

In the narrower sense, collaborative filtering is a method of making automatic predictions (filtering) about the interests of a user by collecting preferences or taste information from many users (collaborating).

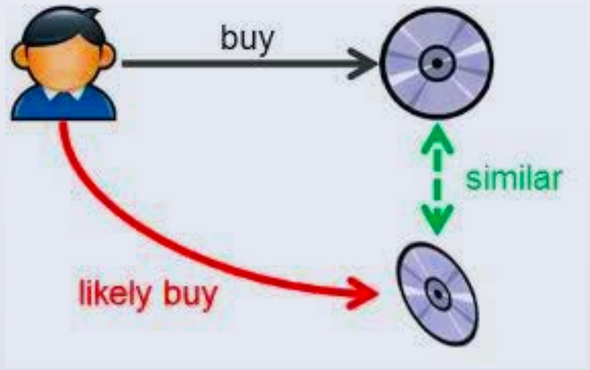

What is Matrix Factorization?

Non-negative matrix factorization (NMF or NNMF), is a group of algorithms in multivariate analysis and linear algebra where a matrix R is factorized into (usually) two matrices P and Q, with the property that all three matrices have no negative elements. This non-negativity makes the resulting matrices easier to inspect.

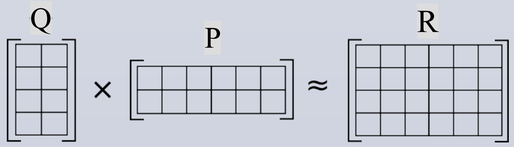

Firstly, we create matrix p and q by using random number

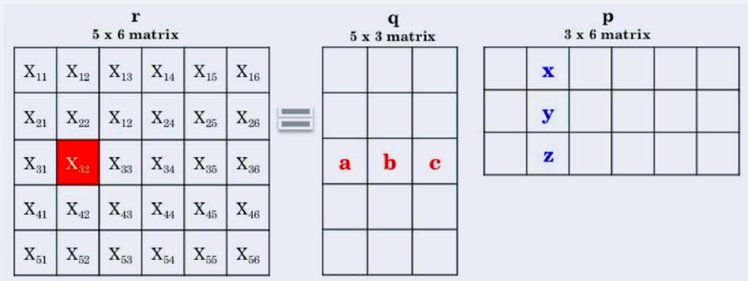

$$X_{32} = (a, b, c) \cdot (x, y, z) = a * x + b * y + c * z$$

Rating Prediction: $\hat{r}_{ui} = q_i^T p_u$ (User Preference Factor Vector; Movie Preference Factor Vector)

Then, we minimize the cost function

$$\min_{q^*,p^*} \sum_{(u,i)\in k} (r_{ui} - x_{ui})^2$$

To learn the factor vectors (p_u and q_i)

Minimizing Cost Function (Least Squares Problem)

What is Dynamic Matrix Factorization?

Matrix factorization that consider temporal dynamics. Linear Dynamic System (LDS) offer an elegant way of expressing the relationship between latent factors at different time steps. For each user n, LDS derives for each time step t a dynamics matrix A that represents the mapping of latent factors from time step t-1 to t. When LDS is applied to a set of users, we obtain DMF.

$$y_{n,t} = C_n \cdot x_{n,t} + v \qquad x_{n,t} = A_{n,t} \cdot x_{n,t-1} + w$$
$$v \sim \mathcal{N}(0, R) \qquad w \sim \mathcal{N}(0, Q)$$

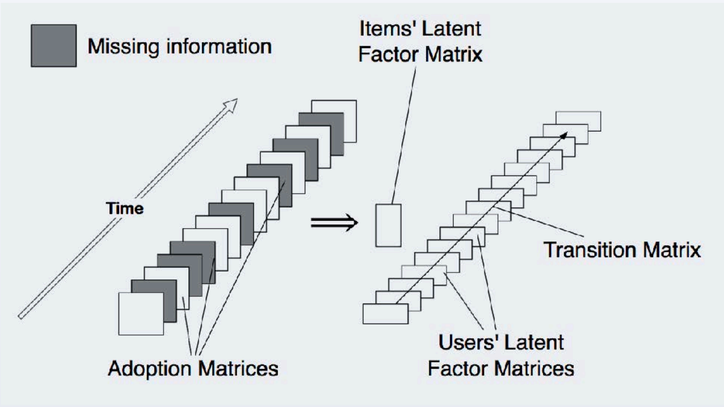

What do we want to do?

What we want to do is to find a better way to improve Dynamic Matrix Factorization. Currently, some researchers have developed DMF based on Kalman Filter and Rauch Tung Striebel (RTS) smoothing algorithm.

Problems we need to solve

1. Compare Dynamic Matrix Factorization with Tensor Factorization.
2. What is the limitation of NMF when considering temporal dynamics?
3. Find a better model to obtain Dynamic Matrix Factorization.

Process Design for CNT Growth on Graphene

Zachary Baron, Richard Senegor, Changjian Zhou, and Cary Y. Yang
Center for Nanostructures, Santa Clara University

Abstract

Carbon nanotubes (CNTs) and graphene are promising candidates to replace copper and tungsten as on-chip interconnect materials due to their 2-3 orders of magnitude larger current-carrying capacities, superior thermal and electronic transport properties, and demonstrated ability to form vertically aligned CNTs as grown on graphene. An all-carbon 3D structure consisting of CNTs on graphene is studied as a potential building block for future-generation on-chip interconnects.

Background and Motivation

- The primary challenge of copper interconnects with nanoscale linewidths lies in on-chip operating current density approaching or exceeding its current-carrying capacity of ~10^6 A/cm^2 due to electromigration [1].
- CNT vias grown on metal underlayer give rise to significant contact resistance, which could be mitigated by an all-carbon 3D structure [2].

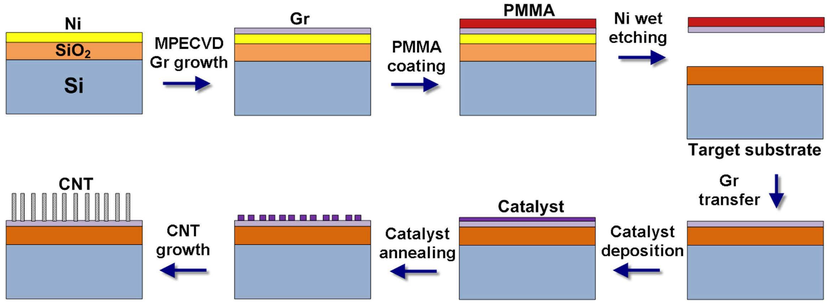

Figure 1: Process flow for CNT-Graphene test structure fabrication.

CNT-graphene fabrication process [3]

- Graphene grown using MPECVD (microwave plasma-enhanced chemical vapor deposition) on thick Ni catalyst film deposited on oxide substrate.
- Graphene transferred onto non-conductive substrate.
- CNT grown on transferred graphene using PECVD.

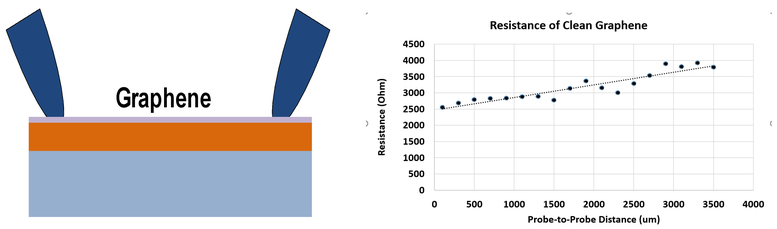

Figure 2: Electrical test of as-grown graphene layer on Ni film.

[1] "International Technology Roadmap for Semiconductors (ITRS) 2013." Available online at http://www.itrs2.net.
[2] P. Wilhite, A.A. Vyas, J. Tan, J. Tan, T. Yamada, P. Wang, J. Park, and C.Y. Yang, "Metal-nanocarbon contacts," *Semiconductor Science & Technology* **29** (2014) 054006 (16pp).
[3] C. Zhou, A. R. Senegor, Z. Baron, Y. Chen, S. Raju, A. Vyas, M. Chan, Y. Chai, and C.Y. Yang, "Synthesis and interface characterization of CNTs on graphene," *Nanotechnology* **28** (2017) 054007 (10pp).

Scanning Electron Microscopy (SEM) Images

CNTs as-grown on graphene with Fe or Ni catalyst are vertically aligned.

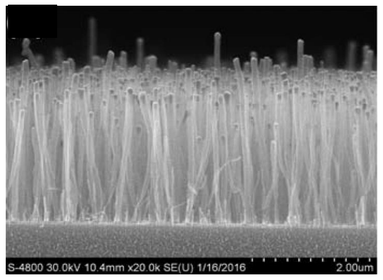

Figure 3: Cross-sectional image of CNTs grown on graphene using Ni catalyst.

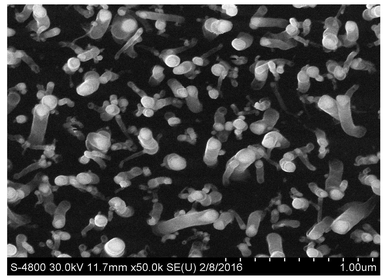

Figure 4: Top-view image of CNTs grown on graphene using Ni catalyst.

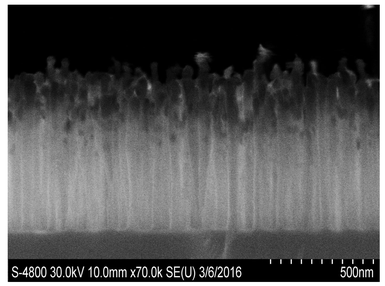

Figure 5: Cross-sectional image of CNTs grown on graphene using Fe catalyst.

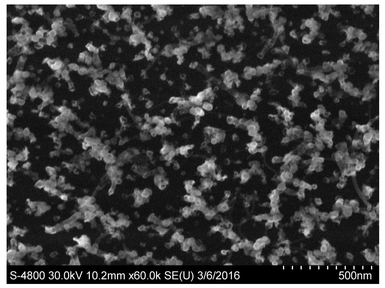

Figure 6: Top-view image of CNTs grown on graphene using Fe catalyst.

Transmission Electron Microscopy (TEM) Cross-sectional Images [3]

- CNT-graphene interface for Ni-catalyzed CNT growth reveals structural damage to graphene, most likely by Ni.
- For Fe-catalyzed CNT growth, interface image suggests C-C bonding between CNTs and graphene.

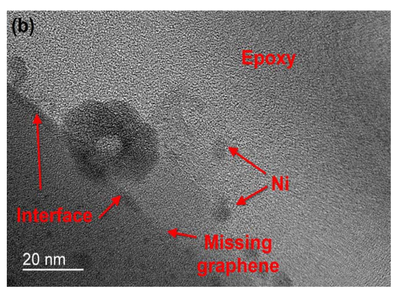

Figure 7: Cross-sectional image of CNT/graphene interface for CNT grown with Fe catalyst.

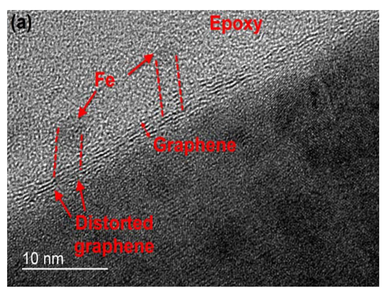

Figure 8: Cross-sectional image of CNT/graphene interface for CNTs grown with Ni catalyst.

Electrical Characteristics of CNT/Graphene Structure [3]

Electrical characteristics of CNT/graphene heterostructure from two-point current-voltage (I-V) measurements are shown below. The results provide evidence that the CNT/graphene structure exhibits electrical conduction paths through graphene that are not disrupted by the CNT growth process.

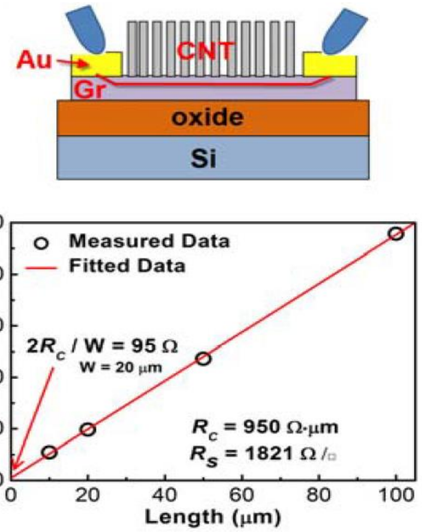

Figure 9: Electrical measurement schematic and resistance versus graphene length behavior after CNT growth, where W denotes the width of graphene strip, R_c the sheet resistance, and R_S the contact resistivity.

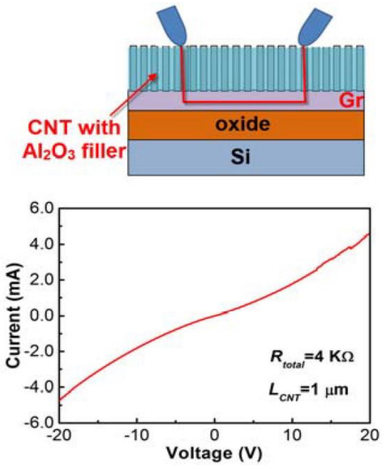

Figure 10: Electrical measurement schematic and I-V characteristics of CNT-graphene heterostructure after oxide filling and polishing to expose CNT tips, where R_{total} denotes the total extracted resistance and L_{CNT} the CNT height.

Conclusion

- An all-carbon 3D interconnect structure consisting of vertically aligned CNTs grown on graphene has demonstrated conduction and possible C-C bonding across the CNT/graphene interface.
- The choice of catalyst for CNT growth on graphene is critical for achieving a viable 3D interconnect structure.